

Part I

Nonlinear Waves in Lattices





Chapter 1

Localized Nonlinear Waves in Lattices

Abstract

In this chapter we will study the nonlinear behavior of atomic lattices coupled by realistic potentials. Essentially, in this conservative system the dispersion is caused by lattice periodicity, where the nonlinearity appears at the coupling between oscillators following a Coulomb type interaction. Thus, strongly supersonic localized waves can be generated and propagates along the lattice in the form of kinks. With the aim of study a more realistic physical system, we include a model accounting for nuclear repulsion effects that modifies the nonlinear interaction for short interatomic distances. In addition, we propose a substrate potential that modifies the lattice dispersion relation. The physical parameters are those of the K^+ ion lattice in a mica muscovite layered silicate.

1.1 Motivation: dynamics of potassium ions in layered silicates

Many minerals are known by their capability of recording the tracks of charged particles, and are often used as solid state nuclear track detectors (SSNTDs); a review of the subject can be found in Refs. (Durrani, 2001; Durrani, 2008).

Among them, mica muscovite has been relevant as it was the second material and the first natural one where tracks from fission fragments were found (Silk et al., 1959). Very soon later fossil tracks were also found in mica (Price et al., 1962). It seems to be one of the most sensitive of natural SSNTD (Fleischer, 2011). Due to its resistance to heat, it can be used inside a nuclear reactor core for particle detection. It has also been used in geochronology and to probe the existence of dark matter (Snowden-Ifft et al., 1995), to find exotic nuclear reactions, decays of superheavy elements and weakly interacting massive particles (WIMPs) (Durrani, 2001; Durrani, 2008). Micas have also important technological applications due their dielectric and heat shielding properties. Other uses are as matrixes for films, monochromators and dispersive crystals.

Silicates are also among the materials considered as engineered barriers for nuclear waste storage due to its high rate of reaction with heavy ions in low temperature reconstructive transformations (Alba et al., 2001). This property can be of importance for the development of advanced structural ceramics (Hong et al., 2002) and has been related to the existence of nonlinear localized vibrations related with the ones described in this work (Archilla et al., 2006; Dubinko et al., 2011).

Tracks of positrons, muons and other particles have been reported (Russell, 1967b; Russell, 1967a; Russell, 1988b; Russell, 1988a) in mica muscovite. Some of these tracks were identified as produced by positrons resulting from the $\beta+$ decay of ^{40}K. This isotope is relatively abundant in the minerals and can also experience $\beta-$, electron capture and other kind of decays. Most of the tracks, however, cannot be explained as being produced by charged particles but could have been produced by some kind of vibrational excitation because, among other properties, the tracks are along the close-packed lines of the K^+ hexagonal layer shown in Fig. 1.1. One interpretation of these tracks is that they are formed by the localized nonlinear excitations, sometimes called quodons (Schlößer et al., 1994), whose exact nature is still not known.

A likely source for the vibrational energy required to initiate a *quodon* is the recoil energy of the ^{40}K after β decay, which can be up to 52 eV. In muscovite, there are about 3 decays per second and cm^3, so after many years of the sensitive period, when tracks recording is possible, there are many possibilities to initiate a *quodon*. An experiment was done to shed some light into the relationship between tracks and *quodons* (Russell et al., 2007). A mica specimen was irradiated with alpha

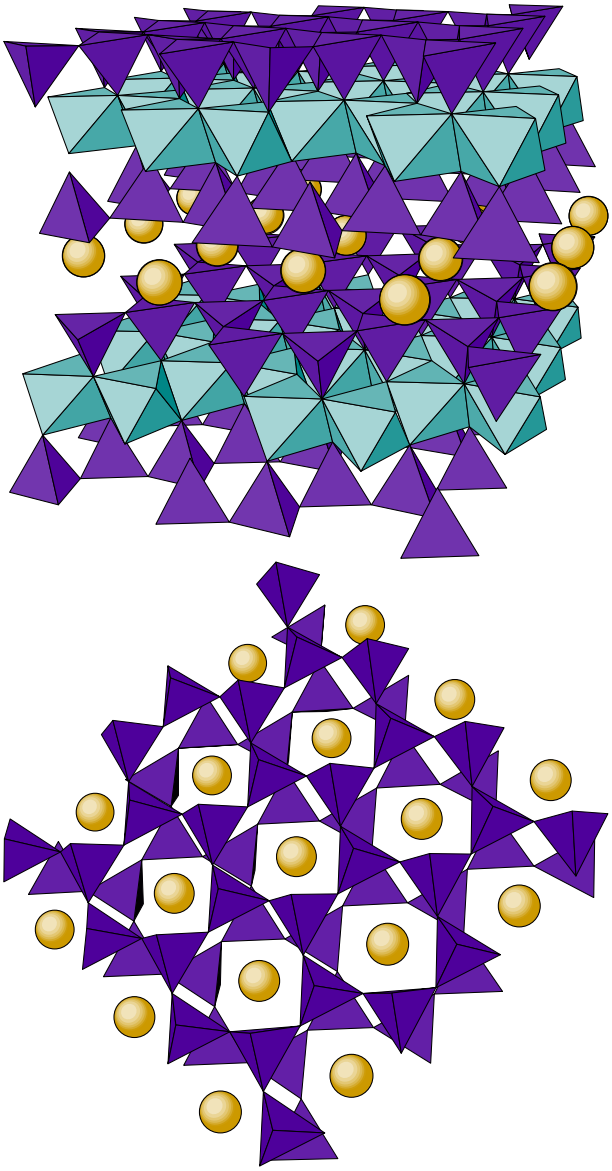


Figure 1.1: Representation of the mica structure from the point of view that emphasizes the close-packed lines of the K^+ hexagonal layer represented by yellow balls. Crystal structure of muscovite. The circles represent the potassium ions forming the interlayer sheet. The unit cell includes two silicate layers and two K^+ions with parameters $a = 5.19$Å, $b = 9.02$Å; $c = 20.0$ Å; and $\beta = 95.7^o$. For a view from the top, see the later Fig. 1.16

particles and the ejection of atoms was detected on the other side, along closed packed lines. The ejected atoms could not been identified and also sputtering energies are not known exactly, however from experimental and theoretical studies, they are known to be in the range of 4-8 eV (Kudriavtsev et al., 2005).

In an attempt to understand this phenomenon, numerical simulations were conducted in an idealized 1D model where the particles of increasing energy hit the boundary of the lattice (Dou et al., 2011). This study reports the formation of a breather and kinks and the ejection of atoms at the opposite boundary of the sample. However, the model did not intend to use realistic values of the mica muscovite parameters.

A minimal model of the cation lattice with realistic parameters was proposed recently (Archilla et al., 2013; Archilla et al., 2014). Only K^+ ions were considered with the actual potassium mass and Coulomb interaction between them. The interaction with the rest of the lattice was implicitly considered as the force keeping the ions inside the crystal with the known interatomic distance in muscovite. In those publications, it was reported the existence of supersonic kinks, which were easily generated within a wide range of energies and velocities.

However such model is too simplistic because for relatively high ion energies it results in unrealistically small distances between the ions, of tenths of angstrom.

In this chapter, we develop a dynamical model in which we use the Ziegler-Biersack-Littmark (ZBL) short-range repulsive potential, introduced in particle bombardment studies (Biersack et al., 2008). ZBL potential describes the Coulomb repulsion between nuclei, which is partially screened by the atom electrons and rapidly decays in few Å. The results for the moving energy-carrying objects in such potential are similar to those obtained with only pure Coulomb interaction (Archilla et al., 2013; Archilla et al., 2014), namely the supersonic kinks, traveling without attenuation for long distances, can be produced with arbitrary energies. But the inter-particle distances in the kinks are limited by physically reasonable values in our dynamical model. Note that our dynamical model allows for bond dissociation, which is a necessary condition for the realistic modeling of the normal energy transport in low-dimensional systems (Savin et al., 2014).

As a next step towards a more realistic description, we construct explicitly the interaction with the surrounding atoms, using standard empiric potentials introduced in molecular dynamics, which give rise to a periodic non-sinusoidal substrate potential. Supersonic lattice kinks, also called *crowdions* (Kosevich et al., 1973), are also easily obtained. They propagate in such potential with a velocity which is independent of the input and is determined only by the lattice potential parameters. For the smaller energies, the kink dissipates in phonons, while for larger energies the excess energy is radiated until reaching the value of crowdion energy.

The final crowdion energy is approximately 26 eV, which can be provided by

the recoil of isotopes of potassium after radioactive decay and is larger than the sputtering energy. This ratio of characteristic energies allows to assume that the tracks found in mica muscovite can be related with the lattice kinks or crowdions.

The literature about kink propagation in lattices with different inter-particle and on-site potentials is extensive. The most studied and generic model is the Frenkel-Kontorova (FK) model(Frenkel et al., 1938), see reviews in Refs. (Chaikin et al., 1995; Braun et al., 1998; Braun et al., 2004). However, most of the kinks considered in this model are subsonic ones. Supersonic kinks in the systems with substrate have been found in models with anharmonic intersite coupling (Kosevich et al., 1973; Milchev, 1990; Savin, 1995; Zolotaryuk et al., 1997). They have the property than only a discrete set of velocities allows the propagation of kinks without attenuation. They can be described as multi-kinks or lattice N-solitons depending on whether the description is done in terms of coordinates, strains or velocities. The kink with the unique supersonic velocity, propagating in our dynamical model of the cation layer on a substrate, is a double-kink.

The FK model has also been considered in layered materials, to model, for example, the in-plane dynamics of a few-layer graphene, in order to explain molecular dynamics simulation results for the cross-plane thermal conductance (Ni et al., 2014). One particular characteristic, found in the kinks studied in the present work, is extreme discreteness of the kinks, namely only two particles, and for higher energies, practically only one particle is in motion at a given time. This discreteness allows the complete understanding in physical terms of the mechanism that brings about a single velocity of the kink and why the kink is a double-kink.

The Chapter is organized as follows. First we review and extend the results obtained with only the Coulomb interaction, using the sinusoidal waveform proposed for supersonic kinks in the Fermi-Pasta-Ulam (FPU) lattice (Kosevich, 1993; Kosevich et al., 2004). The sinusoidal waveform is a good description for $\lambda \simeq 3a$, where λ is a characteristic wavelength of the sinusoidal waveform and a is a lattice constant, but fails for $\lambda \simeq 2a$, been replaced by an almost triangular waveform, corresponding to nearly hard-sphere collisions. Afterward we consider the effects of long-range interactions, with several neighbours, and introduce a short-range nearest-neighbor ZBL potential. Thereafter, the substrate potential is constructed and the properties of the single-velocity lattice kinks in the cation layer on the substrate are analyzed with details.

1.2 Minimal model with realistic potentials

1.2.1 Model

We consider as a starting point a one-dimensional (1D) model for the dynamics of K^+ions. Thus, considering nearest-neighbour Coulomb interaction the position,

x_n, of each n-th atom is given by

$$m\frac{\partial^2 x_n}{\partial t^2} = -\frac{\mathrm{K_C e^2}}{(x_{n+1}-x_n)^2} + \frac{\mathrm{K_C e^2}}{(x_n - x_{n-1})^2}, \tag{1.1}$$

where m is the K^+mass, $\mathrm{K_C e^2}$ is the inter-ion Coulomb electrostatic constant. With the aim of explore solutions from a more general approach, we can write the equation in dimensionless form by choosing as unit of distance, $a = 5.19$ Å(i.e. the lattice constant or the equilibrium distance between K^+ ions; for masses, the mass of a K^+ ion, $m_{K^+} = 39.1$ amu; for time, $\tau = \sqrt{m_K a^3/\mathrm{k_e\, e^2}} \simeq 0.2$ ps, where $\mathrm{k_e}$ is the Coulomb constant and e is the elementary unit of charge. Other physical units in the system are velocity $u_V = 2600$ m/s, energy $u_E = 2.77$ eV and frequency 5 THz. Dimensionless speed of sound in this system is $c_0 = \sqrt{2}$, or about 3.700 km/s in physical units.

Thus, defining u_n as the displacement with respect to the equilibrium position normalized to the lattice constant, witch can be expressed as $x_n = a(n + u_n)$, the dimensionless motion equations become

$$\frac{\partial^2 u_n}{\partial t^2} = -\frac{1}{(1+u_{n+1}-u_n)^2} + \frac{1}{(1+u_n-u_{n-1})^2}, \tag{1.2}$$

which describes the chain of ions coupled to their nearest neighbours by electrostatic Coulomb potential. Note hereinafter t will be dimensionless time.

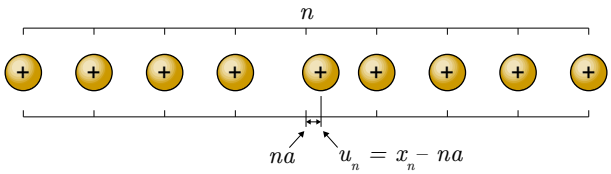


Figure 1.2: Scheme of the one dimensional model of the K^+ ion layer

1.2.2 FPU equivalent lattice

For small amplitudes, the potentials in Eq. (1.2) can be expanded in a series, using that $1/(1+y)^2 \simeq 1 - 2y + 3y^2 - 4\,y^3 \ldots$. Retaining cubic and smaller terms, we obtain

$$\begin{aligned}\frac{\partial^2 u_n}{\partial t^2} \;=\; & c_0^2\,[(u_{n+1}+u_{n-1}-2u_n) \\ & -3/2\,(u_{n+1}-u_n)^2 + 3/2\,(u_n-u_{n-1})^2 \\ & +2\,(u_{n+1}-u_n)^3 - 2\,(u_n-u_{n-1})^3 + \ldots],\end{aligned} \tag{1.3}$$

which are the α-β FPU equations of motion. We would like to emphasize that the α-β FPU Eq. (1.3) describes the Coulomb lattice (1.2) only in the small- and intermediate-amplitude limit and is not applicable to this lattice in the large-amplitude limit, see Fig. 1.9 and the subsection devoted to the triangular waveform below.

1.2.3 Dispersion relations

Linearization Eq. (1.2), i.e. setting $\alpha = \beta = 0$ in Eq. (1.3), the equation of motion is reduced to the well-known discrete linear wave equation

$$\frac{\partial^2 u_n}{\partial t^2} = c_0^2 \ (u_{n+1} + u_{n-1} - 2u_n)\,, \tag{1.4}$$

where c_0, the speed of sound, is the long wavelength phonon velocity. Note that in our scaling $c_0 = \sqrt{2}$. A phonon corresponds to small amplitude particle displacements of the form $u_n = \exp\left(i\left(qn - \omega t\right)\right)$, with q and ω being the phonon wave number and frequency respectively. The dispersion relation and velocities are well known, we include them here for comparison with. Thus, the the phonon dispersion equation in normalized units reads

$$\omega^2 = 4c_0^2 \sin^2 \frac{q}{2} \quad \text{with} \quad q = \frac{2\pi m}{N} \quad \text{and} \quad m = 1, 2, \ldots, N. \tag{1.5}$$

Then, phase and group velocity are expressed for the lattice as

$$\begin{aligned} c_p &= \frac{\omega}{q} = 2c_0 \left| \frac{\sin \frac{q}{2}}{q} \right|, \\ c_g &= \frac{\partial \omega}{\partial q} = c_0 \left| \cos \frac{q}{2} \right|. \end{aligned} \tag{1.6}$$

Thus, those well known relations dispersion of the linear lattice and its group and phase velocity velocity are plotted for the positive first Brillouin zone in Fig. 1.3. The maximum frequency corresponding to the mode with the wave number $q = \pi$ is $\omega_M = 2c_0$. In the limit of long wavelengths, both velocities are equal to the speed of sound c_0, which is also the maximum value. Note that the group velocity becomes zero at the top of the phonon band $q = \pi$.

The maximum frequency in physical units is about 2.2 THz which is larger than the one obtained with molecular dynamics and neutron spectroscopy of about 1.6 THz (Collins et al., 1993; Wada et al., 1991; Chaplot et al., 2002). This is understandable given the simplicity of our model taking into account just one type of atom compared with the complexity of real mica, but it is within the same range of values. Note that the predicted speed of sound in physical units, $c_0 = 3690.2$ m/s, is similar to that found in Ref. (Brudeylins et al., 1995) of 3400-3700 m/s.

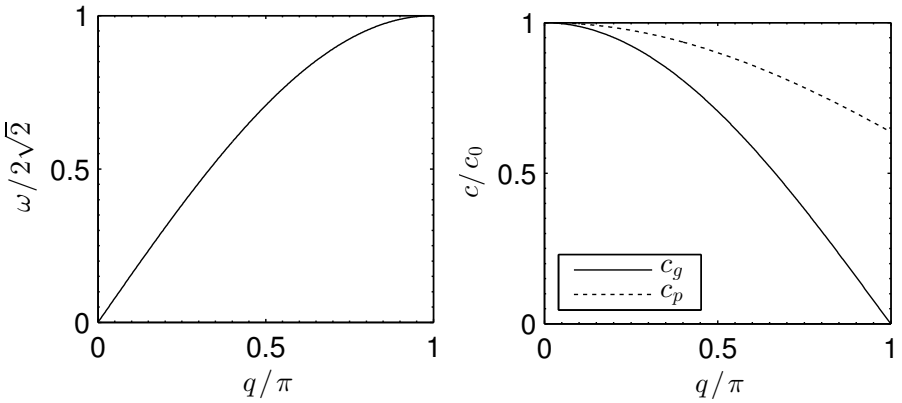


Figure 1.3: Left: Dispersion relation for the linearized Coulomb lattice. Right: Phase speed and group velocity for linearized Coulomb lattice. In the limit of long wavelengths, both give the sound velocity, which can be compared with the values of 3.4–3.7 km/s obtained in Ref. (Brudeylins et al., 1995)

Also note that, in contrast with the *repulsive* character of the full Coulomb interaction, this linearized equation is *attractive*, i.e. if the distance $u_{n+1} - u_n$ increases, the force on the particle u_n is positive. The reason for it is the decreasing nature of the Coulomb force: when the distance with the particle in front increases the repulsion weakens and the repulsion from the particle behind becomes larger pushing the particle n forward.

1.3 Tail analysis

Different types of nonlinear localized solutions are supported by the Coulomb lattice. Although these solutions are large enough to be intrinsically nonlinear, they also have tails of small amplitude which abide the linear equation. Tails cannot exist by themselves but depends on the existence of the nonlinear solution, however its study gives information about the parent excitation. We obtain first the tail properties and later we consider the fully nonlinear solutions. Tails are obtained with the linear system, therefore their properties are common to any system with the same linearization. However, they only give the conditions that the tails have to fulfill. The properties of existence of the nonlinear excitation, its velocity, amplitude and other characteristics have to be worked out with the whole nonlinear system.

Consider a nonlinear localized moving excitation, travelling with velocity V. We also assume that its amplitude decays exponentially far away enough from the

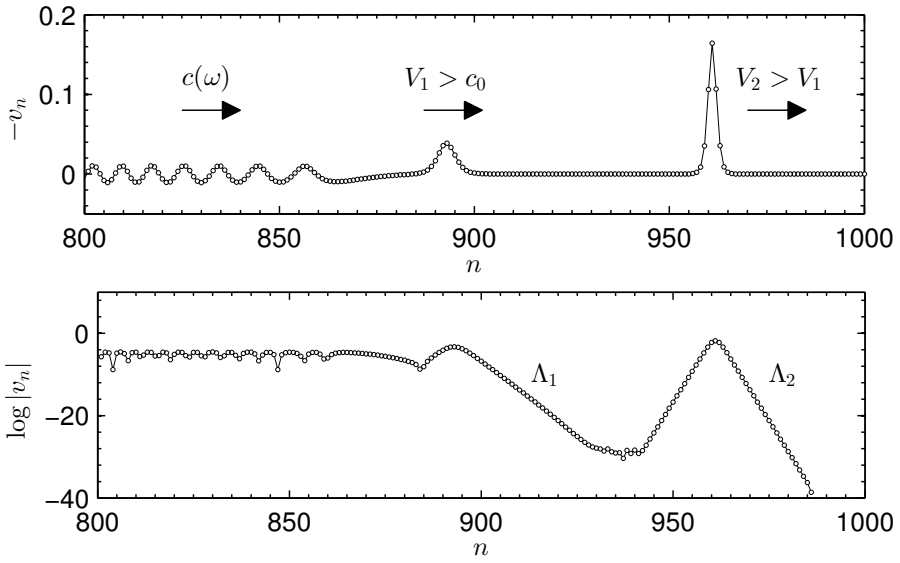


Figure 1.4: Numerical example of two nonlinear localized waves travelling at different velocities and leaving a phonon tail. (Top) profiles obtained at fixed time. (Bottom) logarithmic representation showing that front and back tails exist with different decay length. Despite the type of the excitation and its nonlinear features, the tail analysis predict the relation between the parent velocity and its localization, i.e. $V_i(\Lambda_i)$.

center. Tails are well described by the expression

$$u_n = \exp\left(-\xi\left(n - Vt\right)\right)\exp\left(\mathrm{i}\left(qn - \omega t\right)\right)\,, \tag{1.7}$$

where $|\xi|$ is the localization parameter and its inverse $\Lambda = 1/|\xi|$ the decay length. This equation is valid for $n > Vt$ if $\xi > 0$ and it corresponds to the front tail of the structure, where for $n < Vt$ if $\xi < 0$ corresponding to the back tail. The limit case $\xi = 0$ corresponds to extended phonons. Figure 1.4 shows an example were two localized waves are numerically obtained presenting different tails and velocities.

Since the tail amplitude is by definition small, it satisfies the linear equation Eq. (1.4). Using that $u_{n+1} = \exp(-\xi + \mathrm{i}q)u_n$, $u_{n-1} = \exp(\xi - \mathrm{i}q)u_n$ and $\dot{u}_n = (\xi V - \mathrm{i}\omega)u_n$, substitution of (1.7) in (1.4) yields the following two equations:

$$\begin{aligned} \xi^2V^2 - \omega^2 &= 2c_0^2(\cosh(\xi)\cos(q) - 1) \\ \xi V\omega &= c_0^2\sinh(\xi)\sin(q)\,. \end{aligned} \tag{1.8}$$

As there are two equation with four unknowns, we can express two of them as ω and V as functions of the other two ξ and q. First, the frequency ω is given by:

$$\omega = \cosh(\xi/2)2c_0\sin(q/2) = \cosh(\xi/2)\omega_{\text{phonons}}\,. \tag{1.9}$$

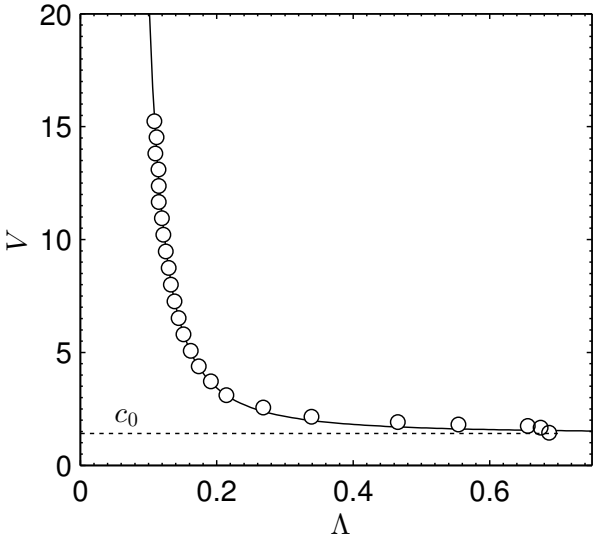


Figure 1.5: Comparison of the numerical (circles) and theoretical (continuous line) decay lengths as a function of the velocity for a localized wave (kink). Dimensionless units

Note that Eq. (1.9) reduces to the phonon dispersion equation when there is no localization, i.e. $\xi \to 0$.

The velocity of the tail of the hypothetical localized wave is given by:

$$V = \frac{\sinh(\xi/2)}{\xi/2}\, c_0 \cos(q/2) = \frac{\sinh(\xi/2)}{\xi/2} c_g \,. \tag{1.10}$$

The relationship between the decay length $\Lambda = 1/|\xi|$ and V given by the equation above is in excellent agreement with the numerical results, as can be seen in Fig. 1.5. Note that both $\sinh(\xi/2)/(\xi/2)$ and $\cosh(\xi/2)$ are larger than the unity and also monotonically increasing functions in $|\xi|$, which means that the tails oscillate and move faster than the phonons. Except for the degenerate case $\xi = 0$, which corresponds to no localization and no tail, i.e., to phonons. Essentially, the conclusion that arise for the tail analysis states that localized travelling waves, either solitons or kinks, with tails following Eq. (1.7) are supersonic, where its velocity depends on the localization. Also note this analysis was developed with the linearized discrete wave equation and does not depend of the specific nonlinearity of the coupling. Is thus generic for many systems of coupled oscillators. However, for studying the specific features of localized nonlinear travelling waves in the Coulomb lattice the nonlinear terms can not be neglected.

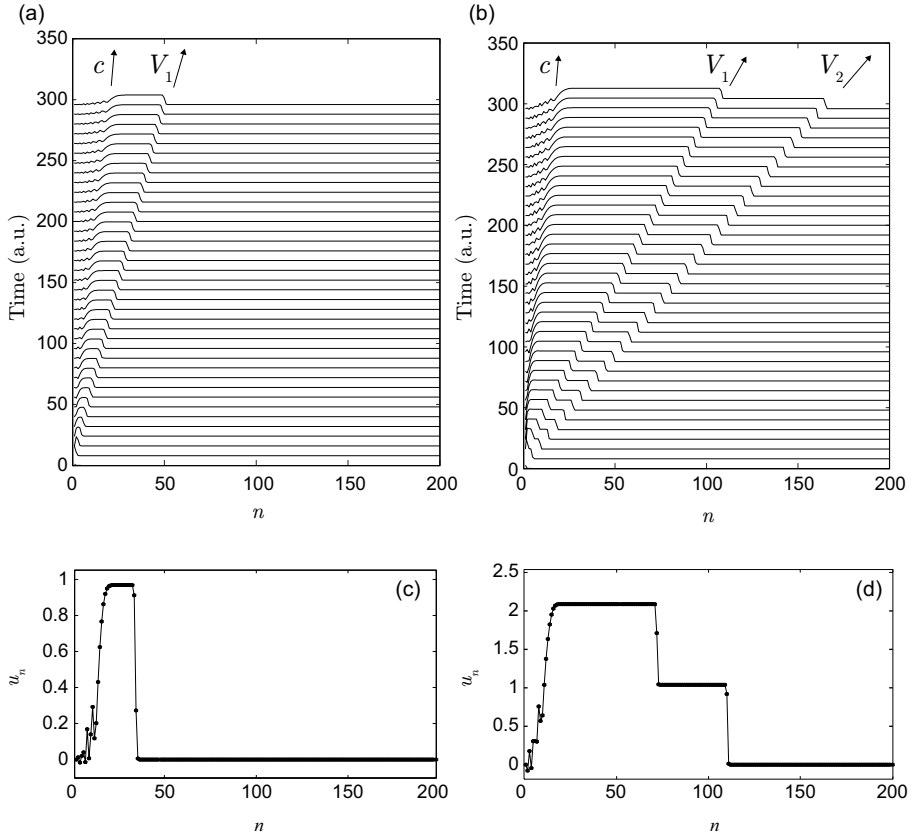


Figure 1.6: (a) Profile and evolution of a single kink for initial amplitude $A_0 = 1.05$. (b) Excitation of multikinks for initial amplitude $A_0 = 2.5$ where two kinks with different velocities are observed. (c,d) Detail of the corresponding displacements at $t = 200$ scaled units. A tail of phonons is left behind the localized travelling nonlinear waves.

1.4 Supersonic ultra-discrete kinks

1.4.1 First supersonic kinks and multi-kinks

We propose the study of kink solutions in the lattice. Essentially, a kink is a nonlinear localized wave that connects and divide two phases of the domain. Kinks can be stationary or propagating. We find that the simplified proposed model for the repulsive lattice is extremely well suited for propagation ultra-discrete supersonic kinks and multi-kinks. Due to the analytical analysis of the kink characteristics will be somehow restricted, a numerical integration of the complete set of equations of motion has been used to explore the full nonlinear features of the lattice.

The numerical evaluation of the Eq. (1.2) retaining the exact form of the Coulomb type interaction is trivial using centered finite differences with a "leap-frog" time marching scheme. Thus, for one-dimensional lattices of $N < 1000$ elements and the integration times considered on this Chapter, the temporal step required can be small enough to achieve convergence and the error due to numerical dispersion can be controlled for all simulations.

Thus, the boundary conditions for the simulations are set to fix at rest the first and last atoms of the chain, i.e. those conditions implicitly includes the effects of the other atoms of the mica crystal in the simplest way, forcing the central part of the chain to remain at rest. Then, a excitation is forced in one extreme of the chain. As a first example, as in Ref. (Kosevich et al., 2004), the first particle in the chain is forced to move sinusoidally during half a period, with an amplitude A_0, so that the initial and final positions are both zero (more details of this waveform will be given in following sections). Increasing the amplitude of the perturbation A_0 the velocity of the kink increases, and eventually, two, three, and any number of kinks are produced, travelling one after the other. The dependency of the velocity and number of kinks with the initial amplitude is shown in Fig. (1.6) for one (a, c) and for two (b, d) kinks.

1.4.2 Test solution

In order to obtain the properties of the full nonlinear system it is convenient to introduce a new variable, the deformation from the equilibrium position or *strain* $v_n = u_n - u_{n-1}$, the equations above can be written as:

$$\frac{\partial^2 v_n}{\partial t^2} = 2F_n - F_{n+1} - F_{n-1}; \quad \text{with} \quad F_n = \frac{1}{(1+v_n)^2}, \tag{1.11}$$

where $v_n = 0$ corresponds to the unperturbed lattice. The boundary conditions assume fixed particles at the ends of the lattice. Kinks are produced numerically by applying at the chain boundary a *half-wave* perturbation, which is a sinusoidal displacement during half of a period, starting and finishing at the equilibrium position (Archilla et al., 2013; Kosevich et al., 2004). In order to describe a kink traveling to the right, the following *ansatz* was introduced as in Refs. (Kosevich, 1993; Kosevich et al., 2004):

$$v_n = -\frac{A}{2}\left(1 + \cos\left(qn - \omega t\right)\right) \quad \text{if} \quad -\pi \leq qn - \omega t < \pi, \tag{1.12}$$

and $v_n = 0$ otherwise, where A is the kink strain amplitude. The bonds are always compressed so v_n is negative with a minimum value of $-A$, corresponding to the maximum compression of the bond. For analogy, we use the usual wave terminology, so $\phi_n = \omega t - q\, n$ is the phase; q is the wave number; ω is the angular

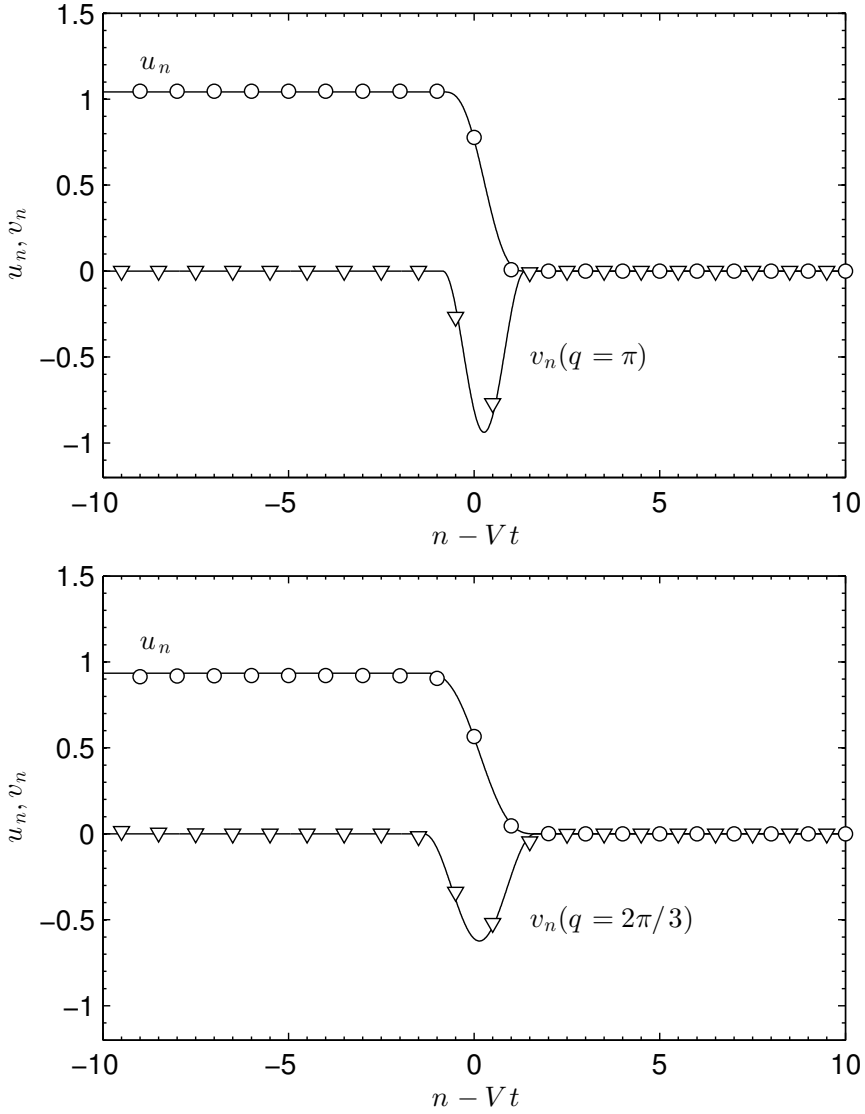


Figure 1.7: Spatial profile at fixed time for kinks represented in displacement (u_n) and strains $v_n = u_n - u_{n-1}$. Circles and triangles are numerical results and the continuous lines are obtained from Eq. (1.12) with *magic* wave number $q \simeq 2\pi/3$ (top), when basically two particles are moving at a given time, and with $q \simeq \pi$ (bottom) for the amplitude A close to 1, when basically one particle is moving at a given time. Scaled units are equal to the lattice unit.

frequency; T is the period; $\lambda = 2\pi/q$ is the wavelength. The sinusoidal waveform with $q = 2\pi/3$, being an exact solution for the FPU lattice(Kosevich, 1993; Kosevich et al., 2004), is not an exact solution for the Coulomb lattice but is a good approximation for intermediate values of the amplitude A and provides very useful framework for understanding the relative phases of the particles and the behavior of the kink.

Figure 1.7 (top) compares the result of the numerical simulation for displacements and strains, with the corresponding analytical expressions derived from Eq. (1.12), for the intermediate value of the amplitude $A = 0.55$ and wave number $q \simeq 2\pi/3$. The analytical expression fits very well the numerical data. Figure 1.7 (bottom) pictures a kink with wavenumber $q = \pi$. There are not enough particles to compare with the analytical form, but the main properties of the latter are valid.

For the dimensionless wave number $q = 2\pi/\lambda$, with λ an integer, Eq. (1.12) represents a solution where basically λ bonds and $\lambda - 1$ particles (the kink core) are in motion, while the others remain at rest.

We will use the term *active* to describe related states of the different magnitudes. The active particles or coordinates at a given time or time interval (or phase or phase interval) are those for which u_n is changing, the active bonds are those for which $v_n \neq 0$, i.e., they are the compressed ones. For a particle, the time interval is active when it is moving, and for a bond - when it is compressed.

If the dimensionless wavelength λ is between two integers m_1 and m_2, the number of active bonds oscillates between m_1 and m_2 and the number of active oscillating particles is between $m_1 - 1$ and $m_2 - 1$.

Of particular interest in this work will be $\lambda = 3$, with $q = 2\pi/3$, which is called the *magic wave number* (Kosevich et al., 2004), and $\lambda = 2$, with $q = \pi$, which will be referred to as the π-mode. These two values are extreme cases of localization, with $q = \pi$ being the limit when only one particle is moving at a given time.

1.4.3 Rotating wave approximation

The velocities of the kinks can be analytically obtained using the rotating wave approximation (RWA), which consists in an approximation of the Fourier series up to the first harmonic (Archilla et al., 2013). When we substitute (1.12) in the equation of motion (1.11), nonlinearity generates multiple frequencies. The RWA approximation states that nonlinear contributions higher than second harmonics can be neglected. This implies that the force terms can be approximated by their first-order Fourier expansions, as $F_n = a_0 + a_1 \cos(qn - \omega t)$. On the other hand, the left hand side of Eq. (1.11) gives, after substitution of Eq. (1.12), $\ddot{v}_n = (A/2)\omega^2 \cos(qn - \omega t)$ which is equal to the first harmonic term of the right hand side. The zero-harmonic cancels out due to the dependency of the right hand

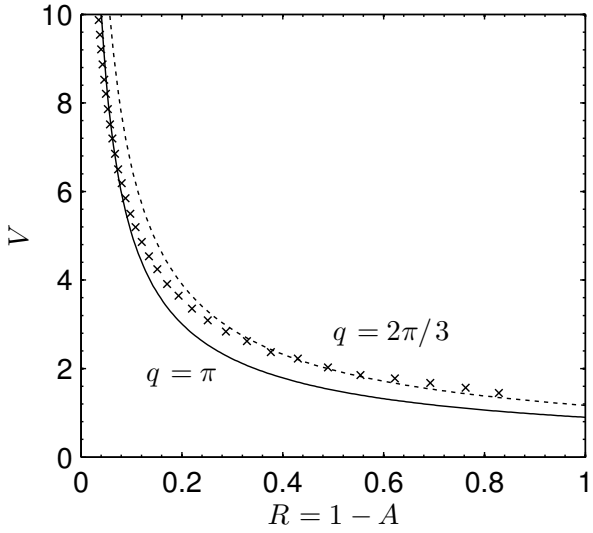


Figure 1.8: Kink velocity versus minimal interparticle distance $R = 1 - A$, calculated numerically (crosses) and analytically from Eq.(1.15) with wave number $q = 2\pi/3$ (upper dotted-dashed line) and $q = \pi$ (lower dotted-dashed line). Scaled units are the lattice constant for distances and 2.6 km/s for velocities.

side on F_n. The first harmonic of F_n is given by:

$$a_1 = \frac{1}{\pi}\int_{-\pi}^{\pi} \frac{\cos(\theta)\mathrm{d}\theta}{(1-\frac{A}{2}-\frac{A}{2}\cos(\theta))^2}\,. \tag{1.13}$$

For $A < 1$ we obtain

$$a_1 = \frac{A}{(1-A)^{3/2}}. \tag{1.14}$$

Therefore, substituting $\ddot{v}_n$ and $F_n = a_0 + a_1\cos(qn - \omega t)$ in Eq. (1.11), is straightforward to obtain the frequency as a function of the amplitude A:

$$\omega = \frac{1}{(1-A)^{3/4}}\, 2c_0 \sin\left(q/2\right), \tag{1.15}$$

and the velocity as:

$$V = \frac{1}{(1-A)^{3/4}}\; c_0\; \frac{\sin\left(q/2\right)}{(q/2)}. \tag{1.16}$$

Kinks are therefore supersonic. These magnitudes are equal to the corresponding ones for phonons, multiplied by a amplitude factor $1/(1-A)^{3/4}$: in the small

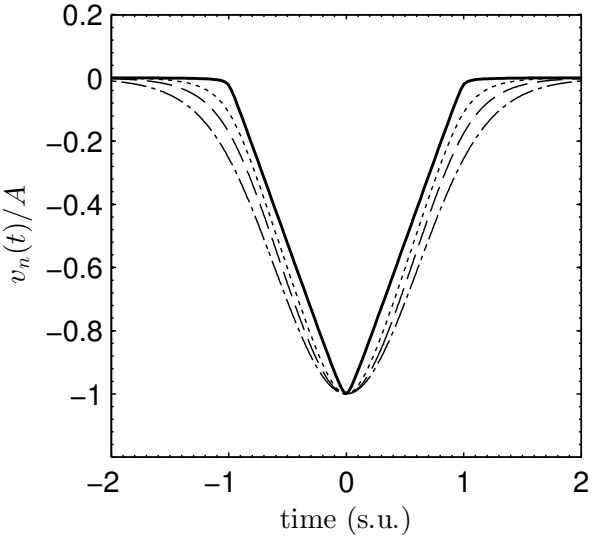


Figure 1.9: Temporal variation of the strain $v_n = u_n - u_{n-1}$ for different amplitudes. As the amplitude A increases, the shape becomes almost triangular, corresponding to almost hard-spheres collisions. The amplitude A is given in lattice units and the scaled time unit is 2 ps.

amplitude ($A \to 0$) and long wavelength ($q \to 0$) limit, V tends to the sound speed c_0.

In Ref. (Archilla et al., 2013) it was shown that the magic wave number represents a good agreement between the *ansatz* and simulations. However this agreement fails at the kink amplitudes A approaching unity, when the minimal interparticle distance in the kink (in lattice units) $R = 1 - A$ diminishes and the $q = \pi$ brings about a much better fit as can be seen in Fig. 1.8. The conclusion is that the magic wave number is a suitable approximation for an intermediate range of amplitudes in the Coulomb lattice, in contrast to the FPU chain where it is valid for all amplitudes(Kosevich, 1993; Kosevich et al., 2004), and that q actually changes continuously with the amplitude in the Coulomb lattice. The complementary approach is to use Eq. (1.15) to find the values of the wave number q, with respect to the amplitude A or the velocity V. This will be shown in Fig. 1.14, where it can be appreciated that the magic wave number is a satisfactory solution only for the intermediate values of kink velocity in the Coulomb lattice.

1.4.4 Triangular waveform

For the higher amplitudes, with A close to 1, the waveform deviates from the sinusoidal one given by Eq. (1.12) and approaches instead the triangular waveform, which is shown in Fig. 1.9. The almost straight lines in such waveform mean that

the velocity is almost constant except during a very short interaction time. The system behavior is very similar to that of the hard-spheres model.

This waveform is also another way of looking at the mode $q = \pi$. In this mode only one particle is moving at a given time, which means that there are no forces on the particle acting from its neighbours (because it moves at constant velocity and those forces would accelerate it). Strictly speaking, the mode $q = \pi$ and an exact triangular waveform are unattainable because of the electrostatic Coulomb forces acting on the particles. However, if the energy of the particle is large with respect to the change in the potential during a large part of the path between collisions, the particle will move almost free during most of the time between collisions.

The triangular waveform has been described as the high-energy limit for the Lennard-Jones interatomic potential (Friesecke et al., 2002) and has been observed experimentally in a system of repelling magnets (Molerón et al., 2014). It is worth mentioning that the triangular waveform can also be related with strongly-stretched bonds in the high-energy limit in the potentials allowing for bond dissociation, like the Lennard-Jones potential. The strongly-stretched bonds result in finite (normal) thermal conductivity in one-dimensional systems with such interatomic potentials (Savin et al., 2014).

1.4.5 Analytical results

Sinusoidal waveform and mode with $q = 2\pi/3$

Some analytical results can be obtained in this model, see also (Kosevich et al., 2004). Let us consider the wavenumber $q = 2\pi/3$ and choose $t = 0$ for the time for which $\phi_n = q\,n - \omega t = 0$ at $n = 0$ after a change of the origin of n and t, but keep the notation n for generality. If we consider the time interval Δt: $-T/6 \leq t < T/6$, there are three active strains: v_{n+1}, v_n and v_{n-1}. At the end of the interval, that is at $t = T/6$, v_{n-1} becomes zero and v_{n+2} starts being perturbed, so all the indexes n of the particles will change in a unity.

During Δt, $u_{n'} = 0$ for $n' \geq n + 1$, u_n and u_{n+1} are changing but u_{n-1} has already attained the value $3A/2$, its final constant value as can be checked by direct sum of 1.12 for $q = 2\pi/3$. Also, $u_{n'} = 3\,A/2$ for $n' < n - 1$, their final value after the kink has passed over them as seen in Fig. 1.7. The active coordinates are therefore $u_n = -v_{n+1}$ and $u_{n-1} = -v_n + v_{n+1}$, i.e. the mode $q = 2\pi/3$ states that essentially two particles are moving at same time and there are tree active bounds.

After some algebra we get

$$\begin{aligned} u_n &= \frac{A}{2} + \frac{A}{2}\cos\left(\phi_n + 2\pi/3\right) \\ u_{n-1} &= A - \frac{A}{2}\cos\left(\phi_n - 2\pi/3\right) . \end{aligned} \tag{1.17}$$

We can obtain immediately the kink kinetic energy as $K = \frac{1}{2}\dot{u}_n^2 + \frac{1}{2}\dot{u}_{n-1}^2$, which results in

$$K = \frac{\omega^2 A^2}{8}\left(1 + \frac{1}{2}\cos\left(2\phi_n\right)\right) , \tag{1.18}$$

with maximum value

$$K_M = \frac{\pi^2}{12} V^2 A^2 . \tag{1.19}$$

The potential energy, with respect to the equilibrium state, is given by:

$$U = \frac{1}{1+v_{n-1}} + \frac{1}{1+v_n} + \frac{1}{1+v_{n+1}} - 3 . \tag{1.20}$$

By substitution, it can be seen that the maximum potential energy corresponds to the bond n at its maximum compression, i.e., with $\phi_n = 0$, while the bonds $n-1, n+1$ have a phase difference of $\pm 2\pi/3$ with a strain $u_{n-1,n+1} = -A/2\left(1 + \cos\left(\pm 2\pi/3\right)\right) = -A/4$. Therefore the maximum energy becomes:

$$U_M = \frac{1}{1-A} + \frac{2}{1-A/4} - 3 . \tag{1.21}$$

There is also a minimum potential energy which corresponds to the limit, in which only two bonds are different from zero with phases $\pm\pi/3$ and strain $v_n = -3A/4$. The minimum energy becomes

$$U_m = \frac{2A}{1-3A/4} - 2 . \tag{1.22}$$

Therefore the kink for the mode $q = 2\pi/3$ has always some compression energy U_m above the ground state.

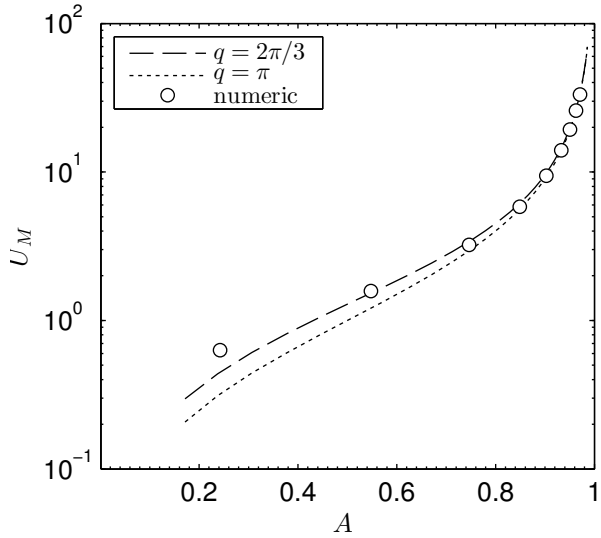


Figure 1.10: Maximum potential energies of the kinks in the Coulomb potential versus minimal interparticle distance in lattice units $R = 1 - A$ (for amplitude A close to 1). The analytical results are very similar for the waveforms with $q = \pi$ and $q = 2\pi/3$, as the maximum potential energy of the kink depends mainly on the minimal separation between particles R. The values of the dimension units are the lattice unit and 2.77 eV respectively.

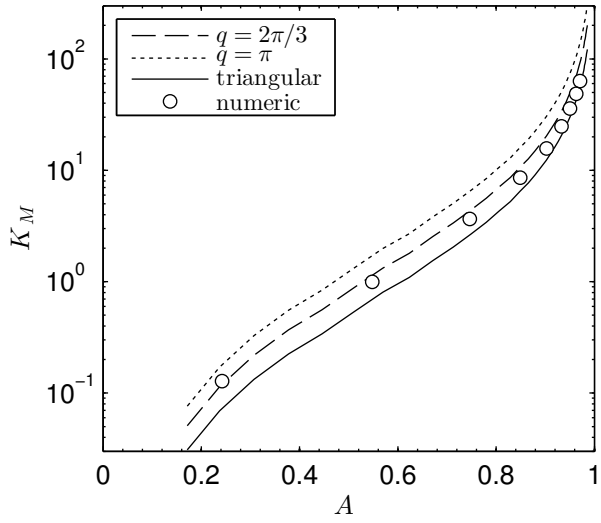


Figure 1.11: Maximum kinetic energies of the kinks in the Coulomb potential versus minimal interparticle distance in lattice units $R = 1 - A$ (for amplitude A close to 1). It can be seen that the kink with wavenumber π is better described by a triangular waveform than by a sinusoidal one. The values of the dimension units are the lattice unit and 2.77 eV respectively.

Sinusoidal waveform and mode with $q = \pi$

The properties of sinusoidal kinks with mode $q = \pi$ are easy to obtain as there are only two active strain variables and one coordinate, which during the interval $\Delta_\pi t$, $0 \le t < T/2$, are:

$$\begin{aligned} v_n &= -\frac{A}{2}\left(1+\cos\left(q\,n-\omega t\right)\right); \\ v_{n+1} &= -\frac{A}{2}\left(1+\cos\left(q[n+1]-\omega t\right)\right) = \\ &\quad -\frac{A}{2}\left(1-\cos\left(q\,n-\omega t\right)\right); \\ u_n &= -v_{n+1}\ ; \quad \dot{u}_n = \frac{A}{2}\omega\sin\left(q\,n-\omega t\right). \end{aligned} \tag{1.23}$$

The kinetic and potential energies, $K = \frac{1}{2}\dot{u}_n^2$ and $U = \dfrac{1}{1+v_n} + \dfrac{1}{1+v_{n+1}} - 2 = \dfrac{1}{1+v_n} + \dfrac{1}{1-v_n} - 2$, can be obtained. The maximum kinetic, maximum and minimum potential energies are given by

$$K_M = \frac{\pi^2}{8}A^2V^2\ ;\ U_M = \frac{1}{1-A} - 1\ ;\ U_m = \frac{2}{1-A/2} - 2. \tag{1.24}$$

Triangular waveform and mode with $q = \pi$

The potential energy fits very well the numerical values, unlike the kinetic energy, as can be seen in Figs. 1.10 and 1.11. This is because the π kink is better described by a triangular waveform in the limit of large energies, as Fig. (1.9) shows. Let us suppose that $t = 0$ is the time for which $v_n = -A$, as it takes half a period to change from $-A$ to 0, then $VT/2 = 2$. Therefore, for the interval $0 \le t < T/2$ the active variables for a ideal triangular waveform are:

$$\begin{aligned} v_n &= -A + AVt; \qquad & v_{n+1} &= -AVt; \\ u_n &= -v_{n+1} = AVt; \qquad & \dot{u}_n &= AV. \end{aligned} \tag{1.25}$$

The maximum and minimum potential energies are identical to that of the $q = \pi$ sinusoidal waveform given by Eq. (1.24).

On the other hand, the kinetic energy is a constant:

$$K = K_M = \frac{1}{2}A^2V^2\,. \tag{1.26}$$

In the numerical simulations, there are short time intervals when K changes, separated by a larger interval when K is almost constant.

In the high energy limit, $A \to 1$, the numerical solution converges to the triangular waveform: at fixed time only one particle is in movement, and its velocity is constant. During $0 < t < T/2$ the potential energy in this limit is negligible compared with the kink kinetic energy. Only when $t \to 0$ and $t \to T/2$ the moving particle *see* the Coulomb potential of the adjacent particles at rest. For $t \to T/2$ the particle experiment a deceleration, that in the limit $A \to 1$ can be considered as a rigid collision and therefore the kinetic energy must vanish for $t \to 0$ and for $t \to T/2$. Here a sharp peak on the potential energy is observed, where in the high amplitude limit a Dirac $\delta(t)$ is expected for energy conservation considerations.

Also, this result has implications in the interpretation of the kink as a particle-like excitation for high energies. In the limit $A \to 1$ the kink travels trough the lattice at constant velocity and energy, E, fixed by Eq. (1.26) as $E = \frac{1}{2}V^2$, which means that the kink behaves itself as a quasiparticle of unit mass (or a K^+ion mass in physical units).

1.5 Interaction with several neighbours

All the previous results apply to the case of nearest-neighbor coupling. However, for a more realistic description the long range interaction must be taken into account. With multiple neighbours, M, the dynamical equations become:

$$\frac{\partial^2 u_n}{\partial t^2} = \sum_{m=1}^{M} \left(-\frac{1}{\left(m + u_{n+m} - u_n\right)^2} + \frac{1}{\left(m + u_n - u_{n-m}\right)^2} \right), \tag{1.27}$$

which linearized become:

$$\frac{\partial^2 u_n}{\partial t^2} = c_0^2 \sum_{m=1}^{M} \frac{1}{m^3} \left(u_{n-m} - 2u_n + u_{n+m}\right). \tag{1.28}$$

Substitution of $u_n = \exp\left(\mathrm{i}\left(qn - \omega t\right)\right)$, leads to:

$$-\omega^2 u_n = c_0^2 \sum_{m=1}^{M} \frac{1}{m^3} \left(\exp\left(-\mathrm{i}qm\right) - 2 + \exp\left(\mathrm{i}qm\right)\right) u_n \tag{1.29}$$

with $c_0 = \sqrt{2}$, or:

$$\omega^2 = 4c_0^2 \sum_{m=1}^{M} \frac{1}{m^3} \sin^2\left(\frac{qm}{2}\right). \tag{1.30}$$

The function $\omega = \omega\left(q\right)$ is quite similar to the one with a single neighbour, but with a slope at $q = 0$ that increases with the number of neighbours. The phase

and group velocity are plotted in Fig. for the positive first Brillouin zone (1.12) for $M = 1, 3, 8, 50$. It is worth noting here that close to the continuous limit, i.e. $q \to 0$, $\sin(qm/2) \simeq qm/2$ and we obtain:

$$\omega^2 = q^2 c_0^2 \sum_{m=1}^{M} \frac{1}{M}. \tag{1.31}$$

Which leads to the group velocity at $q \to 0$ and $\lambda \to \infty$ $c_M = \partial\omega/\partial q$

$$c_M = c_0 \sqrt{\sum_{m=1}^{M} \frac{1}{m}}. \tag{1.32}$$

For a finite number of neighbours, the speed of sound is larger than with a single one. For example $c_3 = 1.354 c_0$ and $c_8 = 1.6486 c_0$. Note if causality is not imposed $\lim_{M\to+\infty} c_M = \infty$, although the convergence of is slow, e.g. for $M = 10^6$ neighbours $c_M = 3.7938 c_0$.

Simulation results show that kinks still exist and propagate supersonically when the Coulomb interaction extends beyond the nearest neighbours. Kinks have similar velocity and wave number if we normalize kink velocity to the sound speed in the Coulomb chain with interactions between M nearest neighbours, i.e. V/c_M.

Figure 1.13 shows the dependence of the relative velocity V/c_p on the minimum interparticle distance and Fig. 1.14 shows the dependence of the numerical best fit for the wave number as a function of the relative velocity, emphasizing the essential identity of the phenomenon. Other aspects of these figures will be commented below. For clarity, only the cases of three and eight neighbours are represented although up to 30 neighbours have been tested.

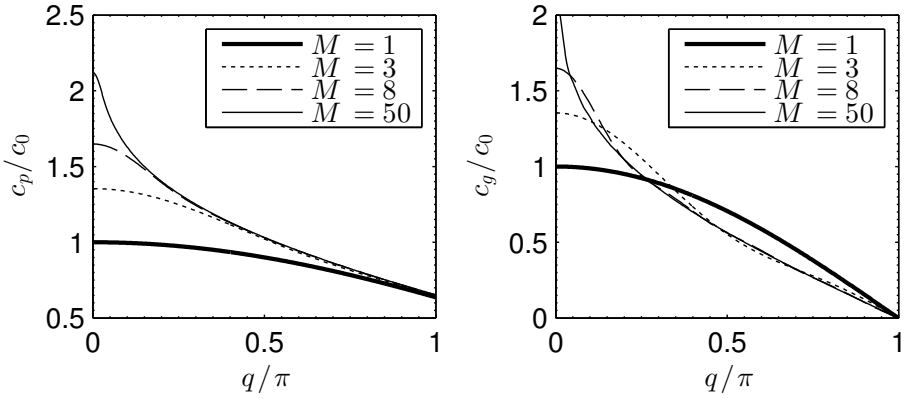


Figure 1.12: (left) Phase and (right) group velocity for the linearized Coulomb lattice including M=[1, 3, 8 and 50] neighbours.

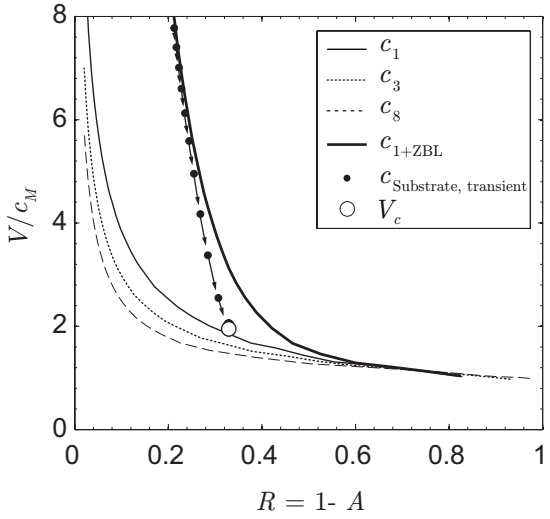


Figure 1.13: Kink velocities as a function of minimal interatomic distance in lattice units $R = 1 - A$ (A is kink's amplitude) for several potentials. Notations in the legend: c_m, $m = 1, 3, 8$, refers to the Coulomb interaction between the first m neighbours. Velocities are normalized to the sound speed c_M for a system with interaction between M neighbours, except for the system with a substrate which is normalized to $c_1 = c_s$. It can be seen that the increase of the number of interacting neighbours slows the normalized velocity V/c_M of the kink (but not its absolute velocity). Also, it can be seen that in the system with a substrate the normalized velocity V/c_M deviates from the curve $c_{1+\mathrm{ZBL}}$ to some specific velocity V_c on the c_1 curve. The values of the sound velocities are $c_1 = c_s = 3.7$ km/s, $c_3 = 5.0$ km/s and $c_8 = 6.1$ km/s.

It is worth commenting the problem that arises when the interaction with an infinite number of neighbours is taken into account. If the pair potential depends on the interparticle distance $|r|$ as $1/|r|^s$, the long-wave phonon velocity is finite for $s > 1$, but it diverges with the number of particles N as $v_{\mathrm{ph}} \propto \sqrt{\ln(N/2)}$ for the unscreened Coulomb potential ($s = 1$). However, this divergence occurs only in the electrostatic limit when the electromagnetic wave retardation is neglected. With an account of the retardation, the long-wave group velocity tends to the speed of light in vacuum. If the particles are in a material medium, there is a rearrangement of the electron density that can be described as a screening of the Coulomb interaction with some characteristic length l_{scr}. The screening brings about a finite long-wave phonon velocity $v_{\mathrm{ph}} \propto \sqrt{\ln(l_{\mathrm{scr}}/a)}$, where a is the lattice constant. As it has been mentioned, we do not study in depth this problem here and have considered only a few neighbours for simplicity.

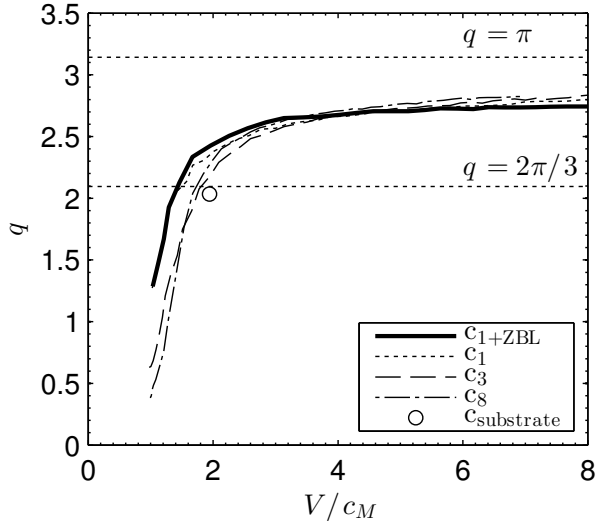


Figure 1.14: Best fit for the wavenumber q of the kinks as a function of the velocities normalized to the sound speed. Notations in the legend: C_i is the Coulomb interaction between the first i neighbours. Note that the *magic wave number* $q = 2\pi/3$ is also chosen in the system with a substrate. The values of the sound velocities are $c_1 = c_s = 3.7$ km/s, $c_3 = 5.0$ km/s and $c_8 = 6.1$ km/s.

1.6 The effect of nuclear repulsion: kinks with short–range ZBL potential

The minimal interatomic distance in lattice units $R = 1 - A$, obtained for fast large-amplitude kinks, is clearly impossible in realistic systems. At short distances short–range forces appear, which are produced by the overlapping electronic shells of the two close atoms. A large number of different repulsive potentials and screening functions have been proposed over the years, some determined semi-empirically, others from theoretical calculations. Much used repulsive potential is the one given by Ziegler, Biersack and Littmark, the so-called ZBL repulsive potential. It has been constructed by fitting a universal screening function to theoretically obtained potentials calculated for a large variety of atom pairs (Biersack et al., 2008). The ZBL potential has the form

$$U_{\mathrm{ZBL}}(r) = \mathrm{k_e}\,\frac{Z_1\,Z_2\,\mathrm{e}^2}{r}\,\phi\left(\frac{r}{\rho}\right)\,, \tag{1.33}$$

with $\mathrm{k_e}$ being the Coulomb constant, Z_1 and Z_2 are the atomic numbers of the involved atoms, and r the distance between them, $\phi(x)$ is the universal screening

Constant	$i=1$	$i=2$	$i=3$	$i=4$
A_i	0.1818	0.5099	0.2802	0.02817
b_i	3.2	0.9423	0.4029	0.2016

Table 1.1: Constants used for the Ziegler-Biersack-Littmark (ZBL) screening potential of Eq. (1.34)

function:

$$\phi(x) = \sum_{i=1}^{4} A_i \exp\left(-b_i x\right), \tag{1.34}$$

where the constants A_i and b_i are listed in Table (1.1).

The screening length is $\rho = 0.8854\, a_0 / \left(Z_1^{0.23} + Z_2^{0.23}\right)$, with $a_0 = 0.529$Å being the Bohr radius. The ZBL potential describes well the interaction between neutral atoms. In the case of ions considered here, the Coulomb potential must also be added, accounting for the repulsion between the ions. The introduction of the ZBL potential restricts the interatomic distances to the realistic values. The four terms in the ZBL potential are important for different range of energies, but for K^+ions, with energies up to 200 KeV, which are much larger that the ones considered here, the interaction potential can be represented by a single term, which together with the Coulomb ionic part takes the form:

$$U\left(r\right) = \frac{1}{r} + \frac{\alpha}{r} \exp(-\frac{r}{\rho}), \tag{1.35}$$

with $\alpha = 184.1$ and $\rho = 0.0569$ in dimensionless units, which in physical units correspond to 2650.6 eVÅand 0.29529 Å, respectively. Figure 1.15 represents ZBL and Coulomb potentials, with their sum and other details to be commented later. Note that around $r \simeq 0.4$, the combined potential $U(r)$ differs considerably from the Coulomb potential.

The dynamical equations become

$$\frac{\partial^2 u_n}{\partial t^2} = -G_{n+1} + G_n - F_{n+1} + F_n\,, \tag{1.36}$$

with F_n given by Eq. (1.11) and G_n given by

$$G_n = \frac{\alpha}{1+v_n} \exp\left(-\frac{1+v_n}{\rho}\right)\left(\frac{1}{1+v_n} + \frac{1}{\rho}\right). \tag{1.37}$$

When the joint effect of both the screened Coulomb (ZBL) and bare Coulomb potentials is considered, i.e., Eq. (1.35), numerical simulations show that the behavior of the kinks is not much different from that observed in the bare Coulomb

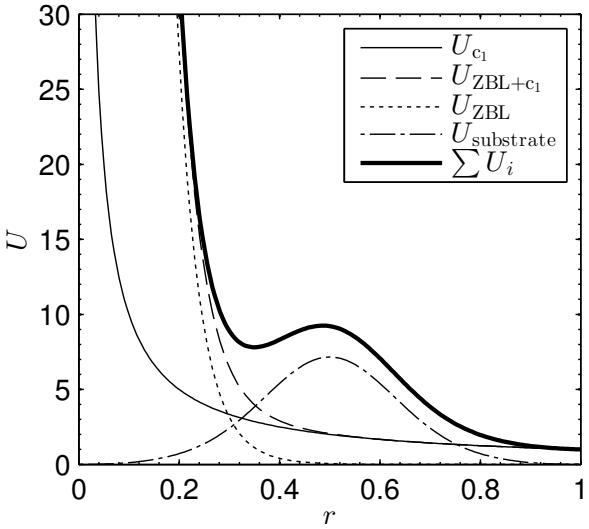


Figure 1.15: Interaction potentials U(r) in dimensionless units. Coulomb (c_1); ZBL (c_{ZBL}); Coulomb+ZBL ($c_{1+\mathrm{ZBL}}$); substrate potential (c_{S}) and the sum of the Coulomb, ZBL and substrate potentials ($c_{1+\mathrm{ZBL}+\mathrm{S}}$). The scaled units are 2.77 eV and the lattice unit a=5.19 Åfor U and r, respectively.

case, discussed in the preceding sections. Supersonic kinks propagate equally well, changing from the magic wavenumber $q = 2\pi/3$ to the proximity of $q = \pi$ and from the sinusoidal to nearly triangular waveform in increasing the amplitude A. Figures 1.13 and 1.14 also show the characteristic curves $V = V(A)$ and $q = q(A)$. The basic difference is that the high energy regime, i.e. the regime of high velocities at witch the waveform change from sinusoidal to triangular, is obtained for for lower (and also realistic) interatomic distances. On the other hand the sound velocity does not change since the ZBL potential is felt only for very large perturbations. Unfortunately, the RWA cannot be obtained analytically but the numerical RWA fits very well the results of the simulations.

1.7 The effect of the substrate potential: lattice kinks or crowdions

In the preceding sections, the interaction with the other atoms in the crystal was taken into account only implicitly, since the only effect of the surrounding atoms was to fix the equilibrium lattice period and to confine the particles within the crystal. To better model the properties of the kinks in a crystal like muscovite, we take into account explicitly the interaction with the surrounding atoms in a simplified mica geometry.

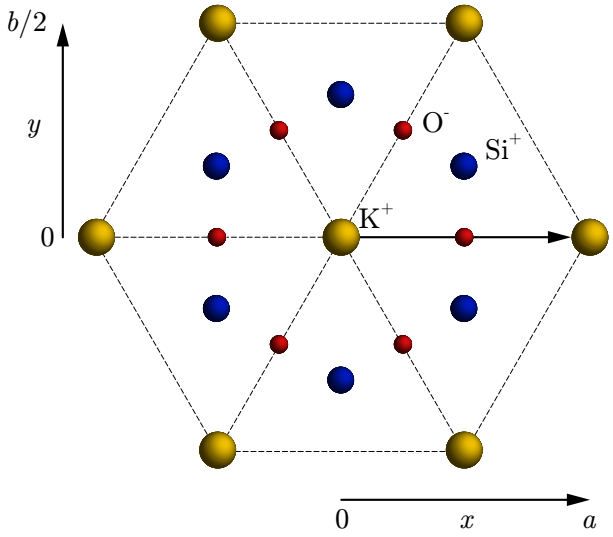


Figure 1.16: Projection on the [001] plane of the ions used in the calculation of the substrate potential. Four planes of ions are considered, two above and two symmetrical below the K^+plane, the closest two with oxygen and the other two with silicon ions. The path for the central K^+ion used the in calculation is shown, note that the O^{-2} ions in the middle of the path are actually at a distance of 1.68Å above and below. The interaction between the K^+ions in the central X-axis is not taken into account in constructing the substrate potential as it is taken into account explicitly. The crystal is continued in the K^+plane until the convergence is achieved. Distance between the longer marks is 1 Å.

The K^+ ions occupy the nodes of the hexagonal lattice with a lattice unit $a = 5.19$ Å. There are no other atoms in the K^+plane, therefore we need to consider more atoms above and below. We consider two planes above and two symmetric below. The closest plane, situated at a height of 1.6795Å, is occupied with oxygen ions with charge -2, their projections on the K^+plane lie in the middle of the two nearest-neighbor K^+ ions. The other layers, at at a height of 2.2227Å from the K^+ plane, are occupied by silicon ions. They are in the centers of tetrahedra whose three horizontal vertices are occupied by the oxygen ions. See the sketch on Fig. 1.16 for a projection of oxygen and silicon layers on the [001] plane, i.e. a top view of the K^+layer. The Si sites are occupied by Si^{+4} and Al^{+3} ions in the proportion of 3:1, giving an average charge of +3.75, but we assign them a smaller charge +2.75 to take into account other atoms in successive layers, particularly the oxygen ions at the top of the tetrahedra, and to achieve charge neutrality.

We suppose that all the atoms are in fixed positions except the moving K^+ ions in a row and only in the [100] direction. This is justified by the supersonic speed of the kinks, that we are interested in, and due to the weak interaction between the Si and Al ions compared to the ZBL interaction between potassium ions when they collide at high velocities. The interaction between the K^+ ions, that are in the central X-axis, are not considered in constructing the substrate potential as

it is taken into account explicitly. The lattice is extended in the [001] K^+ plane until the convergence of the potential is achieved. Specifically the potentials used are the electrostatic interactions and Born-Mayer potentials of the form $V = A\exp(-r/r_g)$, given in Ref. (Gedeon et al., 2002). The value $r_g = 0.29$Å is for all the interactions, and the pre-exponential constants in eV are: $A_{\mathrm{KO}} = 3800.125$, $A_{\mathrm{KSi}} = 2762.5$, $A_{\mathrm{OO}} = 453.375$, $A_{\mathrm{0Si}} = 1851.25$, and $A_{\mathrm{SiSi}} = 1173.125$. For the K^+-K^+ interaction, we use the Coulomb-ZBL potential described above.

We obtain a substrate potential in scaled units ($u_E \simeq 2.77$ eV), which can be described with very good approximation by a truncated Fourier series up to fourth harmonic:

$$U_s(x) = \sum_{h=0}^{4} U_h \cos(2\pi h x) , \tag{1.38}$$

with coefficients U_h equal to [2.4473, -3.3490, 1.0997, -0.2302, 0.0321]. The potential well of 20 eV is consistent with molecular dynamics simulations (Collins et al., 1992). It is represented in Fig. 1.15 together with the other potentials, such that their relative magnitudes can be compared.

1.7.1 Dispersion relations with substrate

Our dynamical equations with a substrate potential $U_s(x)$ in the form given by Eq. (1.38) and for M neighbour Coulomb interactions can be written as

$$\frac{\partial^2 u_n}{\partial t^2} = -\frac{\partial U_s(u_n)}{\partial u_n} + \sum_{m=1}^{M}\left(-\frac{1}{(m+u_{n+p}-u_n)^2} + \frac{1}{(m+u_n-u_{n-m})^2}\right), \tag{1.39}$$

where the restoring forces of the substrate potential are

$$-\frac{\partial U_s(u_n)}{\partial u_n} = \sum_{h=1}^{4} 2\pi h\, U_h \sin(2\pi h u_n) . \tag{1.40}$$

The latter equations, for small amplitude oscillations of u_n becomes

$$-\frac{\partial U_s(u_n)}{\partial u_n} \simeq -\omega_0^2 u_n , \tag{1.41}$$

with the linear frequency ω_0 as

$$\omega_0^2 = \sum_{h=1}^{4} (2\pi h)^2 U_h. \tag{1.42}$$

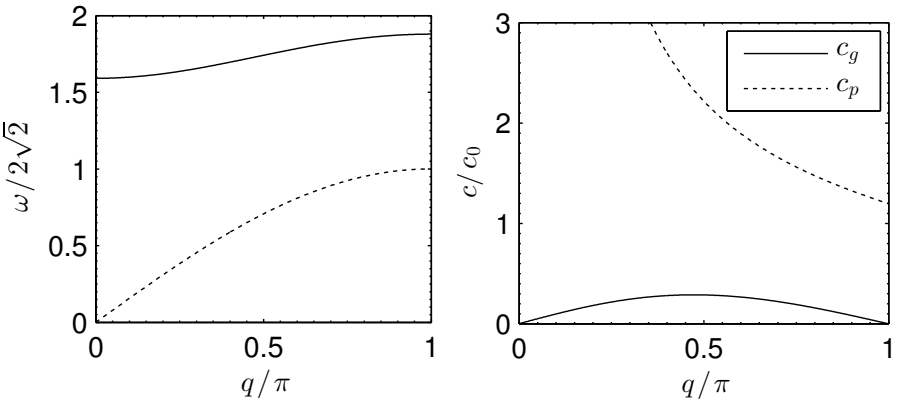


Figure 1.17: Left: Dispersion relation for the linearized Coulomb lattice with (continuous) and without (dotted) substrate potential. Right: Phase (dotted) and group (continuous line) velocity for linearized Coulomb lattice. All dispersion curves are for $M = 1$ neighbour interaction.

The corresponding value for linear frequency is $\omega_0 = 4.48$ or $119\ \mathrm{cm}^{-1}$ in physical units, which is close to $110\ \mathrm{cm}^{-1}$ determined experimentally (Diaz et al., 2000). Therefore the dynamical equations for u_n small become

$$\frac{\partial^2 u_n}{\partial t^2} = -\omega_0^2 u_n + c_0^2 \sum_{m=1}^{M} \frac{1}{m^3} \left(u_{n-m} - 2u_n + u_{n+m}\right) . \tag{1.43}$$

Substitution of $u_n = \exp(\mathrm{i}(qn - \omega t))$ leads to

$$-\omega^2 = -\omega_0^2 + c_0^2 \sum_{m=1}^{M} \frac{1}{m^3} \left(\exp\left(-\mathrm{i}qm\right) - 2 + \exp\left(\mathrm{i}qm\right)\right) . \tag{1.44}$$

Therefore the phonon dispersion relation become

$$\omega^2 = \omega_0^2 + 4\, c_0^2 \sum_{m=1}^{M} \frac{1}{m^3} \sin^2\left(\frac{qm}{2}\right) . \tag{1.45}$$

In the following we particularize for a single neighbour,i.e. $M = 1$. The phonon spectrum becomes an optical one, and the frequency and group velocity are

$$\begin{aligned} \omega^2 &= \omega_0^2 + 4\, c_0^2 \sin^2\left(q/2\right) , \\ c_g &= \frac{\partial \omega}{\partial q} = \frac{c_0^2 \sin q}{\sqrt{\omega_0^2 + 4\, c_0^2 \sin^2\left(q/2\right)}} . \end{aligned} \tag{1.46}$$

Note that c_0 is still the sound speed in the system *without* substrate. Thus, as Fig. (1.17) shows, the dimensionless phonon frequencies ω are in the interval

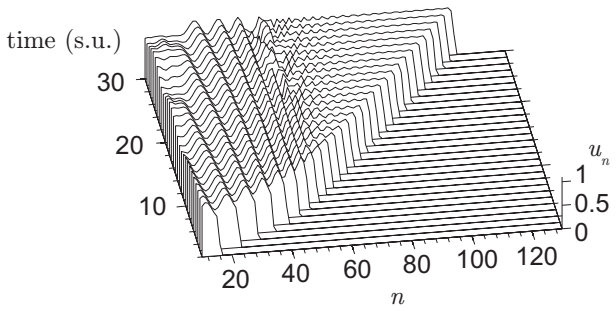


Figure 1.18: Representation of the process of dynamical slowing down of the kink. The nonlinear and linear radiation processes can be easily distinguished. Nonlinear waves with large amplitude are first emitted. Later, the phonons with the wavelength close to $\lambda \simeq 4$, which corresponds to maximal group velocity, and with exponentially decaying amplitudes are emitted while the kink approaches the limit velocity. Scaled units for time and distance are 0.2 ps and lattice constant 5.19 Å.

between $\omega_0 = 4.48$ and $\omega_{\max} = 5.31$. The group velocity is zero at $q = 0$ and $q = \pi$ and reaches its maximum $c_{\mathrm{c,max}} \simeq 0.4$, in the proximity of $q = \pi/2$ with $\lambda \simeq 4$. These features are also observed in the simulations for low amplitude travelling waves.

1.7.2 Qualitative description

The introduction of the substrate potential does not prevent the existence of supersonic lattice kinks. The lattice kink, also called *crowdion*, consists of an interstitial atom propagating very fast in the lattice and leaving behind a vacancy. The specific feature of the kinks found in the present work is that its velocity and energy are fixed by the layer+substrate system, let us denote them as V_c and E_c (c for crowdion). If the initial energy of the excitation is smaller than the threshold E_c, the kinks are rapidly dispersed and disappear and cannot propagate more than few lattice units. However, if it is larger, a kink is formed and its speed depends on its amplitude following the relation $V(A)$ of the ZBL interaction without substrate. However this velocity is not constant with time: the kink always slows down to a fixed stable speed V_c, and the excess energy is backward radiated. The specific values for the stable kink velocity and energy in scaled units are $V_c = 2.7387 \simeq 2c_0$ and $E_c = 9.4374$, corresponding to 7.16 km/s and 26.2 eV, respectively.

The lattice kink is supersonic in the two meanings a) $V_c > c_0$, where c_0 is the sound velocity without substrate; b) V_c is much larger than the maximum phonon group speed $V_{\mathrm{c,max}} \simeq 0.4$ in the system with the substrate, but is not larger than the maximum phase velocity which is unbounded for $q \to 0$, see Fig. (1.17).

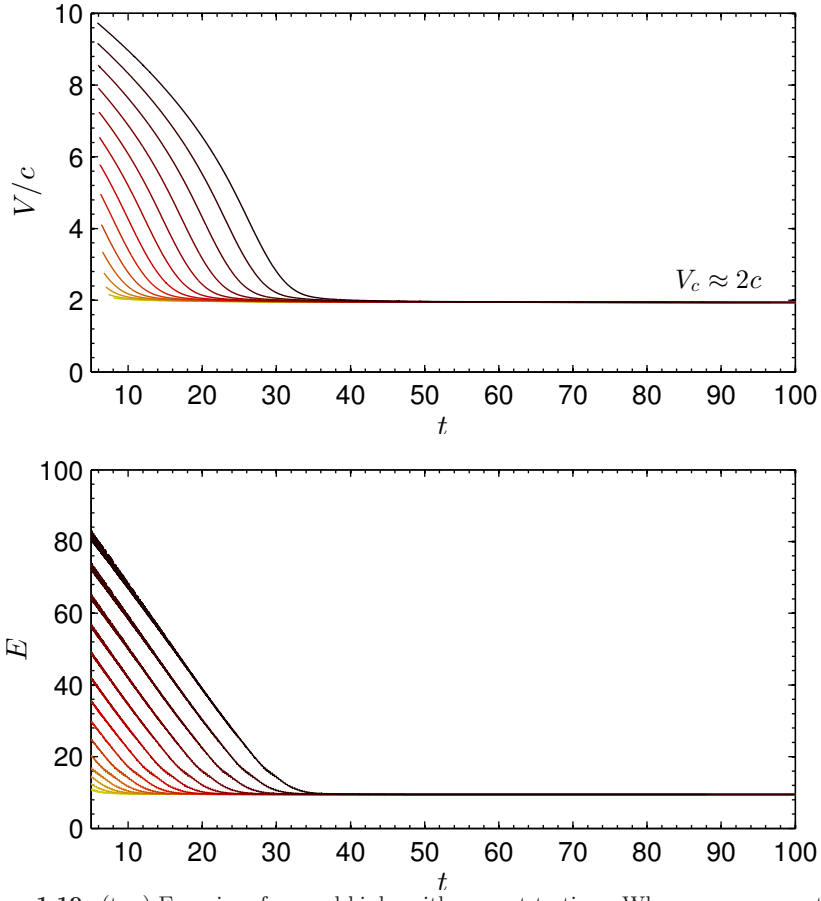


Figure 1.19: (top) Energies of several kinks with respect to time. When more energy than the crowdion's one is delivered a faster kink is produced and a radiation process takes place until the supersonic crowdion is formed. Thereafter, the crowdion is extremely stable. If the initial energy is smaller than the crowdion's one the kink dissipates into phonons. The scaled units are approximately 2.77 eV for energy and 0.2 ps for time. (bottom) Velocities of lattice kinks or crowdions versus time in scaled units for different initial conditions. The final velocity and energy are approached asymptotically, being $V_c = 2.7$ (7.2 km/s) and $E_k = 9.5$ (26.2 eV) in scaled and physical units. For $V < V_c$, the kinks are dissipated into low-amplitude phonons.

1.7.3 Slowing down processes

The process of slowing down to V_c is shown in Figs. (1.18) and (1.19), where two well distinguished phases can be identified.

a) **Nonlinear radiation:** For an initial energy $E > E_c$, the kink progressively loses energy. The particles immediately after the kink perturbation are left with enough energy for nonlinear vibrations in the potential well bringing about

nonlinear wave. Their frequencies obtained numerically are above the phonon band with a maximum value of about 6.3. This strong radiative process is shown in Fig. 1.18 for an initial velocity $V(t=0)=7$. This process is very fast and the decay of kink energy is almost linear with time. As long in this regime the waveform is nearly triangular, kink kinetic energy can be approximated by $K=\frac{1}{2}A^2V^2$ as explained is Sec. (1.4.5). Thus, as the potential energy is negligible for this regime, the linear decay of energy is consistent with the decreasing of velocity at the initial part seen in the of Fig. 1.19.

b) **Linear radiation:** As the lattice kink energy approaches E_c, the amplitude of the tail oscillations and its frequency decrease, the kink frequency enters the phonon band, radiating low amplitude phonons (Braun et al., 1998; Braun et al., 2004). The energy decreases exponentially with time towards E_c. The wave number of the radiated phonons can be deduced from the kink speed as each particle left behind the kink is excited with a delay $\Delta t = 1/V_c$ and, therefore, with a phase difference $q=\omega(q)\Delta t=\omega(q)/V_c$. As the phonon wave vector is given by $q=\omega(q)/c_{\rm ph}$, where $c_{\rm ph}$ is the phase speed of the phonons, $V_{\rm ph}=V_c$. Using the phonon dispersion relation in Eq. (1.46) it is possible to obtain the phonon wavenumber and wavelength $\lambda_{\rm ph}=3.5$ which is the observed one in the simulations. Similar process has been described in Ref. (Braun et al., 1998) and in references therein for subsonic kinks. However, there is an important difference: the subsonic kinks, described in those works, radiate continuously and eventually stop. Here the amplitude of the radiation decreases exponentially, allowing the kink to achieve a constant energy value and propagate stable along the lattice.

From the comparison of Figs. (1.13) and (1.19) with Fig. (1.15) we conclude that supersonic kink's amplitude A of relative particle displacements is determined by the interatomic distance R at the local *minimum* of the combined interatomic plus substrate potential, $R=1-A\approx 0.33$ in lattice units. This value of the kink amplitude ensures the absence of kink oscillations and correspondingly the absence of phonon radiation into the chain by the supersonic kink. We also want to emphasize that we do not observe discrete spectrum (a set of possible values) of the velocity of the supersonic kink in our system, even when we start with high initial kink velocity, see Fig. (1.19). This is in contrast with the prediction of supersonic multi-solitons (lattice N-solitons) in Frenkel-Kontorova model with nonlinear intersite coupling in Refs. (Braun et al., 2004; Savin, 1995; Zolotaryuk et al., 1997). We relate this finding with the extreme discreteness of our kink of effective wavenumber $q\simeq 2\pi/3$, which as shown in Fig. (1.14) corresponds to only two particles moving at a given time, cf. Ref. (Kosevich et al., 2004), which does not allow for different matching with the substrate potential, and also with possible dynamical instability of lattice multi-solitons (bound states of supersonic kinks) in the considered system.

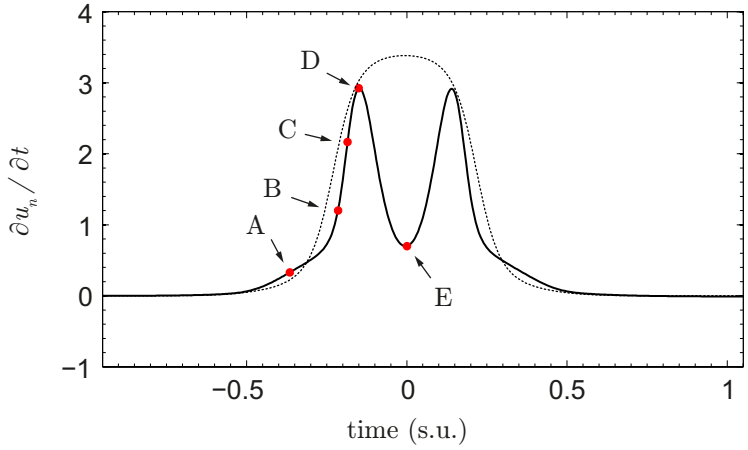


Figure 1.20: Particle velocity waveform measured at $n = 470$ in supersonic kink with amplitude $A = 0.67$ and minimal interatomic distance in lattice units $R = 1 - A = 0.33$ for Coulomb+ZBL potential with (continuous line) and without (dotted line) substrate potential. The instants when the ZBL interaction acts (near A) and the minimum velocity at the top of the potential barrier (E) are easily identified. The configurations at those times can be seen in Fig. 1.21. Scaled units are 0.2 ps and 2.6 km/s.

1.7.4 Double kink

The particle velocity $\dot{u}_n$ as a function of time for the stable kink in the substrate is represented in Fig. 1.20. Due to the extreme discreteness of the kink, it is not practical to represent $\dot{u}_n$ an a function of n. The profile of a double soliton for the particle velocity corresponds to the double kink shown in Fig. (1.21)-(a), is evident as a function of time.

Supersonic multi-solitons in Frenkel-Kontorova system with anharmonic coupling has been described in Refs. (Kosevich et al., 1973; Savin, 1995; Zolotaryuk et al., 1997). They correspond precisely to the discrete set of velocities for which the kinks do not radiate phonons. Although roughly similar in the shape, the kink in our system does not correspond to the mathematical forms obtained in those references. The kink in our system is more discrete, very close to the limit of discreteness, its wavenumber $q \simeq 2\pi/3$, shown in Fig. (1.14), corresponds to only two particles moving at a given time, cf. Ref. (Kosevich et al., 2004).

This discreteness makes possible the exact description of the double kink process as shown in Fig. 1.21 (c): a particle n, represented by a white circle, initially at rest at the bottom of a potential well, experiences two collisions, one when it was hit by the particle $n-1$ and is accelerated afterwards, and a second one when it hits the particle $n+1$ and is decelerated, attaining almost zero velocity at the

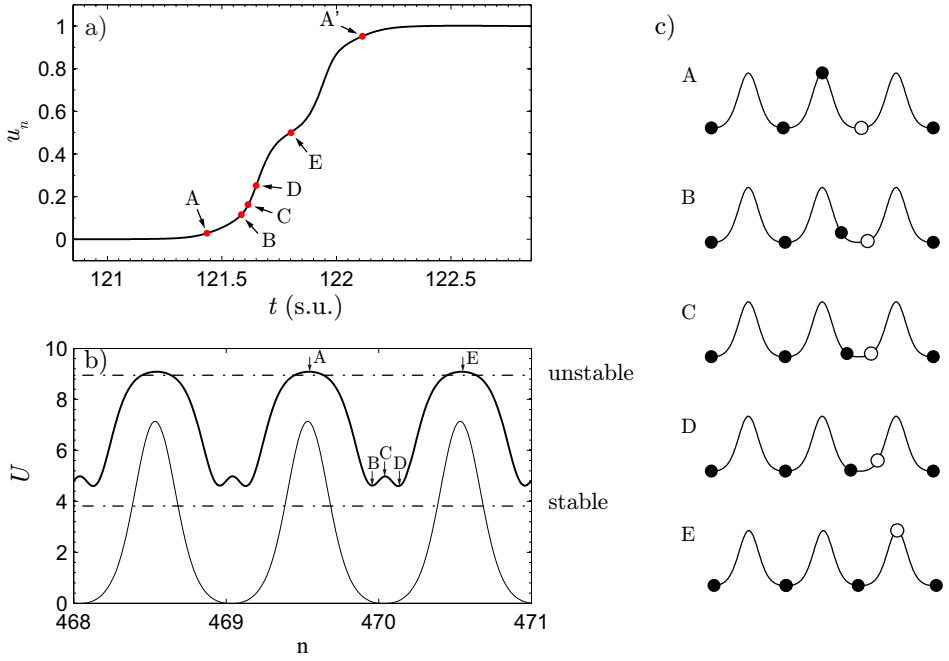


Figure 1.21: (a) Particle displacement waveform for the established lattice kink. (b) Potential energy seen by the kink during propagation (thick line) and periodic substrate potential (thin line), horizontal lines are the energies corresponding to the equilibrium stable (C) and unstable (A) interstitials. (c) Particle configurations corresponding to the points $A-E$, shown in (a) and (b). Scaled units are lattice unit 5.19 Å for distances, 0.2 ps for time and 2.77 eV for energies.

bottom of the potential well (during the radiation process the particle velocity is different from zero). Between the two collisions, the particle finds the substrate potential barrier between sites and experiences a decrease in velocity while going uphill which is followed by an acceleration while going downhill.

Note that the states A and E in Fig. 1.21 have exactly the same energy, but the kink has only moved half a lattice site. This is the first kink of the double-kink process shown in Fig. 1.21 (a). The process of the particle n going downhill and hitting the $n+1$ particle until it stops forms the second kink.

This process can be seen in terms of the kink energy in Fig. 1.21 (b). Two identical oscillations of particle's potential energy U happen for the kink to move a lattice site. There is a local maximum at point C, corresponding to the minimum distance between particles and the short range ZBL interaction. The horizontal dashed-dotted lines indicate the energies for the equilibrium interstitial configurations, with two particles inside a potential well (stable), or one particle at the top of the potential barrier (unstable), with the energy difference corresponding to the Peierls-Nabarro (PN) barrier. The potential energy is always above the stable interstitial energy as the lattice has no time to relax, bringing about an *adi-*

abatic PN barrier. The kink always has finite kinetic energy, with the minimum corresponding to configuration A.

1.8 Some numerical simulations with ultradiscrete kinks or crowdions

In this section we present the results of different simulations to show the capacity of the crowdions to survive a perturbed environment when larger energy is initially delivered and, second, the behaviour of the crowdions with temperature.

1.8.1 Excess energy

We present some examples of simulations when the lattice is given more energy than the 26.2 eV needed to produce the supersonic crowdion. The energies range from 130 eV to 520 eV. They are represented in Fig. 1.22. In (a) a single crowdion is formed after nonlinear waves are emitted. In (b) two crowdions are formed leaving behind an stationary linear wave. Note how the second crowdion survives to the tail of the first and the common velocity V_c of both. In (c) the excessive energy destroys the second crowdion which transforms into a highly localized nonlinear stationary wave. In (d) the second crowdion survives again, while in (e) it is again destroyed. Extensive phonon radiation and wandering kinks can be seen in the latter figure. In (f) a second crowdion survives 150 sites in a highly perturbed media but it is finally pinned down.

1.8.2 Thermalized medium

An interesting question is whether the crowdion can travel trough a previously thermalized medium. This is not only a question of general interest but particulary important for mica muscovite. As it has been calculated in the chapter *Tracks in mica: 50 years later* in this book, the recording process of tracks happens a few kilometers underground under large pressure and temperatures of 700-1000 K. Although much more work is necessary, the answer is positive. For comparison Fig. 1.23 (a-b) shows two simulations at 300 K and 1000 K in the system without substrate potential where the kink survives over hundreds of lattice sites. It is not really surprising as if we compare the energy of the crowdion 26.2 eV with the mean thermal energy of a particle k_BT, the crowdion energy is 1000 and 300 times larger at 300 K and 1000 K respectively.

In the case of including the substrate potential, as shown in Fig. 1.23 (c-d) for 300 K and 1000 K respectively, the crowdion can also travel hundreds of sites of the previously thermalized media. As it was studied in Ref. (Archilla et al.,

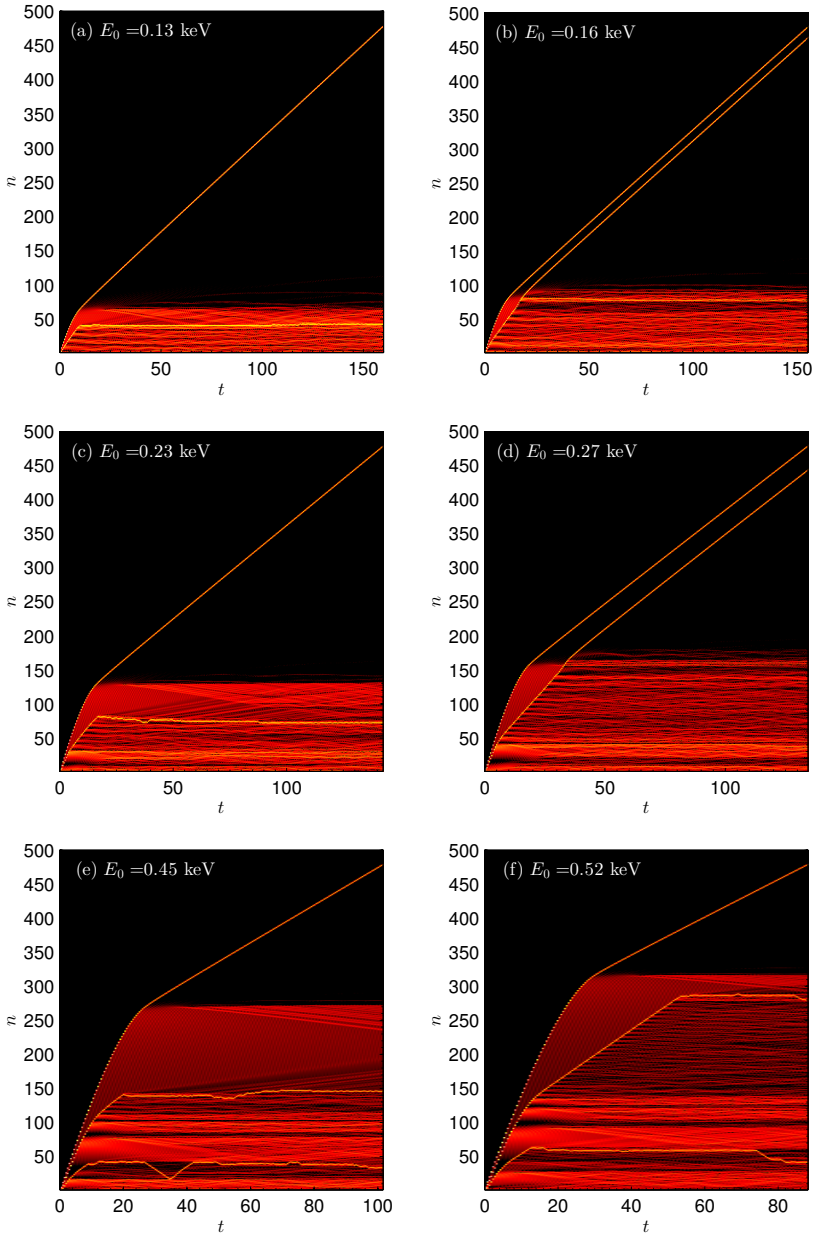


Figure 1.22: (Color) Particle energy plots of several examples of crowdion formation in arbitrary units of $\simeq 3$ eV. Initial energy increases form (a) to (f). Many features can be observed, among them the specific velocity of the crowdion V_c, the formation of nonlinear waves and phonons, the formation of two crowdions and the survival of the crowdion to the severely perturbed media during hundreds of sites

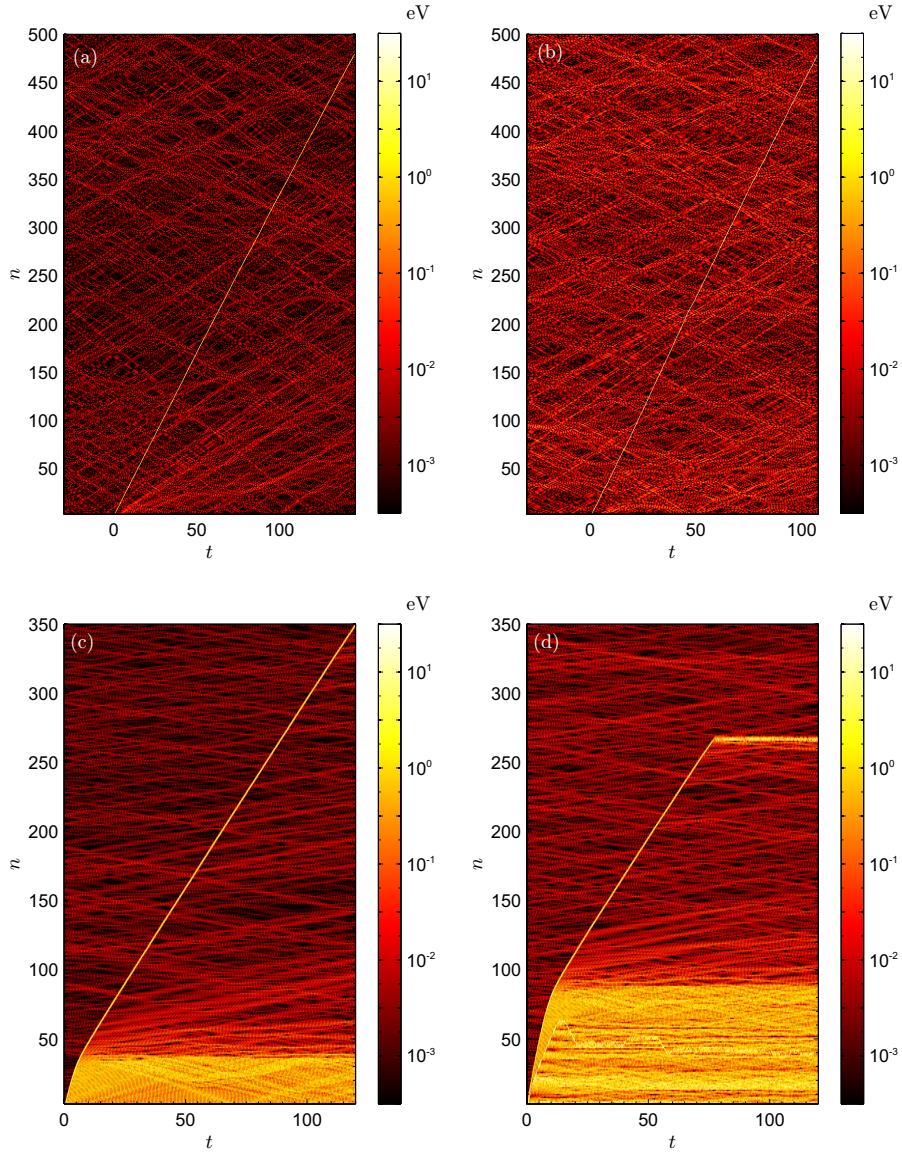


Figure 1.23: (Color) Particle energy plots of two crowdions travelling on a previously thermalized medium at (a,c) 300 K and (b,d) 1000 K, top without and bottom with substrate potential. Color bars are in $10\log_{10}(E)$ units

2015), the crowdion always has finite kinetic energy, but the final total energy of the kink, E_k, is always on the order of magnitude of the Peierls-Nabarro (PN) barrier. The equivalent kinetic energy equivalent for the thermalized media is 0.005

(0.013 eV) at 300 K and 0.016 (0.043 eV) at 1000 K in normalized and physical units . These values are far below the energy difference between the PN barrier and the kink energy. However, in some simulations, for temperatures of 1000 K the thermalization is not completely achieved due to appearance of nonlinear waves instead of phonons. Therefore, localized peaks of the background vibrations can interfere with the crowdion where, in some cases, it can be trapped leading to a highly localized nonlinear stationary perturbation. Figure 1.23 (d) shows and example of this situation, where the crowdion is eventually trapped forming an interstitial defect.

Thermal effects discussed in this section lead to different survival path length of the crowdions. It the hypothesis of crowdions propagating in mica muscovite is correct, they might be related with some the tracks observed in the mineral. Other feature of the presented simulations worth remarking is that the high equivalent temperature of the nonlinear tail radiation of the crowdion is likely to favor a change of structure and the formation of tracks.

1.9 Conclusions

In this chapter we have modeled a low dimensional system using realistic potentials corresponding to a row of ions in a silicate layer, mica muscovite sheet. Our objective was to determine what kind of nonlinear localized modes can exist with realistic parameters and with what characteristics. The choice of the parameters of mica muscovite is motivated by the fact that many of the dark tracks that appear in sheets of this material are consistent with the in-layer propagation of vibrational excitations along close-packed lattice lines of ions, and an experiment has demonstrated that localized energy can travel along lattice directions, being able to eject an atom at the opposite surface.

The modeling of the system has followed a process of increasing complexity to better understand which effect is responsible for which characteristic of the model. In the starting model in preliminary publications (Archilla et al., 2013; Archilla et al., 2014), only K^+ions with nearest-neighbor Coulomb repulsion were present, for which we have found that very fast supersonic kinks can propagate. They are extremely localized, only two particles or for higher energies only a single particle is moving at the same time.

We have added analytical calculations of the energies and compare them with numerical simulations. We have also shown that the introduction of interaction with several neighbours do not produce significant changes as long as the sound speed in each system is taken as a reference. But the extremely short minimal interatomic distances in the kink has motivated the introduction of more realistic short-range ZBL potential. In the improved dynamical model, kinks propagate equally well and with as much energy as desired, but now with realistic minimal

interatomic distances.

The next step was the introduction of a periodic substrate potential using empirical potentials and the geometry of the crystal. Supersonic kinks continue to propagate without losing energy but with several important properties:

a) The main one is that the system selects only one velocity and one energy of the kink;

b) The lattice kink energy is larger than the one which is needed for atom ejection at the surface, and smaller than the one of the proposed sources of energy, the recoil of a K^+ion due to beta emission;

c) The found kinks can be described as the double-kinks or bi-solitons depending of the variable chosen. The unique velocity of the supersonic kink on the periodic substrate potential we relate with the kink amplitude of relative particle displacements which is determined by the interatomic distance corresponding to the minimum of the combined intersite plus substrate potential.

The extreme discreteness of the system with basically two particles moving at the same time allows for the detailed interpretation of the observed double-kinks, which was not possible for multi-kinks without dispersion presented in other works. The double-kink structure is produced by the matching of the two collisions experienced by a particle and the process of going over the substrate potential barrier between neighboring sites. We have shown that realistic potentials allow for the propagation of ultra discrete lattice kinks with energies that are consistent with the properties observed in experiments. Although we cannot claim that those kinks are responsible for those phenomena, it seems likely that they play an important role.

References

Alba, M. D., A. I. Becerro, M. A. Castro, and A. C. Perdigón (2001). "Hydrothermal reactivity of Lu-saturated smectites: Part I. A long-range order study". In: *Amer. Mineral.* 86, p. 115.

Archilla, J. F. R., J. Cuevas, M. D. Alba, M. Naranjo, and J. M. Trillo (2006). "Discrete Breathers for Understanding Reconstructive Mineral Processes at Low Temperatures". In: *J. Phys. Chem. B* 110.47, pp. 24112–24120.

Archilla, J. F. R., Yu. Kosevich, N. Jiménez, V. Sánchez-Morcillo, and L. M. García-Raffi (2013). "Moving Excitations in Cation Lattices". In: *Ucr. J. Phys.* 58.7, pp. 646–656.

Archilla, J. F. R., Yuriy A. Kosevich, N. Jiménez, V. J. Sánchez-Morcillo, and L. M. García-Raffi (2015). "Ultradiscrete kinks with supersonic speed in a layered crystal with realistic potentials". In: *Phys. Rev. E* 91 (2), p. 022912.

Archilla, J.F.R., Y. A. Kosevich, N. Jiménez, V.J. Sánchez-Morcillo, and L.M. García-Raffi (2014). "Supersonic Kinks in Coulomb Lattices". In: *Localized Excitations in Nonlinear Complex Systems*. Ed. by R. Carretero et al. Springer, pp. 317–331.

Biersack, J., J.P. Ziegler, and M.D. Ziegler (2008). *SRIM - The Stopping and Range of Ions in Matter*. Published by J.P. Ziegler.

Braun, O M and Yu S Kivshar (1998). “Nonlinear dynamics of the Frenkel–Kontorova model”. In: *Phys. Rep.* 306, pp. 1–108.

Braun, O.M. and Yu.S. Kivshar (2004). *The Frenkel-Kontorova Model*. Springer.

Brudeylins, G. and D. Schmicker (1995). “Elastic and inelastic helium atom scattering at a cleaved mica sheet.” In: *Surf. Sci.* 333, pp. 237–242.

Chaikin, P. M. and T. C. Lubensky (1995). *Principles of Condensed Matter Physics*. Cambridge: Cambridge University Press, pp. 601–602.

Chaplot, SL and et al (2002). “Inelastic neutron scattering and lattice dynamics of minerals”. In: *Eur. J. Min.* 14, p. 291.

Collins, D R and C R A Catlow (1992). “Computer simulation of structure and cohesive properties of micas”. In: *Am. Min.* 77, pp. 1172–1181.

Collins, D.R., W.G. Stirling, C.R.A. Catlow, and G. Rowbotham (1993). “Determination of Acoustic Phonon Dispersion Curves in Layer Silicates by Inelastic Neutron Scattering and Computer Simulation Techniques.” In: *Phys. Chem. Miner.* 19, pp. 520–527.

Diaz, M, V. C. Farmer, and R Prost (2000). “Characterization and assignment of far infrared absorption bands of K^+ in muscovite”. In: *Clays Clay Miner.* 48, pp. 433–438.

Dou, Q., J. Cuevas, J. C. Eilbeck, and F. M. Russell (2011). “Breathers and kinks in a simulated crystal experiment”. In: *Discret. Contin. Dyn. S.-S* 4, pp. 1107–1118.

Dubinko, V. I., P. A. Selyshchev, and J. F. R. Archilla (2011). “Reaction-rate theory with account of the crystal anharmonicity”. In: *Phys. Rev. E* 83, p. 041124.

Durrani, S. A. (2001). “Nuclear tracks: A success story of the 20th century”. In: *Rad. Meas* 34, pp. 5–13.

Durrani, S. A. (2008). “Nuclear tracks today: Strengths, weaknesses, challenges”. In: *Rad. Meas* 43, S26–S33.

Fleischer, R.L. (2011). *Tracks to Innovation. Nuclear Tracks in Science and Technology*. Springer.

Frenkel, Ya. and T. Kontorova (1938). “-”. In: *Phys. Z. Sowjetunion* 13 (1), p. 1.

Friesecke, G. and K. Matthies (2002). “Atomic-scale localization of high-energy solitary waves on lattices”. In: *Physica D* 171.4, pp. 211 –220.

Gedeon, O., J. Machacek, and M. Liska (2002). “Static energy hypersurface mapping of potassium cations in potassium silicate glasses”. In: *Phys. Chem. Glass.* 43.5, pp. 241–246.

Hong, Z. L., H. Yoshida, Y. Ikuhara, T. Sakuma, T. Nishimura, and M. Mitomo (2002). “The effect of additive on sintering behavior and strength retention in silicon nitride with RE-disilicate”. In: *J. Eur. Ceram. Soc.* 22, p. 527.

Kosevich, A.M. and A.S. Kovalev (1973). “The supersonic motion of a crowdion. The one dimensional model with nonlinear interaction between the nearest neighbors”. In: *Solid State Commun.* 12, pp. 763–764.

Kosevich, Yu. A. (1993). “Nonlinear sinusoidal waves and their Superposition in anharmonic lattices.” In: *Phys. Rev. Lett.* 71, pp. 2058–2061.

Kosevich, Yu. A., R. Khomeriki, and S. Ruffo (2004). “Supersonic discrete kink-solitons and sinusoidal patterns with *magic* wave number in anharmonic lattices”. In: *Europhys. Lett.* 66, pp. 21–27.

Kudriavtsev, Y., A. Villegas, A. Godines, and R. Asomoza (2005). “Calculation of the surface binding energy for ion sputtered particles”. In: *Appl. Surf. Sci.* 239.3-4, pp. 273–278.

Milchev, Andrey (1990). “Breakup threshold of solitons in systems with nonconvex interactions”. In: *Phys. Rev. B* 42 (10), pp. 6727–6729.

Molerón, M., A. Leonard, and C. Daraio (2014). “Solitary waves in a chain of repelling magnets”. In: *J. Appl. Phys.* 115.18, p. 184901.

Ni, Y, Yu A. Kosevich, S. Xiong, Y. Chalopin, and S. Volz (2014). “Substrate-induced cross-plane thermal propagative modes in few-layer graphene”. In: *Phys. Rev. B* 89 (20), p. 205413.

Price, P. B. and R. M. Walker (1962). “Observation of fossil particle tracks in natural micas”. In: *Nature* 196, pp. 732–734.

Russell, F. (1988a). “Identification and selection criteria for charged lepton tracks in mica”. In: *Nucl. Tracks. Rad. Meas.* 15, pp. 41–44.

Russell, F. M. (1967a). “Duration of sensitive period for track recording in mica”. In: *Nature* 217, pp. 51–52.

Russell, F. M. (1967b). “Tracks in mica caused by electron showers”. In: *Nature* 216, pp. 907–909.

Russell, F. M. (1988b). "Positive charge transport in layered crystalline solids". In: *Phys. Lett. A* 130, pp. 489–491.
Russell, F. M. and J. C. Eilbeck (2007). "Evidence for moving breathers in a layered crystal insulator at 300K". In: *Europhys. Lett.* 78, p. 10004.
Savin, A. V. and Yu A. Kosevich (2014). "Thermal conductivity of molecular chains with asymmetric potentials of pair interactions". In: *Phys. Rev. E* 89 (3), p. 032102.
Savin, A.V. (1995). "Supersonic regimes of motion of a topological soliton". In: *Sov. Phys. JETP* 81, pp. 608–613.
Schlößer, D., K. Kroneberger, M. Schosnig, F. M. Russell, and K. O. Groeneveld (1994). "Search for solitons in solids". In: *Rad. Meas* 23, pp. 209–213.
Silk, E C H and R S Barnes (1959). "Examination of fission fragment tracks with an electron microscope". In: *Phylos. Mag.* 4, pp. 970–971.
Snowden-Ifft, D. P., E. S. Freeman, and P. B. Price (1995). "Limits on dark-matter using ancient mica". In: *Phys. Rev. Lett.* 74.21, pp. 4133–4136.
Wada, N and WA Kamitakahara (1991). "Inelastic neutron and Raman scattering studies of muscovite and vermiculite layered silicates." In: *Phys. Rev. B* 43, p. 2391.
Zolotaryuk, Y., J.C Eilbeck, and A.V. Savin (1997). "Bound states of lattice solitons and their bifurcations". In: *Physica D* 108, pp. 81–91.

Publications

The contents of this chapter has been presented in the following publications:

Journal papers

- Archilla, J. F., Kosevich, Y. A.; **Jiménez, N.**, Sánchez-Morcillo, V. and García-Raffi, L. M. "Ultradiscrete kinks with supersonic speed in a layered crystal with realistic potentials" *Phys. Rev. E*, 91, 022912 (2015)
- Archilla, J. F., Kosevich, Y. A., **Jiménez, N.**, Sanchez-Morcillo, V. and García-Raffi, L. M. "Moving excitations In cation lattices" *Ukranian Journal of Physics*, 58, 646-656 (2013)

Conference proceedings

- **Jiménez, N.**, Archilla, J. F., Kosevich, Y. A., Sanchez-Morcillo, V. and García-Raffi, L. M. "A crowdion in mica. Between K40 recoil and transmission sputtering" *Quodons in mica: nonlinear localized travelling excitations in crystals*, Altea, Spain. September 18-21, (2013)
- **Jiménez, N.**, Sánchez-Morcillo, V., García-Raffi, L. M. and Archilla, J. F. "Kinks supersónicos en redes repulsivas" *XXXIV Reunión Bienal de la Real Sociedad Española de Física*, Valencia, Spain. July 17, (2013)
- Archilla, J. F., Kosevich, Y. A., **Jiménez, N.**, Sanchez-Morcillo, V. and García-Raffi, L. M. "Effect of ZBL potential on kinks in repulsive lattices" *IV International Symposium on Strong Nonlinear Vibronic and Electronic Interactions in Solids*. Tartu, Estonia, May 1-3, (2013)

- Archilla, J. F., Kosevich, Y. A., **Jiménez, N.**, Sanchez-Morcillo, V. and García-Raffi, L. M. "Moving excitations in cation lattices" *Problems of theoretical physics* (dedicated to the 100th anniversary of Alexander Davydov). Kiev, Ukraine, October 8-11, (2012)
- Archilla, J. F., Kosevich, Y. A., **Jiménez, N.**; Sanchez-Morcillo, V. and García-Raffi, L. M. "Supersonic solitons and kinks in repulsive lattices" *Lattice Solitons and Irradiation-Induced Nonlinear Phenomena in Solids*. Tartu, Estonia, October 31-November 2, (2012)

Book chapters

- Carretero-González, R. & others (Eds.) **Localized Excitations in Nonlinear Complex Systems**, Springer (2014). Archilla, Juan F. R. and Kosevich, Yuriy A. and **Jiménez, Noé** and Sánchez-Morcillo, Víctor J. and García-Raffi, Luís M. "Supersonic Kinks in Coulomb Lattices", pp. 317-331 (2014),
- L. M. Archilla, J. F. R.; **Jiménez, N.**; Sánchez-Morcillo, V. J. & García-Raffi, L. M. (Eds.) **Quodons in mica: nonlinear localized travelling excitations in crystals**, Springer, (2015). Archilla, J. F., Kosevich, Y. A., **Jiménez, N.**, Sanchez-Morcillo, V. and García-Raffi, L. M. " A supersonic crowdion in mica: Ultradiscrete kinks with energy between $K^4 0$ recoil and transmission sputtering", pp 69–98 (2015).



Chapter 2

Nonlinear Acoustic Waves in Layered Media

Abstract

In this chapter we investigate numerically the propagation of a plane acoustic wave in a periodic medium in a structured fluid, formed by a periodic array of fluid layers with alternating acoustic properties. Periodic acoustic media such as 1D layered media, or 2D sonic crystals, are known to introduce strong dispersion in wave propagation, even creating forbidden propagation bands or bandgaps where wave propagation at particular frequencies is not allowed. We show how the nonlinear generation and propagation of the second and higher harmonics are strongly affected by the presence of the periodicity. Thus, the combined action of nonlinearity (harmonic generation) and periodicity (different propagation velocities and attenuation for the different harmonics) results in novel and unexpected phenomena with respect to the linear counterpart, and opens the door to new mechanisms of acoustic wave control and manipulation.

2.1 Introduction

In the previous chapter we have considered waves propagating in nonlinear lattices. Such lattices can be macroscopic, idealized as masses coupled by springs, or even microscopic, as atoms/ions coupled by electromagnetic forces. Lattices can be then considered of basic model of solid matter, with its elements distributed periodically in a regular array. Many properties of solids, such as thermal conductivity, can be interpreted in terms of fundamental vibrations of the lattice, or phonons.

The study of matter as a periodic medium (a crystal of atoms), was originally performed by Bloch and Brillouin (Brillouin, 2003) in the 30-40's, and gave rise to an entire new discipline in physics, the solid state (or condensed matter) physics. One of the most celebrated effects of wave propagation in periodic media are the appearance of forbidden propagation regions in the energy spectrum of electrons, or band-gaps. Most of the physics of semiconductors, and therefore many electronic devices, are somehow based on this concept. In the late 80's, these ideas where extended by Yablonovich and John to light waves (electromagnetic waves in general) propagating in materials where the optical properties like the index of refraction were distributed periodically. These materials were named, by analogy with metals, as photonic crystals. The typical scale is given by the wavelength. Actually, not only light but any wave propagating in a periodic medium may experience the same effects, and acoustic waves are not an exception. Sound wave propagation in periodic media has become very popular in the last 20 years in acoustics, after the introduction of the concept of sonic crystals. Exploiting the analogies with other type of waves many interesting effects, as the mentioned forbidden propagation bands (band-gaps), but also focalization, self-collimation, negative refraction, and many others have been proposed. We consider in this chapter the simplest case plane waves propagating in a 1D structure, formed by a periodic alternation of layers with different properties. Depending on the context, such a structure has been named a multilayer, a superlattice (particularly in the context of semiconductors) or a 1D phononic crystal (this include more exotic structures, as the granular crystal or lattice).

The huge majority of the studies considered so far have assumed a low-amplitude (linear) regime, neglecting the nonlinear response of the medium. Intense wave propagation in nonlinear periodic media, and in particular the case of sound waves, is almost unexplored. In this chapter we present different examples of new phenomena related to sound wave propagation in multilayers, where each of the layer has a nonlinear cuadratic elastic response. Nonlinear acoustical effects in such structure have been studied only in a few works. For example, in (Yun et al., 2005) the harmonic generation process is described in a fluid/fluid multilayered structure (water/glicerine), based in a nonlinear wave equation. Also, acoustic solitons in solid layered nonlinear media have been presented (Yong et al., 2003). More recently, nonlinearity plus periodicity has been considered in (Liang et al., 2009), where an asymmetric propagation device (acoustic diode) was proposed.

There, the nonlinearity and the periodicity appear in different position and its effect is consider separately.

The effects discussed in this Chapter are the result of the interplay between nonlinearity and periodicity. We mostly concentrate in two phenomena: the control of harmonic distortion and the generation and propagation of solitons in the multilayer. The first case is analyzed in depth, and the conditions needed to selectively act on the nonlinearly generated spectrum, and therefore manipulate the waveform in the desired way, are obtained and discussed.

The theory in this Chapter has been developed for fluid-fluid (scalar) structures, however the main conclusions are extendable to fluid-solid or to solid-solid multilayers, if particular conditions are given. Also, the main conclusions in the Chapter are independent on the regime of the waves (audible, ultrasound,...), and therefore on the size or scale of the structure. However, there is a domain, when ultrasound waves reach the Teraherz regime, where these ideas may find a great potential. The progress in miniaturization and the technological development allows currently to create multilayers at scales even in the nanometer range (each layer contains then a small number of atoms). This structures are usually made of semiconductors and are often used in particular applications as phononic mirrors to form phonon nanocavities, (Huynh et al., 2006) or microcavities to obtain a strong optomechanical coupling (Fainstein et al., 2013) (for a revent survey, see Huynh et al. (2015)). Notably, acoustic amplification was realized in doped GaAs/AlAs superlattices and recently a saser, for sound amplification by the stimulated (acoustic phonons) radiation was demonstrated, in a device including a superlattice gain medium and GaAs/AlAs SLs acoustic mirrors (Maryam et al., 2013).

Some phenomena are common to lattices and superlattices (both are nonlinear, dispersive, periodic media), and the results of this Chapter and the previous are connected. Harmonic generation has been described in granular chains, modeled by FPU equation. Such quadratic FPU is actually a basic model for lattices with different interaction potentials (like Hertz, Coulomb,...) for small displacements. The continuous limit of this equation gives the nonlinear acoustic equation, which actually connects the propagation of sound waves with the microscopic theory of matter.

2.2 Dispersion relations

We consider the simple case of a 1D periodic medium made of an arrangement of homogeneous fluid media of thickness a_i with varying material properties. For the shake of simplicity only longitudinal waves under normal incidence are considered. A scheme of the system is shown in Fig. 2.1.

The propagation of small amplitude waves in an infinite periodic system is completely described by its dispersion relation, often known as band structure,

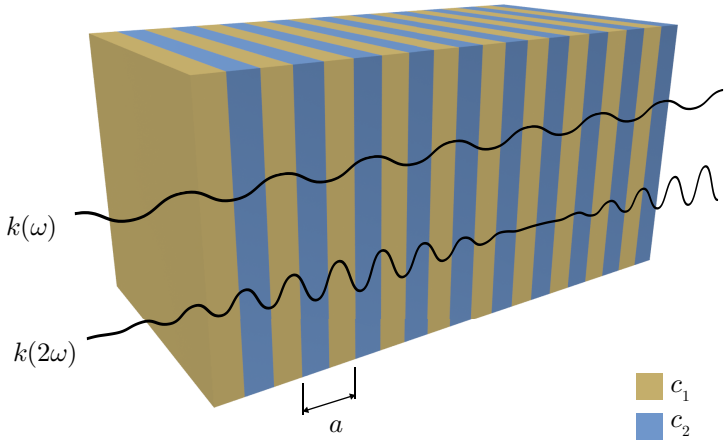


Figure 2.1: Layered acoustic system with two different layers and second harmonic generation scheme. Here the lattice period is $a = \sum a_i$.

that for 1D systems consisting in a periodic alternation of two different layers of length a_1 and a_2 can be expressed analytically as (Kosevich, 2005):

$$\cos(ka) = \cos(k_1 a_1)\cos(k_2 a_2) - \frac{1}{2}\left(\frac{k_1}{k_2} + \frac{k_2}{k_1}\right)\sin(k_1 a_1)\sin(k_2 a_2)\ , \qquad (2.1)$$

also known as the Rytov formula, where k is the Bloch wave-number, the lattice period is defined by $a = a_1 + a_2$ and $k_i = \omega/c_i$ with c_i the sound speed in the i layer. For a wave of frequency ω incident in a medium with known acoustical c_i and geometrical a_i parameters, the above equation results in a band structure of propagating and nonpropagating (bandgap) regions, as shown in Fig. 2.2. Thus, using Eq. (2.1), we can estimate the effect of periodicity on the different harmonics of the incident wave as they propagate trough the multilayer.

The ratio between layer thickness can be defined as

$$\alpha = a_1/a\,, \qquad (2.2)$$

leading to $a_2 = (1-\alpha)a$.

An example of dispersion relation plot is shown in Fig. 2.2 for normalized parameters $a = 0.5$ and for different sound speed ratios c_1/c_2. Increasing the impedance ratio between layers increases the reflected intensity in the trans-layer

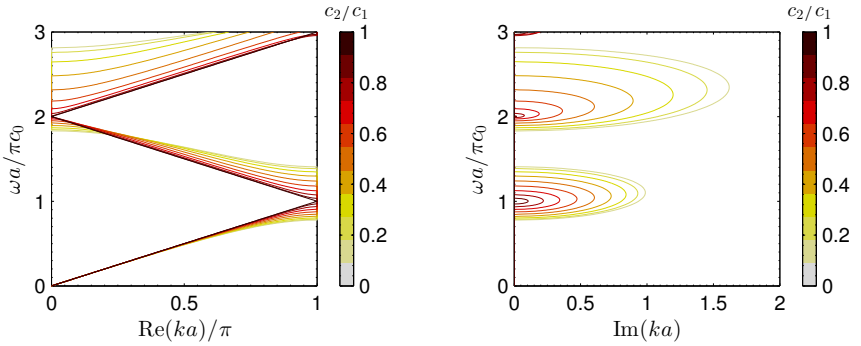


Figure 2.2: Dispersion relation of the two-layers system for layer proportion $\alpha = 0.5$ and for different c_2/c_1 ratio. Left: real wavenumbers. Right: imaginary part of the complex wavenumber.

propagation, while the transmitted energy of the multiple internal reflections diminishes. As can be seen, due to these scattering processes band-gaps are progressively open for wavenumber $k = n\pi/a$ with $n = 1, 2, ...$ Thus, the bandwidth of these band-gaps also increases when the impedance ratio grows.

On the other hand, its imaginary part increases in amplitude with c_1/c_2, leading to shorter evanescent propagation inside the band-gap for high sound speed contrast layers, while remains zero (no attenuation) in the propagation band. It is worth noting here that the system is conservative: the physical interpretation of the complex wavenumber is not energy absorption, but back reflection of the incident wave. Thus, at band-gap frequencies waves penetrate only a short distance into the medium with a forward evanescent mode, and if the medium is perfectly periodic and lossless the energy is back-reflected (it behaves as a mirror).

Furthermore, the curvature of the real part of the dispersion relations in the propagation band indicates dispersive propagation. However, in the low frequency regime the curve $\omega(k)$ is nearly linear. Here, a relation between c_1 and c_2 can be obtained for estimating the ratio in the limit $\omega \to 0$, $k \to 0$, that is the effective sound speed of the layered system $\tilde{c_0}$.

In order to obtain c_0 we first expand in Taylor series Eq. (2.1) in powers of ω around $\omega = 0$, and collecting terms up to second order we get

$$\omega \approx \sqrt{\left(1 - \cos\left(ka\right)\right) \frac{2c_1^2 c_2^2}{a\left(a_2 c_1^2 + a_1 c_2^2\right)}}. \tag{2.3}$$

Then, we expand again in Taylor series in powers of k around $k = 0$, and collecting terms up to first order we get

$$\tilde{c_0} = \frac{\omega}{k} \approx \sqrt{\frac{a c_1^2 c_2^2}{a_2 c_1^2 + a_1 c_2^2}}. \tag{2.4}$$

This value characterizes the layered media in the low frequency regime where the wavelength is much greater than the distance between layers. Furthermore, $\tilde{c_0}$ is useful also for frequency normalization, as long the first band-gap appears at $\omega = \pi\tilde{c_0}/a$ as can be appreciated in the common slope in the low frequency regime in Fig. 2.2. This quantity can be also obtained by assuming a mean density, $\tilde{\rho}$, and compressibility, $\tilde{\kappa}$ as (Yong et al., 2003):

$$\tilde{c_0} = \sqrt{\frac{\tilde{\kappa}}{\tilde{\rho}}}, \tag{2.5}$$

where the mean values for density and compressibility can be obtained as

$$\tilde{\rho} = \alpha\rho_1 + (1-\alpha)\rho_2\,, \tag{2.6}$$

$$\frac{1}{\tilde{\kappa}} = \frac{1}{\alpha\kappa_1} + \frac{1}{(1-\alpha)\kappa_2}, \tag{2.7}$$

being $\kappa_i = \rho_i c_i^2$ the compressibility of each layer.

2.3 Full-wave model

2.3.1 Nonlinear constitutive mode

The nonlinear propagation of sound in the acoustic inhomogeneous media, and in particular in multi-layered media can be described by several models, with different levels of accuracy. Here, we start from the equations of continuum mechanics for ideal fluids with space dependent parameters. Thus, applying mass conservation principle over a fluid control volume, the continuity equation reads (Naugolnykh et al., 1998):

$$\frac{\partial\rho}{\partial t} + \nabla\cdot(\rho\mathbf{v}) = 0\,. \tag{2.8}$$

On the other hand, the conservation of momentum over the same fluid test volume leads to the equation of motion

$$\rho\frac{D\mathbf{v}}{Dt} + \nabla p = 0\,, \tag{2.9}$$

where ρ is the total density, $\mathbf{v}$ is the particle velocity vector over a Eulerian reference frame, p is the acoustic pressure, t is the time and D is the material derivative operator

$$\frac{D}{Dt} = \frac{\partial}{\partial t} + \mathbf{v} \cdot \nabla \,. \tag{2.10}$$

For non homogeneous media, the ambient properties of the fluid in the absence of sound can be space dependent, so the total density becomes $\rho(t, \mathbf{x}) = \rho'(t, \mathbf{x}) + \rho_0(\mathbf{x})$, where $\rho_0(\mathbf{x})$ is the spatially dependent ambient density and $\rho'(t, \mathbf{x})$ is the perturbation of the density or acoustic density, that is space and time dependent. Then, using the material derivative, Eq. (2.9) becomes

$$\rho_0 \frac{\partial \mathbf{v}}{\partial t} + \nabla p = -\rho' \frac{\partial \mathbf{v}}{\partial t} - (\rho' + \rho_0)\,(\mathbf{v} \cdot \nabla)\,\mathbf{v} \,. \tag{2.11}$$

In this equation, the first two terms in the left-hand-side accounts for linear acoustic propagation, where the terms in the right-hand-side introduces nonlinearity in the Eulerian reference frame through momentum advection processes.

On the other hand, we can expand Eq. (2.8) for non-homogeneous media as

$$\frac{\partial \rho'}{\partial t} + \rho_0 \nabla \cdot \mathbf{v} + \mathbf{v} \cdot \nabla \rho_0 = -\rho' \nabla \cdot \mathbf{v} - \mathbf{v} \cdot \nabla \rho' \,. \tag{2.12}$$

Here, the first two terms on the left-hand-side account for linear acoustic propagation, the third, also linear, accounts for the magnitude of the changes in the ambient layer properties. Note this term is space dependent but only changes at the interface between adjacent layers. For density matched layers, $\rho_i = \rho_{i-1}$, this terms vanishes. The terms on the right-hand-side are nonlinear and accounts for mass advection. This equation remains exact.

Finally, a fluid thermodynamic state equation $p = p(\rho, s)$ is needed to close the system, with s the entropy. The local nonlinear media response relating density and pressure variations, retaining up to second order terms, can be written as

$$p = c_0^2 \rho' + \frac{B}{2A} \frac{c_0^2}{\rho_0} {\rho'}^2 \,, \tag{2.13}$$

where $B/A(\mathbf{x})$ is the quadratic nonlinear parameter and $c_0(\mathbf{x})$ is the sound speed, that can be also spatially dependent.

In this system of equations, quadratic nonlinearity appears in the equation of motion (2.11) and in the continuity equation (2.12), in the momentum and mass advection terms respectively, and also in the equation of state, Eq. (2.13), relating pressure and density acoustic perturbations. It is worth noting here that we only take into account nonlinear processes through the layer's bulk. The nonlinear effects at the boundary between adjacent sheets are neglected. These nonlinear boundary effects include cavitation processes, that in the case of fluids with very

different compressibility can be very important. In the case of solid layers, other local nonlinear effects relative to boundaries, e.g. clapping phenomena between surfaces, can lead to nonlinearities that are orders of magnitude in importance compared to the *bulk* cumulative nonlinearities (Tournat et al., 2004).

2.3.2 Second-order model

For moderate amplitudes, the system of Eq. (2.11-2.13) can be simplified. In the following, we use same ordering scheme as in Ref. Hamilton et al. (1998a), where $\mathcal{O}(\varepsilon)$, $\mathcal{O}(\varepsilon^2)$ and $\mathcal{O}(\varepsilon^3)$ represents the terms of generic smallness parameter ε. The derivation of a second-order nonlinear wave equation requires the substitution of the linearized acoustic approximations (first order) into second order terms of Eq. (2.12, 2.21). This substitution procedure will give third order errors, so the final nonlinear wave equation will be a second order approximation of the full constitutive relations.

Therefore, the first order equations of momentum and continuity can be obtained by linearization of Eq. (2.11-2.13) by assuming the acoustical magnitudes, ρ', p', and $\mathbf{v}$, are of small amplitude compared to the ambient values. Thus, for small amplitude perturbations the constitutive equations become

$$\frac{\partial \rho'}{\partial t} = -\rho_0 \nabla \cdot \mathbf{v} + \mathcal{O}(\varepsilon^2)\,, \tag{2.14}$$

$$\rho_0 \frac{\partial \mathbf{v}}{\partial t} = -\nabla p + \mathcal{O}(\varepsilon^2)\,, \tag{2.15}$$

$$\rho' = \frac{p}{c_0^2} + \mathcal{O}(\varepsilon^2)\,. \tag{2.16}$$

Then, we begin to manipulate the second order terms of the full constitutive relations with these first order approximations. Thus, using Eq. (2.14), the third right-hand-side term of the exact continuity Eq. (2.12) can be approximated up to second order as

$$-\rho' \nabla \cdot \mathbf{v} = \frac{\rho'}{\rho_0} \left(\frac{\partial \rho'}{\partial t} \right) + \mathcal{O}(\varepsilon^3)\,, \tag{2.17}$$

and using the linearized state Eq. (2.16) and rearranging terms leads to

$$-\rho' \nabla \cdot \mathbf{v} = \frac{1}{2\rho_i c_0^4} \frac{\partial p^2}{\partial t} + \mathcal{O}(\varepsilon^3)\,. \tag{2.18}$$

On the other hand, the fourth right-hand-side term of continuity Eq. (2.12) can be rewritten using the first order Eq. (2.15, 2.16) as

$$-\mathbf{v}\cdot\nabla\rho' = \frac{\rho_0}{2c_0^2}\frac{\partial u^2}{\partial t} + \frac{\mathbf{v}\rho'}{c_0^2}\nabla c_0^2 + \mathcal{O}(\varepsilon^3)\,. \tag{2.19}$$

Note that the last term of the above equation, that accounts for the local effect of the sound speed spatial variations, is $\mathcal{O}(\varepsilon^3)$, so it will be discarded, in contrast to the local effect of the ambient-density spatial variations (third term of Eq. (2.12)), that is $\mathcal{O}(\varepsilon^2)$ and it will remain in the derivation of the second order nonlinear wave equation for the layered media.

On the other hand, using the vector identity $(\mathbf{v}\cdot\nabla)\,\mathbf{v} = \frac{1}{2}\nabla v^2 - \mathbf{v}\times\nabla\times\mathbf{v}$ with $v^2 = \mathbf{v}\cdot\mathbf{v}$, and collecting terms up to second order, the equation of motion, Eq. (2.11), can be rewritten as

$$\rho_0\frac{\partial\mathbf{v}}{\partial t} + \nabla p = \frac{1}{2}\rho_0\nabla v^2 - \rho'\frac{\partial\mathbf{v}}{\partial t} + \rho_0\mathbf{v}\times\nabla\times\mathbf{v} + \mathcal{O}(\varepsilon^3)\,. \tag{2.20}$$

In general, although it is second order, the vorticity term (last term in the right-hand-side) decays exponentially away from rigid boundaries and can be discarded. However, it is essential to the analysis of other second order phenomena as the acoustic streaming (Hamilton et al., 1998a). In the following we will assume irrotational fluid. For a layered system, where the layer boundaries are orthogonal to the acoustic wave-vector, the vorticity modes can be neglected, while for strictly 1D propagation vanishes. Therefore, Eq. (2.20) becomes

$$\rho_0\frac{\partial\mathbf{v}}{\partial t} + \nabla p = -\frac{1}{2}\rho_0\nabla v^2 - \rho'\frac{\partial\mathbf{v}}{\partial t} + \mathcal{O}(\varepsilon^3)\,. \tag{2.21}$$

On the other hand, the second term of the right-hand-side of the above equation can be approximated up to second order using the first order Eqs. (2.14, 2.16) as

$$-\rho'\frac{\partial\mathbf{v}}{\partial t} = \frac{1}{2\rho_0 c_0^2}\nabla p^2 + \mathcal{O}(\varepsilon^3)\,. \tag{2.22}$$

Therefore, the second order approximation of the full constitutive relations in nonhomogeneous media can be expressed as:

$$\frac{\partial\rho'}{\partial t} + \rho_0\nabla\cdot\mathbf{v} + \mathbf{v}\cdot\nabla\rho_0 = \frac{1}{2\rho_0 c_0^4}\frac{\partial p^2}{\partial t} + \frac{\rho_0}{2c_0^2}\frac{\partial u^2}{\partial t} + \mathcal{O}(\varepsilon^3)\,, \tag{2.23}$$

and

$$\rho_0\frac{\partial\mathbf{v}}{\partial t} + \nabla p = -\nabla\left(\frac{1}{2}\rho_0 v^2 - \frac{1}{2\rho_0 c_0^2}p^2\right) + \mathcal{O}(\varepsilon^3)\,. \tag{2.24}$$

Using the definition of the Lagrangian density

$$\mathcal{L} = \frac{\rho_0}{2c_0^2}u^2 - \frac{p^2}{2\rho_0 c_0^2}, \tag{2.25}$$

the second order relations can be rewritten in a compact form

$$\frac{\partial \rho'}{\partial t} + \rho_0 \nabla \cdot \mathbf{v} + \mathbf{v} \cdot \nabla \rho_0 = \frac{1}{\rho_0 c_0^4}\frac{\partial p^2}{\partial t} + \frac{1}{c_0^2}\frac{\partial \mathcal{L}}{\partial t} + \mathcal{O}(\varepsilon^3)\,, \tag{2.26}$$

and

$$\rho_0 \frac{\partial \mathbf{v}}{\partial t} + \nabla p = -\nabla \mathcal{L} + \mathcal{O}(\varepsilon^3)\,. \tag{2.27}$$

These equations can be combined to form a unique nonlinear wave equation by subtracting the time derivative of Eq. (2.26) to the divergence of Eq. (2.26) to obtain

$$\nabla^2 p - \frac{\partial^2 \rho'}{\partial t^2} - \frac{\partial \mathbf{v}}{\partial t}\nabla \rho_0 = -\frac{1}{\rho_0 c_0^4}\frac{\partial^2 p^2}{\partial t^2} - \left(\nabla^2 + \frac{1}{c_0^2}\frac{\partial^2}{\partial t^2}\right)\mathcal{L} + \mathcal{O}(\varepsilon^3)\,. \tag{2.28}$$

Here, the third term can be expressed in terms of the acoustic pressure using the local instantaneous media response described by the state equation

$$\rho' = \frac{p}{c_0^2} - \frac{1}{\rho_0 c_0^4}\frac{B}{2A}p^2\,. \tag{2.29}$$

The fourth term of Eq. (2.28) can be also approximated using the first order Eq. (2.15), to finally obtain the second order nonlinear wave equation for nonhomogeneous media

$$\nabla^2 p - \frac{1}{c_i^2}\frac{\partial^2 p}{\partial t^2} - \frac{1}{\rho_0}\nabla \rho_0 \nabla p = -\frac{\beta}{\rho_0 c_0^4}\frac{\partial^2 p^2}{\partial t^2} - \left(\nabla^2 + \frac{1}{c_0^2}\frac{\partial^2}{\partial t^2}\right)\mathcal{L} + \mathcal{O}(\varepsilon^3)\,. \tag{2.30}$$

where we introduced the coefficient of nonlinearity $\beta = 1 + \frac{B}{2A}$ that accounts for material and mass advection quadratic nonlinearities. It is worth noting here (and discussed elsewhere (Hamilton et al., 1998a)) that the second-order Lagrangian density vanish for plane progressive waves due to the first order relation $p = uc_0\rho_0$ that leads to $\mathcal{L} = 0$. In this case, Eq. (2.28) simplifies to the well-known Westervelt equation for inhomogeneous media

$$\nabla^2 p - \frac{1}{c_0^2}\frac{\partial^2 p}{\partial t^2} - \frac{1}{\rho_0}\nabla\rho_0\nabla p = -\frac{\beta}{\rho_0 c_0^4}\frac{\partial^2 p^2}{\partial t^2} + \mathcal{O}(\varepsilon^3)\,. \tag{2.31}$$

In general, the Lagrangian density term can be discarded based on the distinction of cumulative and local nonlinear effects. In this way, for progressive quasi-plane wave propagation in homogeneous media the nonlinear local effects become insignificant in comparison to the nonlinear cumulative effects, where in most practicals situations, beyond a distance of only one wavelength away from the source local nonlinear effects can be neglected. However, local nonlinear effects can become significant in other complex situations including standing-wave fields. Concerning the layered media, in this Chapter we solve numerically the full constitutive relations, and we use the second order approximation Eq. (2.31) to obtain analytical solutions where the effect of the Lagrangian density term is assumed to be negligible.

2.3.3 Numerical solution

For one-dimensional acoustic waves $\mathbf{v} = (v_x, 0, 0)$, so the full constitutive relations Eqs. (2.8-2.11) can be expressed for nonhomogeneous media as

$$\frac{\partial \rho}{\partial t} = -\frac{\partial(\rho v_x)}{\partial x}\,, \tag{2.32}$$

$$\frac{\partial v_x}{\partial t} = -\frac{1}{2}\frac{\partial v_x^2}{\partial x} - \frac{1}{\rho}\frac{\partial p}{\partial x}\,, \tag{2.33}$$

The system of equations (2.13, 2.32-2.33) can be solved by several numerical methods (Botteldooren, 1996; Ginter et al., 2002; Vanhille et al., 2004; Albin et al., 2011). In this chapter we use the Finite-Differences in Time-Domain (FDTD) method: the density and pressure domain are discretized staggered in time and space respect to the particle velocity field, spatial and temporal derivatives are solved by centered finite difference operators, while the temporal integration is an explicit leap-frog scheme that consecutively solves density, pressure and particle velocity from continuity, momentum and state equations respectively. Thus, due to the 2-point stencil of the centered finite differences, the algorithm presents second order accuracy. Stability is achieved by the well-known Courant- Fiedrich-Levy (CFL) time step restriction and numerical FDTD dispersion is controlled due to a high enough grid refinement. Due to the low-dimensional space, a refinement > 100 elements per wavelength gives a negligible numerical dispersion compared to the physical one due to the layered system.

The dispersion relation (band structure) can be numerically obtained for the 1D system by a time-domain simulation of the linearized system. Linearization of

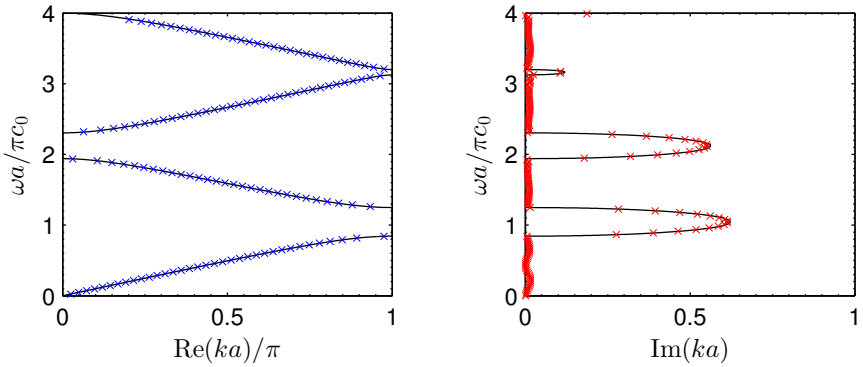


Figure 2.3: Dispersion relation of the two-layers system for normalized parameters $\alpha = 0.5$ and $c_2/c_1 = 0.5$. Left: real wavenumbers. Right: imaginary part. Rytov analytical Eq. (2.1) (Continuous line) and numerical solution (markers).

equations (2.13, 2.32-2.33) leads to the small amplitude version of Eq. (2.30), that is the nonhomogeneous wave equation, so both models present the exact same solution. Simulated pressure of Eqs. (2.13, 2.32-2.33) using a small amplitude excitation ($p_0 = 10^{-6}$ Pa or $\varepsilon = u_0/c_0 \approx 10^{-16}$) was recorded at two locations x_0 and x_1, located in different layers. Attenuation and phase velocity were estimated from the spectral components over the bandwidth of the recorded signals, that in this case was a numerical Dirac delta function in order to excite the entire numerical bandwidth. The numerical attenuation was calculated as

$$\alpha(\omega) = \frac{\ln\left(|P(\omega, z_2)/P(\omega, z_1)|\right)}{(z_1 - z_0)}\,, \tag{2.34}$$

where $P(\omega)$ is the Fourier transform of the measured pressure waveforms at points x_1 and x_2. On the other hand, the phase velocity was computed as

$$c_p(\omega) = \frac{\omega \cdot (z_2 - z_1)}{\arg\left(P(\omega, z_2)/P(\omega, z_1)\right)}\,, \tag{2.35}$$

where a correct phase unwrapping is needed in the arg function. Figure 2.3 shows the numerical and theoretical estimations of the dispersion relations, where excellent agreement is observed between them.

2.4 Harmonic generation in layered media

2.4.1 Overview

We start studying the response of the layered system for plane-harmonic wave excitation. Then, as sketched in Fig. (2.1), the source is placed in one boundary of the layered system, and the acoustic relevant magnitudes are calculated and measured along space and time. As the wave propagates, cumulative nonlinear effects generate harmonics of the fundamental frequency, ω_0, and due to the multiple scattering processes into the layers, local nonlinear effects also distorts the wave. However, the high dispersion of the layered system have a strong impact on the nonlinear harmonic generation. Dispersion modify the resonance conditions between fundamental and second harmonic wave, and also for other nonlinearly generated higher frequencies. In this way, nonlinear energy transfer efficiency from one component to another is modified in a wide variety of configurations, leading to the possibility of engineering and controlling the nonlinear wave processes by tuning the dispersion relation.

Figures 2.4 Figure 2.5 show an overview of the nonlinear harmonic generation over the propagation distance in a sample of layered media for normalized parameters $\alpha = 0.5$ and $c_2 = 0.7c_1$. From now on, if it is not explicitly said, the rest of the medium parameters are kept constant for the sake of simplicity, namely $\rho_1 = \rho_2$ and $B_1/A_1 = B_2/A_2$. If the frequency of the fundamental wave is varied, the harmonic generation exhibit various phenomena depending on the dispersion relation (plotted on the left of Fig 2.4a and Fig. 2.4b). Thus, we difference different frequency areas that will be explained below. It is worth noting here that the specific limiting frequency values and bandwidth between areas are strongly depending in the layered parameters However, the ordering of zones for different phenomena are, in general, the following:

(A) **Fubini-homogeneous**: The first zone is the very-low frequency band where the dispersion relation is nearly flat not only for the fundamental wave, but also for higher spectral components. In this region, the layered system behaves as an homogeneous material with effective parameters and dispersion can be neglected.

(B) **Weak-dispersion**: As the frequency is increased dispersion start to appear and different harmonics propagate with different wave speed. In the low dispersive regime, second harmonic dispersion is weak and even can be neglected, but third harmonic experiment strong dispersion and higher harmonics can fall in a band-gap where its propagation will be evanescent. Due to this situation, the energy transfer from the fundamental to its second harmonic is almost constant, and the second harmonic grows linearly with propagation. However, higher order cascade processes can be modified due to dispersion and the energy transfer from second to higher harmonics is decreased. This

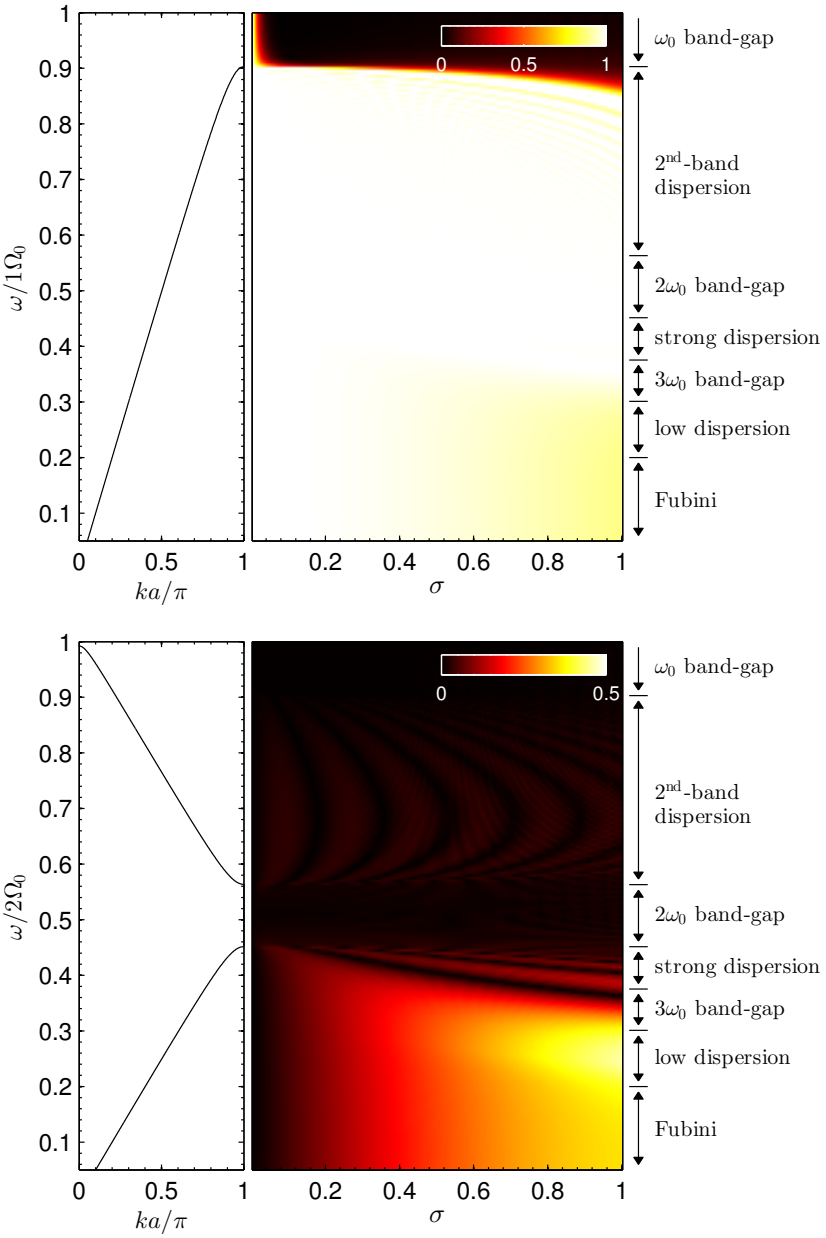


Figure 2.4: Overview of the harmonic generation processes in a nonlinear layered acoustic media. Top: fundamental component field, bottom: second harmonic field. Left: dispersion relation of the two-layers system for normalized parameters $\alpha = 0.5$ and $c_2/c_1 = 0.7$. Right: pressure amplitude (color) normalized to the source amplitude versus fundamental wave (ω) frequency and distance normalized to shock distance (σ)

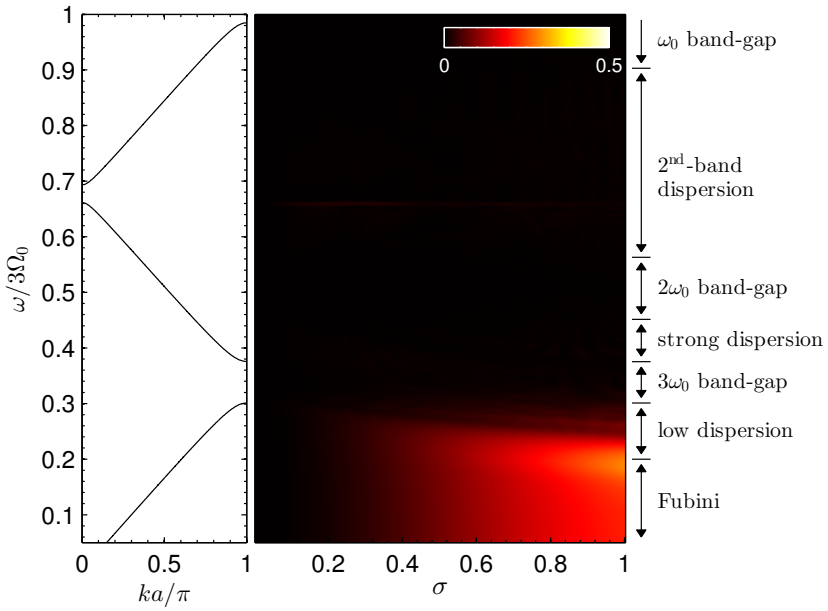


Figure 2.5: Overview of the harmonic generation processes in a nonlinear layered acoustic media for third harmonic. Left: dispersion relation of the two-layers system for normalized parameters $\alpha = 0.5$ and $c_2/c_1 = 0.7$. Right: pressure amplitude (color) normalized to the source amplitude versus fundamental wave (ω) frequency and distance normalized to shock distance (σ)

situation avoids the emergence of shocks and underthat conditions the second harmonic amplitude can overcomes the second harmonic field amplitude observed in the absence of dispersion.

(C) 3rd **harmonic in band-gap**: In this frequency area the propagation of third harmonic is evanescent and, in general, strong dispersion is observed on the second harmonic.

(D) **Strong-dispersion**: Where strong dispersion is observed for the second harmonic component, its field develops beatings in space, where its amplitude and spatial frequency depends on the matching conditions.

(E) 2nd **harmonic in band-gap**: In this frequency area second harmonic propagation is evanescent and the field does not grow with distance, but achieves a nearly constant value, being locally forced by the first.

(F) 2nd **band dispersion**: When second harmonic is in the second band, a high variability of phenomena can be observed depending on the material parameters. In the sample plot in Fig. 2.4 the second harmonic develops oscillations whose period varies by changing the frequency due to different phase matching conditions. By tuning material parameters and frequency different phase

matching conditions can be obtained, leading to a wide variety of possibilities. A sample is observed in Fig. 2.5 for $\omega_0 = 0.6\Omega_0$, where third harmonic falls in the limit of the second band-gap and also phase-matching is higher for third that for second harmonic, leading to third harmonic field higher than the second for this specific situation.

(G) 1st **harmonic in band-gap**: When fundamental frequency falls in the band-gap evanescent propagation is achieved and only local nonlinearities can be exited. However, due to the imaginary part of the wavevector inside the band-gap, that depends on the frequency, (see Fig. 2.3), the length of the exponentially decaying propagation inside the layered media can be tuned and therefore second harmonic can be produced at the beginning of the layered media while fundamental cannot propagate at the exist of the system.

These scenarios will be studied in the following subsections.

2.4.2 Homogeneous-Fubini

We start studying the rpropagation in the layered system for harmonic excitation in the very low frequency regime, where we assume that $ka \ll 1$ holds. As the Rytov's Eq. (2.1) predicts, in the very low frequency regime the slope of the $\omega(k)$ curve is nearly flat, and after sound speed normalization using using Eq. (2.4), the dispersion of the layered system should be negligible. Thus, the medium behaves as a continuum-lossless homogeneous material with effective parameters. This is known as the homogenization limit. However, attention should be paid here if the fluid compressibility highly differs between layers because the validity of the effective parameters may fail. It is the case, for example, of a liquid with gas inclusions (bubbly liquids) (Gurbatov et al., 2011).

In limit of low-frequency, the dispersion of all the spectral components is negligible, and they all propagate at nearly the same velocity. Thus, in the absence of dispersion and attenuation process, the system of Eq. (2.13, 2.32-2.33) can be reduced for harmonic-plane wave to a Burger's evolution equation expressed in traveling coordinates with effective parameters, namely $\tilde{c_0}$, $\tilde{\rho_0}$ and $\tilde{\beta}$. Therefore, the approximate evolution equation in terms of the acoustic pressure can be written as:

$$\frac{\partial p}{\partial t} + \tilde{c_0}\frac{\partial p}{\partial x} = \frac{\tilde{\beta}}{2\tilde{\rho_0}\tilde{c_0}^2}\frac{\partial p^2}{\partial t}. \tag{2.36}$$

An analytic solution of this equation is also available through the Fubini's representation for the nth-harmonics of the fundamental wave of frequency ω and initial amplitude p_0 as

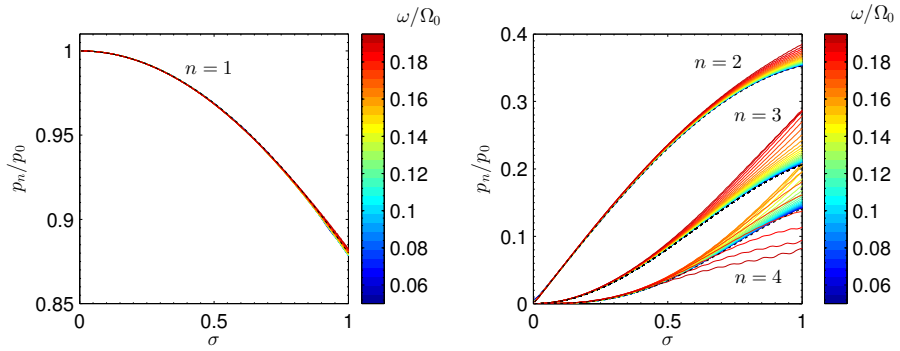


Figure 2.6: Harmonic generation in homogeneous-Fubini regime of the layered media

$$p(\sigma,\tau) = p_0 \sum_{n=1}^{\infty} \frac{2}{n\sigma} J_n(n\sigma)\sin(n\omega\tau), \tag{2.37}$$

where J_n is the Bessel function of order n, and $\sigma = x/x_s$ is the propagation coordinate, normalized to the shock formation distance:

$$x_s = \frac{1}{\tilde{\beta}\tilde{\varepsilon}k}, \tag{2.38}$$

with the effective match number $\tilde{\varepsilon} = u/\tilde{c_0}$ and the effective wavenumber $k = \omega/\tilde{c_0}$, that can be also found from Eq. (2.1). This celebrated solution is valid for $\sigma < 1$ (pre-shock region).

Simulations in this regime were carried out using a full-wave constitutive relations solver. Thus, we shall define the normalized frequency as $\Omega_0 = \pi\tilde{c_0}/a$ (located in the first band-gap). Therefore, the source frequency was set to $\omega = 0.1\Omega_0$.

Figure 2.6 shows the analytical and numerical solutions for the low frequency limit of the layered system, where an excellent agreement is obtained between Fubini and numerical solutions in the pre-shock region, $\sigma < 1$ and for low excitation frequencies. As commented above, when the fundamental frequency is increased the higher harmonics fall in dispersive region of the frequency bands, and thus its wave speed is reduced. In this situation, phase matching conditions are no longer fulfilled and therefore the energy transfer from fundamental to higher harmonics is modified. Thus, the Fubini solution can be only applied as an ideal solution for the low-frequency limit or as a good approximation for the first harmonics and for frequencies below $\omega \lesssim 0.1\Omega_0$.

However, it should be noted that for observing a shock wave, i. e. a discontinuous solution, all the spectral components must be phase matched, as occurs in

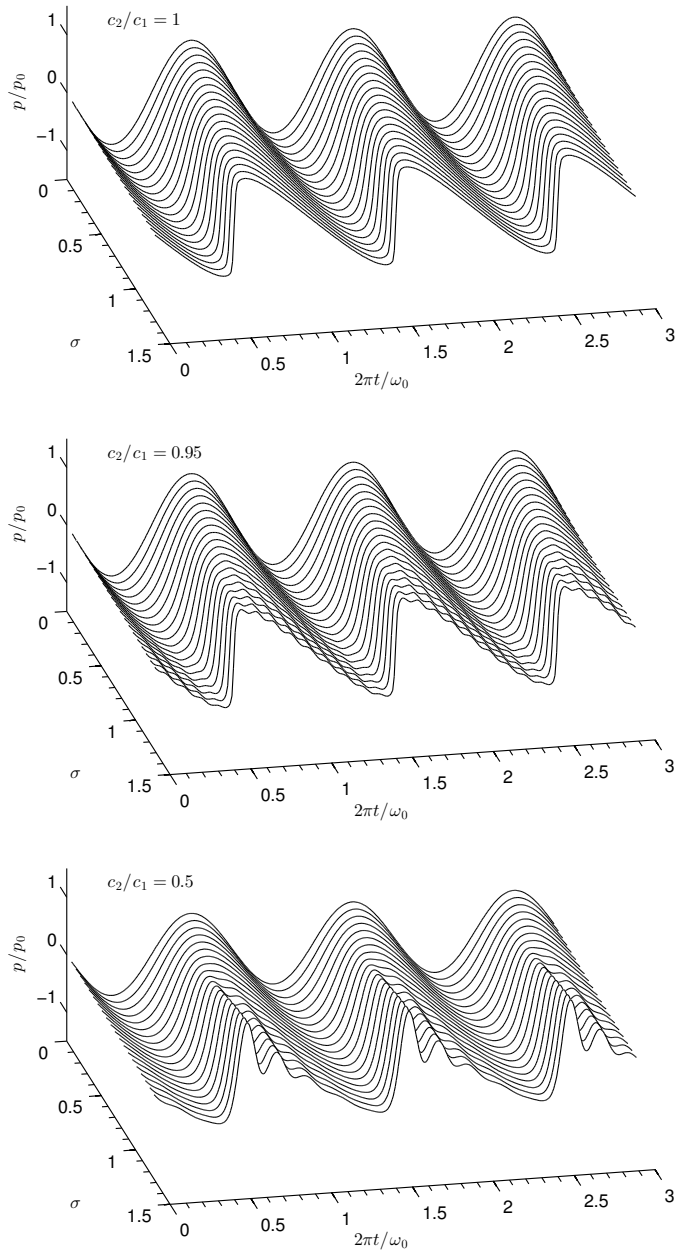


Figure 2.7: Waveform evolution beyond shock formation distance in layered media with parameters $\omega_0/\Omega_0 = 0.1$ and $c_2/c_1 = 1$ (top), $c_2/c_1 = 0.95$ (middle) and $c_2/c_1 = 0.5$ (bottom). Instead a discontinuity, pulsations around the sharp front are formed.

the nondispersive (homogeneous) media. Then, even for a low finite fundamental frequency, a small (but non negligible) dispersion will appear for the higher frequency components, and a phase mismatch is introduced on these high spectral components. The differences on phase speed on the different spectral components over a discontinuity impedes the formation of a stable traveling shock wave, as long sound speed dispersion spreads the high-frequency wave vectors that describe the discontinuous solution. Instead of a shock wave, pulsations or ripples are formed over the sharp nonlinear wavefront for $\sigma > 1$. This scenario reduces the validity of the homogeneous Eq. (2.36) to distances shorter than shock formation in lossless media, where the specific limit is dependent on the flatness of the dispersion relation near the band-gap, i.e. the layered media parameters: a, c_2/c_1, ρ_2/ρ_1 and $\alpha = a_1/a$.

Figure 2.7 shows the waveform evolution calculated at different distances in the shock-free region and also beyond shock formation distance for a homogeneous media ($c_2/c_1 = 1$) for a nearly-flat dispersion relation ($c_2/c_1 = 0.95$ and $\alpha = 0.5$) and for a more dispersive media ($c_2/c_1 = 0.5$, $d_2/d_1 = 0.5$). The above described effects are clearly visible: the waveform evolution follows the Fubini analytical solution for $\sigma < 1$ in both layered systems. However, for longer distances, pulsations around the discontinuity are formed due to different phase speed of the higher spectral components, spreading the sharp solution into a *solitonic* pulsations. In the absence of dissipation, these pulsations evolves in a train of weakly interacting solitons. Solitons in the layered media will be studied later on Sec. 2.6.

2.4.3 Dispersive regime

For frequencies above the (idealized) homogeneous-Fubini regime, finite (weak and strong) dispersion effects are observed. The dispersive effects of the layered system deeply affects harmonic generation processes.

As intense waves propagate through a quadratic nonlinear medium, their frequency component interact with each other and new frequencies arise at combination frequencies, including higher harmonics. The cumulative energy transfer from the interacting waves to the harmonics is dependent on the resonance conditions:

$$\omega_1 \pm \omega_2 = \omega_3 \ , \ \mathbf{k}_1 \pm \mathbf{k}_2 = \mathbf{k}_3. \tag{2.39}$$

Note these conditions express the laws of conservation of energy ($\hbar\omega$) and momentum ($\hbar\mathbf{k}$) in the quantum description for the disintegration and merging of quanta (Naugolnykh et al., 1998).

These conditions can be satisfied in a variety of situations. The most simple case is observed in nondispersive media and for collinear waves $k_i = \omega_i/c_0$. In this situation the resonance conditions are fulfilled all over the spectra and a large number of harmonics interacts synchronously: when there exist in the system a *free*

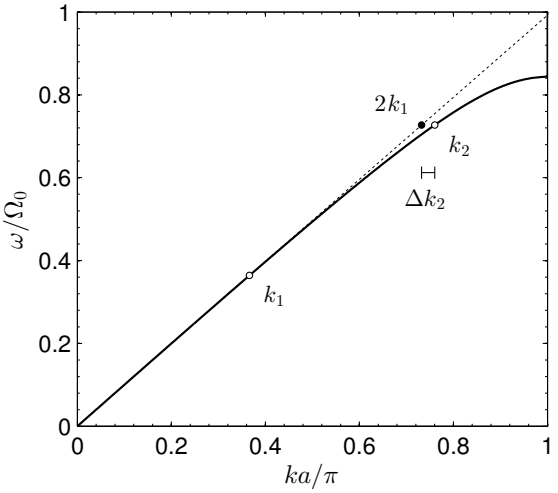


Figure 2.8: Scheme of the phase miss-matching situation. The fundamental wave vector k_1 at frequency ω generates a *forced* wave $2k_1$ at frequency 2ω. The *free* wave that the system allows to propagate is k_2, located in the dispersion relation curve. Due to dispersion, $k_2 \neq 2k_1$, thus there exist a phase mismatch, Δk_2 between both waves and the generation is therefore asynchronous.

wave with velocity $\omega_3/|\mathbf{k}_3|$ that matches the excited (*forced*) wave $\omega_1 \pm \omega_2/|\mathbf{k}_1 \pm \mathbf{k}_2|$, the *free* wave is excited in a resonant way. The resonant interaction leads therefore to synchronous, cumulative energy transfer from the initial wave to the secondary wave fields.

In the case of an initial monochromatic wave, the main wave generates its second harmonic. The resonant conditions Eq. (2.39) in this situation read

$$2\omega_1 = \omega_2 \ , \ 2\mathbf{k}_1 = \mathbf{k}_2, \tag{2.40}$$

that holds true for nondispersive collinear waves, leading to the simple relation $2\mathbf{k}(\omega_1) = \mathbf{k}(2\omega_1)$. However, in the case of dispersive media this condition is, in general, not fulfilled and the *forced* and *free* waves interact asynchronously. Figure 2.8 shows a scheme of this situation for a layered media with a fundamental wave in the first dispersion band.

In order to study asynchronous second harmonic generation processes, we recall here for the lossless second-order wave equation Eq. (2.31) for one-dimensional propagation

$$\frac{\partial^2 p}{\partial x^2} - \frac{1}{c_0^2}\frac{\partial^2 p}{\partial t^2} - \frac{1}{\rho_0}\frac{\partial \rho_0}{\partial x}\frac{\partial p}{\partial x} = -\frac{\beta}{\rho_0 c_0^4}\frac{\partial^2 p^2}{\partial t^2}. \tag{2.41}$$

This equation does not include dispersion by itself, dispersion arises from the solution of the linearized wave equation with the layered media boundary conditions, where the eigenvalue problem leads to the Rytov's dispersion relation Eq. (2.1).

In the following, we apply a perturbation method to obtain an approximate solution for the second harmonic field. We expand the pressure field as sum of contributions of different orders, as

$$p = p^{(1)} + \varepsilon p^{(2)} + \cdots , \tag{2.42}$$

where ε is the smallness perturbation parameter, which we identify with the acoustic Match number. Thus, $p^{(1)}$ is the first order (linear) solution of the problem and $p^{(2)}$ its the second order contribution. By substituting Eq. (2.42) in the second order wave Eq. (2.41), assuming constant density[1] and neglecting $\mathcal{O}(\varepsilon^3)$ terms we get the coupled set of equations

$$\frac{\partial^2 p^{(1)}}{\partial x^2} - \frac{1}{c_0^2}\frac{\partial^2 p^{(1)}}{\partial t^2} = 0 , \tag{2.43}$$

$$\frac{\partial^2 p^{(2)}}{\partial x^2} - \frac{1}{c_0^2}\frac{\partial^2 p^{(2)}}{\partial t^2} = -\frac{\beta}{\rho_0 c_0^4}\frac{\partial^2 p^{(1)2}}{\partial t^2}. \tag{2.44}$$

The first order Eq. (2.43) for a monochromatic plane wave of frequency ω has the trivial solution

$$p^{(1)} = p_0 \sin\left(\omega t - k_1 x\right) , \tag{2.45}$$

where $k_1 = k(\omega)$ is the wave vector associated with the primary frequency ω, and p_0 is the excitation pressure amplitude. Substitution of Eq. (2.45) into the right-hand side term of Eq. (2.44), using the trigonometric identity $\sin^2(\theta) = (1 - \cos(2\theta))/2$, an inhomogeneous equation for the second harmonic field is obtained:

$$\frac{\partial^2 p^{(2)}}{\partial x^2} - \frac{1}{c_0^2}\frac{\partial^2 p^{(2)}}{\partial t^2} = -\frac{4\beta\omega^2 p_0^2}{\rho_0 c_0^4}\sin\left(2\omega t - 2k_1 x\right). \tag{2.46}$$

The general solution of the this equation will be the sum of the solution of the homogeneous equation ($p_0 = 0$), and the particular solution of the inhomogeneous equation ($p_0 \neq 0$). Therefore the field for the second harmonic can be expressed as $p^{(2)} = p_h^{(2)} + p_f^{(2)}$, where the corresponding waves for this two solutions are the *free*, and *forced* waves respectively. Following Ref. Rudenko et al. (1977), we can obtain the homogeneous and particular solutions as:

[1] We neglect the ambient density variations for the sake of simplicity. Dispersion arise also for sound speed variations, that are assumed to be implicit in the boundary conditions.

$$p_h^{(2)} = p_h^{(2)}(x=0)\sin(2\omega_1 t - k_2 x), \tag{2.47}$$

$$p_f^{(2)} = \frac{A}{(k_2+2k_1)(k_2-2k_1)}\sin\left(2\omega_1 t - 2k_1 x\right), \tag{2.48}$$

where $k_2 = k(2\omega_1)$ is the wavenumber of the *free* wave at second harmonic frequency, and the constant $A = -4\beta\omega_1^2 p_0^2/\rho_0 c_0^4$. It is worth noting here that as long $2k_1 \neq k_2$, the *forced* and *free* waves in dispersive media have different phase speed, i. e. the *forced* and *free* waves are phase mismatched as can be seen in the argument of the sin function in Eq. (2.47-2.48). On the other hand, as long as there is not second harmonic at $x = 0$ (boundary condition), we must set

$$p_h^{(2)}(x=0) = -\frac{A}{(k_2+2k_1)(k_2-2k_1)}. \tag{2.49}$$

Therefore, combining Eqs. (2.47-2.49) the evolution of the second harmonic field can be expressed as

$$p^{(2)} = \frac{A}{k_2\Delta k}\sin\left(\frac{\Delta k}{2}x\right)\cos\left(2\omega_1 t - k_2' x\right), \tag{2.50}$$

where the effective wave number is $k_2' = (k_2 + 2k_1)/2 \approx k_2$ and the detuning parameter that describes the asynchronous second harmonic generation is defined as

$$\Delta k = |k_2 - 2k_1| = |k(2\omega) - 2k(\omega)|. \tag{2.51}$$

Equation (2.50) describes the well-known effect in second harmonic generation, that is the beatings in space of the second harmonic field when the resonant conditions are not fulfilled. Thus, as Δk increases, the beating spatial period and also its maximum amplitude decreases. The position of the maximum of the beating, also called the coherence length, can be related to the second-harmonic phase-mismatching frequency as

$$x_c = \frac{\pi}{\Delta k} = \frac{\pi}{|k(2\omega) - 2k(\omega)|}. \tag{2.52}$$

This length corresponds to the half of the spatial period of the beating, where the maximum of the field is located. It can be expressed also for other higher harmonics simply as $x_c(n) = \pi/\Delta k_n = \pi/|k(n\omega) - nk(\omega)|$.

In the limiting case of $\Delta k \to 0$, the second harmonic field is generated synchronous and accumulates with distance, so linear growth is predicted. In this

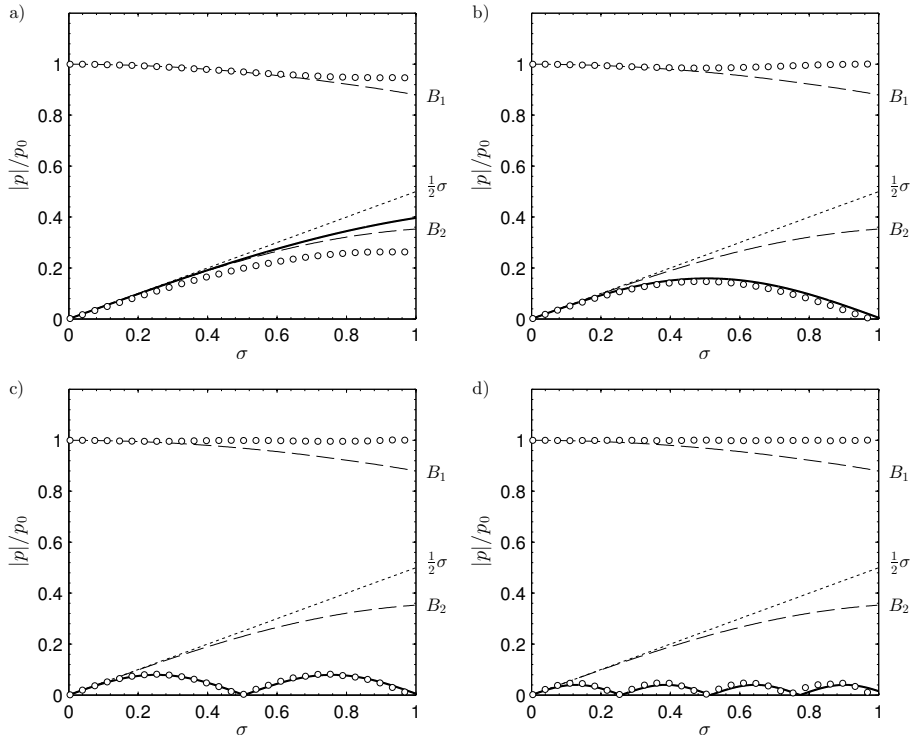


Figure 2.9: Second harmonic evolution for $x_c/x_s = [1, 1/2, 1/4, 1/8]$ obtained using Eq. (2.50) (continuous line), numerically (white circles), nondispersive linear law of growing (dotted line) and Bessel-Fubini nondispersive solution (dashed).

case, phase matching conditions are fulfilled and the *free* wave is excited synchronous to the *forced wave*. Note here that in the derivation of Eq. (2.50) only second order processes are taken into account and therefore, only second harmonic is predicted. This leads to overestimate the second harmonic field: as long no energy is transferred to third harmonic, second harmonic predicted by Eq. (2.50) in the absence of dispersion grows indefinitely. The validity of this model can be explored expanding the Bessel functions of Fubini series near the source. A simple comparison between the full Fubini solution and linear second harmonic growth gives a reasonable approximation for distances $\sigma < 0.5$ or for second harmonic field values of $p(2\omega) < p_0/4$.

Figure 2.9 shows four different simulations in the dispersive regime of the layered media where the wave amplitude and frequency has been selected to match $x_c/x_s = [1, 1/2, 1/4, 1/8]$. The higher beating spatial period waves corresponds to lower frequencies. The analytical solution for the second harmonic matches the full-wave numerical solution. However, differences can be observed in the second harmonic amplitude estimation for $x_c/x_s = 1$ (left plot in Fig. (2.9)). This

overestimation by the analytical solution can be related to the absence of energy transfer to higher harmonics, that is not considered by the perturbation solution but is included in the simulation. Therefore, this model is specially suitable in situations where the third harmonic does not grow cumulative with distance. In the lossless layered media, this situations include frequencies that leads to very high-third harmonic detuning and also when the third harmonic falls in band gap.

2.4.4 Second harmonic in band gap

Waves with frequencies falling into the band-gap of the dispersion relation are evanescent due the non negligible imaginary part of its complex wave number. Thus, its amplitude decays exponentially with distance. When the second harmonic frequency falls into the band-gap, a characteristic effect, studied also in other nonlinear lattices (Sánchez-Morcillo et al., 2013) can be observed: its amplitude reaches a constant value. Figure 2.10 present an example of this case for four

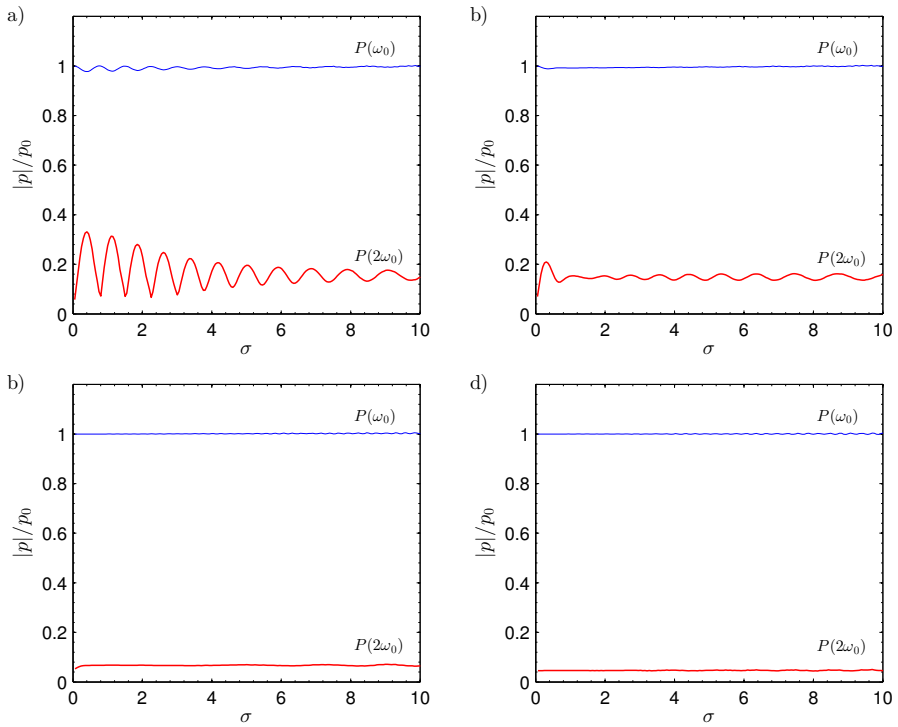


Figure 2.10: Evolution of the second harmonic field propagating in bang-gap for second harmonic frequencies (a) just above band-gap $2\omega_0 = 0.84\Omega_0$, (b) $2\omega_0 = 0.85\Omega_0$, (c) in the middle of the bandgap $2\omega_0 = \Omega_0$ and (d) $2\omega_0 = 1.05\Omega_0$ at the maximum of the imaginary part for the first band gap. All results for a layered system of $\alpha = 1/2$ and $c_1/c_2 = 1/2$.

different frequencies, where can be observed that the constant value of the second harmonic field depends on the imaginary part of the wave vector.

This effect can be understood in terms of the *free* and *forced* waves. If the second harmonic is evanescent (as follows from the dispersion relation), the wave will not accumulate with distance. But the fundamental wave is still "pumping" energy to the second harmonic field at every point in space. Thus, the second harmonic field is generated locally and remains trapped inside the layered media. It reaches a constant level that depends on three main factors. In first place, the "pumping" rate, characterized by the fundamental wave amplitude and medium nonlinearity, or more strictly the ratio between the layer thickness and the shock distance d/x_s. Secondly, it also strongly depends on the magnitude of the imaginary part of the complex wave number, i.e. the ratio between its characteristic exponential decay length and the shock distance in a layer. The characteristic decay length of the evanescent propagation is always shorter when the second harmonic is in the middle of the band-gap, leading to less second harmonic field in this frequency region, as can be seen in Fig. 2.10 (c-d). Finally, it depends also on the detuning of real part of the wave number, where for the first band-gap is minimum at the center. The first factor can be isolated and studied separately. However, the two last factors are linked through the specific dispersion relation of the medium.

Figure 2.11 shows the detuning of the second harmonic and the imaginary part as a function of the frequency for a medium with $\alpha = 1/2$ and $c_1/c_2 = 1/2$, showing that at the middle of the band-gap these two factors have opposite effects: detuning is minimized when evanescence decay is maximized and vice versa. However, the magnitude of the effects can be very different. As the rate of the second harmonic generation (see the initial slope in Fig. 2.9) is independent on the detuning, and the evanescence implies that the wave decays after few layers, there not exist a practical

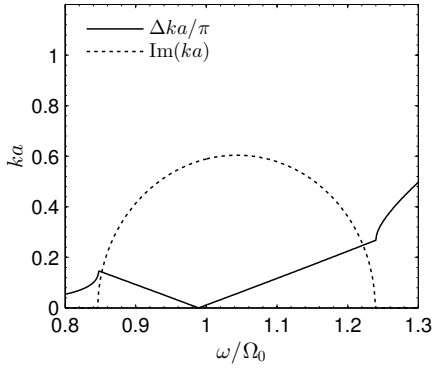


Figure 2.11: Detuning of the second harmonic (continuous line) and imaginary part (dotted line) in function of the normalized frequency.

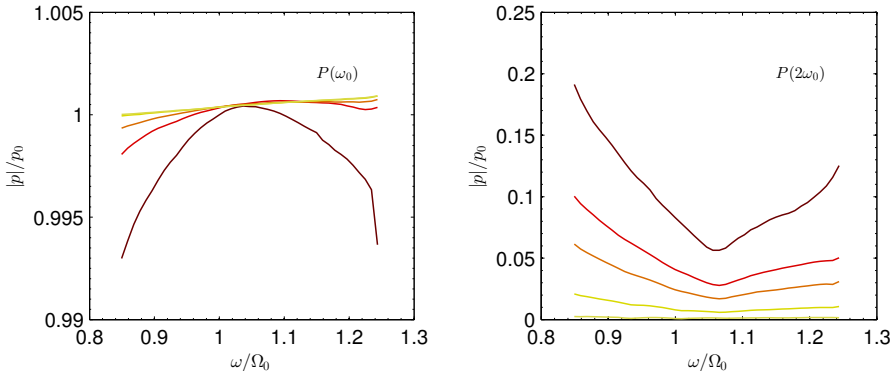


Figure 2.12: (left) Amplitude of the constant field value for fundamental (dashed) and (right) its second harmonic field (continuous line) for amplitudes matching $a/x_s = 0.08, 0.04, 0.02, 0.001$

compensation of the effects at the center of the band-gap. However, the situation is different for frequencies around the limits of the band-gap, where the coherence length is of the order of the exponential decay characteristic length. Thus, for frequencies just above bad-gap and for amplitudes with shock distance comparable to the evanescent characteristic decay length, the beatings can be also observed, as shown in Fig. 2.10 (a). Then, if frequency is increased the characteristic decay length becomes shorter than the shock wave distance and beatings cannot be observed, leading to to the characteristic constant second harmonic field shown in Fig. 2.10 (c-d).

Figure 2.12 (right) shows the second harmonic amplitude (of the constant field) in function of the frequency for different amplitudes matching a/x_s =0.08, 0.04, 0.02, 0.001, where it is clearly visible that the minimum field value is obtained at the frequency of the maximum imaginary part of the complex wave number. On the other hand, as more energy is transferred to second harmonic the fundamental amplitude decays in an inverse way of its second harmonic field, as shows in Figure 2.12 (left).

2.4.5 Fundamental harmonic in band gap

When the fundamental frequency of the wave lies within the band-gap, small amplitude waves propagates evanescently. Essentially, the same applies to finite amplitude harmonic waves. In general, if the shock distance is large compared to the exponential characteristic length of the evanescent wave, the nonlinear effects have no time to accumulate and harmonic amplitude is negligible. Since the characteristic exponential decay is about few lattice sites, this means that the initial amplitudes necessary to achieve nonlinear effects in this configuration are much higher than those in the preceding sections. Figure 2.13 shows the evolution of the

first and second harmonics for a fundamental frequency falling in the middle of the bad-gap, $2\omega_0 = 1\Omega_0$, and with a frequency just above but into the band-gap, $\omega_0 = 0.87\Omega_0$ for a layered media of $\alpha = 1/2$ and $c_1/c_2 = 1/2$. In the first case, the imaginary part of the wave vector is remarkable high and the waves decay fast after few lattice units. Due to this fast decay, the second harmonic interacts over a short distance with the first, and its amplitude is very limited. After few lattice units, fundamental wave can be treated as a small-amplitude evanescent-wave. The second harmonic, that also falls in bandgap (but in the second band) also decays exponentially.

On the other hand, if the fundamental frequency is set just above the band-gap, where the imaginary part of the wave-vector is smaller, the amplitude of the fundamental wave decays more slowly, penetrating deeper into the material. The interaction region with the second harmonic is larger, and nonlinear effects resultv in a more efficient generation of the second harmonic. Furthermore, as long the different (higher order) bandgaps in the layered media can have different band-width, in this configuration at $\omega_0 = 0.87\Omega_0$ second harmonic does not fall inside a bandgap. Therefore, the generated second harmonic wave at the beginning of the lattice propagates through the medium essentially without amplitude change. Due to the evanescence of the fundamental wave, there is only *forced* wave at the beginning of the medium. Therefore, although in this configuration waves are phase mismatched, beatings are not present: only the *free* wave propagates through the medium.

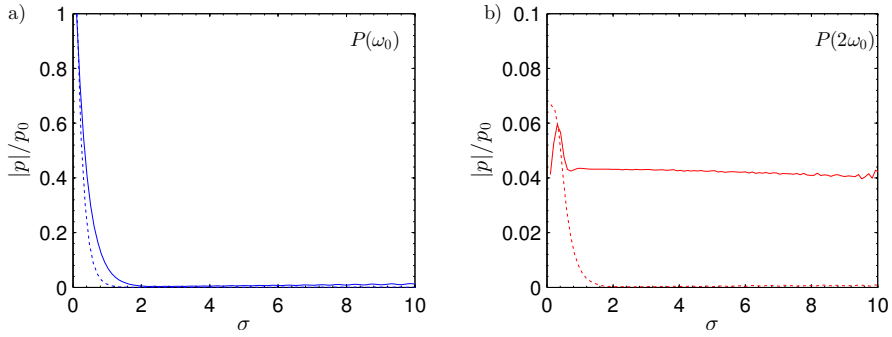


Figure 2.13: (a) Evolution of the fundamental harmonic wave field with its fundamental frequency falling just above into band-gap, $\omega_0 = 0.87\Omega_0$, (continuous line), and in the middle of the bad-gap, $2\omega_0 = 1\Omega_0$ (dotted line). (b) Corresponding second harmonic field, where for $\omega_0 = 1\Omega_0$ (dotted line) second harmonic frequency falls in the 2nd band band-gap while for $\omega_0 = 0.87\Omega_0$, (continuous line) lies into a propagating band.

2.5 Nonlinear acoustic field management

2.5.1 Tuning nonlinearity with dispersion

In the preceding sections we have explored the fundamental behavior of nonlinear waves generated inside layered media. However, the layered medium parameters can be tuned to provide specific conditions. These conditions are, among others, looking for detuning or coherence at specific frequencies and using the evanescent propagation in the bad-gap for another specific frequency.

The material parameters can be tuned to get coherence at one frequency of interest, e.g. at one of the harmonics of the fundamental wave, or to get detuning or evanescent propagation at other specific harmonics. Using these mechanisms the layered system provides a control of the nonlinear process inside the medium. Thus, the layered media can be tuned in order to obtain specific balance of the harmonic amplitude or specific nonlinear waveforms.

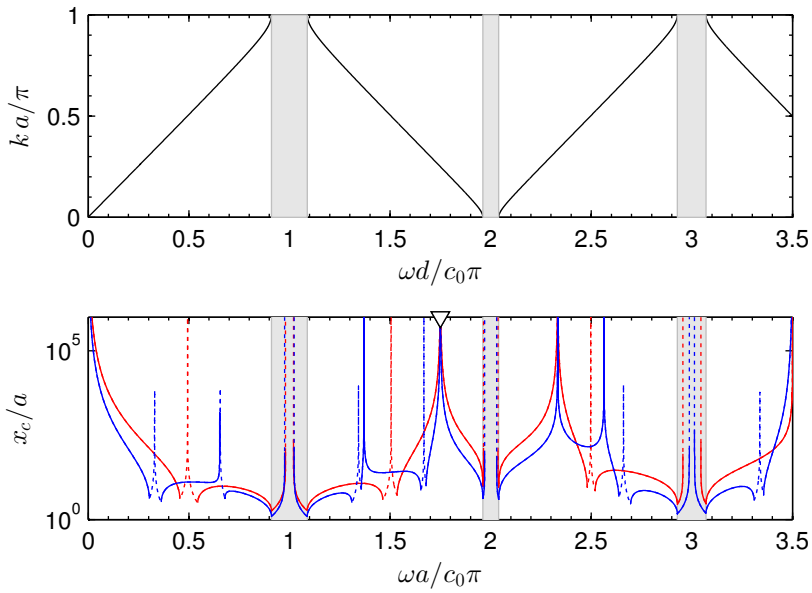


Figure 2.14: (Top) dispersion relation for a layered media of $c_1/c_2 = 1.33$ and $\alpha = 1/2$. (Bottom) coherence length for second (red) and third (blue) harmonic in function of the fundamental frequency. Phase matched frequencies are those with $x_c \to \infty$, while asynchronous generation is predicted for $x_c \to 0$. Frequencies at which the fundamental frequency is in band-gap are is marked in gray regions, while band-gap regions for second and third harmonic are marked in dashed lines.

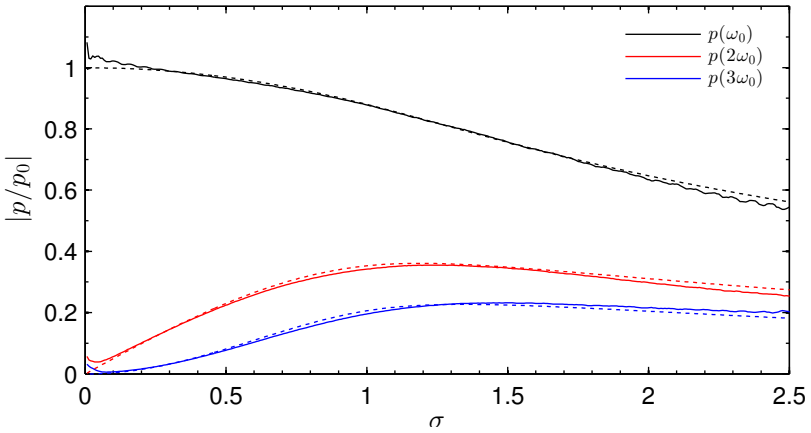


Figure 2.15: Harmonic distribution for the frequency $\omega_0 = 1.75/\Omega$. Coherence is recovered for at least the lowest spectral components. Blackstock solution (dotted lines).

In the design of a system for this purpose, the coherence length is a useful control parameter. Thus, Fig. 2.14 (top) shows an example of the dispersion relation with parameters $c_1/c_2 = 1.333$ and $a = 1/2$. Then, in Fig. 2.14 (bottom) the coherence length for the second and third harmonic is shown. The propagating bands are marked with continuous lines while the band-gap frequencies are marked in dotted lines. Thus, the abscissa axes marks the frequency of the fundamental wave. It can be observed that there exist singular frequencies, e.g. frequencies where all the harmonics are phase matched, $x_c \to \infty$. In Fig. 2.14 it happens for $\omega_0 = (0, 1.75, 2.333, ...)/\Omega$. On the other hand, there also exist frequencies at which there exist coherence for the second but a non-negligible detuning is observed for the third. Opposite effect can be observed, where coherence is achieved for the third harmonic but second harmonic presents strong dispersion. Finally, other interest regions are those where second harmonic component is almost phase matched and for the same frequency third harmonic falls into a band-gap.[2]

Thus, the analytic Eq. (2.1) provides an excellent framework to tune-up the layered parameters to obtain the desired balance between detuning, evanescent propagation, synchronous generation and, at the same time, it allows to find those conditions for a specific phase/group speed.

We start studying the harmonic distribution for an initial monochromatic wave of $\omega_0 = 1.75/\Omega$, corresponding to the triangle marked in Fig. 2.14 (bottom). Figure 2.15 shows the harmonic distribution, where, as expected, synchronous cumulative harmonic generation inside the dispersive media is recovered. The harmonic evolution in the second band follows again the Bessel-Fubini-Blackstock harmonic

[2]This singular situations can be also obtained with no difficulty for physical values of sound speed and other layer proportions. We use here normalized values for the sake of simplicity.

distribution for the lower spectral components. However some remark must be underlined. First, there exist some detuning for the high frequency components that avoids the formation of shock waves for $\sigma > 1$. Figure 2.16 shows the waveforms measured at $\sigma = (0.5, 1, \pi/2, 2)$. It can be observed that, although second and third harmonics are phase matched a shock is not produced. Due to finite detuning of the higher harmonic components, oscillations instead of a shock wave profile appears for $\sigma > 1$, as those presented in the low frequency limit in Sec. 2.4.2.

It is worth noting here that coherence is achieved in theoretically lossless media for all spectral components. However, losses can modify the dispersion relation specially for frequencies near the band-gap. Thus, in practical cases, where losses exist and typically increases quadratically with frequency, the dispersion relation will be modified specially at frequencies of the higher spectral components. In the presented cases, due to the introduction of some amount of artificial attenuation necessary for nonlinear numerical stability and convergence, it is observed how appears a finite detuning for high spectral components, causing the characteristic dispersive oscillations. On the other hand, the finite difference method used always introduces some amount of artificial dispersion that modify the dispersion relations. However, the oscillatory solutions, e.g. Fig. 2.16, are therefore not caused directly by numerical artifacts. They are not present in homogeneous simulations. Note the grid used is 300 elements per wavelength and the artificial attenuation was only 10^{-3} P/s, ten times greater than the water viscosity. The effect of computational restrictions is to slightly modify the dispersion relations for higher harmonics causing finite detuning. We expect those effects to be present in real materials, and therefore, limit the ability of recovering perfect coherence for all spectral components and create shock waves[3].

Other interest feature is that in these conditions phase speed at the fundamental and at higher harmonic frequencies always match $c_p(n\omega) = \bar{c}_0$. In contrast, in this situation the group velocity does not match necessary the low frequency sound speed. In this case was close, with a value of $c_g = 0.97\bar{c}_0$.

Other situations can be explored by changing the layered parameters. Figure 2.17 (top)shows the dispersion relation for $c_1/c_2 = 2$ and $\alpha = 0.1$. It is shown in Fig. 2.17 (bottom) that coherence is achieved, at least for the lowest components, for $\omega/\Omega = 1.22$. In this case, the phase speed matches $c_p(n\omega_0) = \bar{c}_0$, but the group velocity is reduced to $c_g(\omega_0) = 0.830$. Figure 2.18 shows the evolution of the fundamental and its first two harmonics. A remarkable effect that can be observed here is the appearance of high-amplitude oscillatory fields due to the strong impedance contrast between layers, actually nonlinear Bloch waves. In these reduced group velocity conditions, the analytical solution for homogeneous media (dashed lines) does not match the numerical results. However, no beating are produced and the shape of harmonic growing is essentially the same. It can be seen that the rate of second and third harmonic growth is increased. The distance at

[3]Other interesting topic, not studied here, is to find conditions for recovering coherence in media with attenuation by tuning its lossy dispersion relations

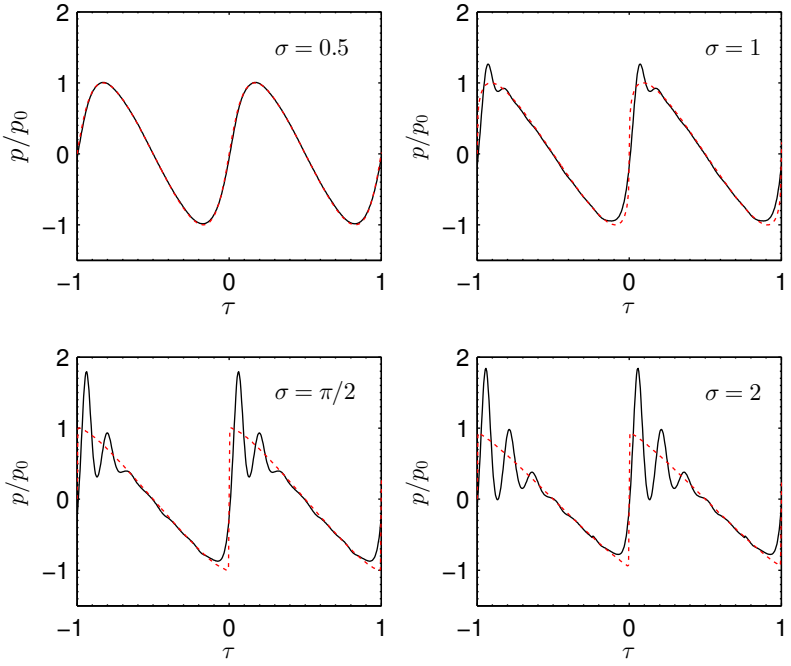


Figure 2.16: (continuous lines) Waveforms at different distances ($\sigma = 0.5, 1, \pi/2, 2$) for $\omega_0 = 1.75/\Omega$ where a coherence is recovered for the lowest harmonics. Blackstock analytic solution (red dotted lines).

which the maximum second harmonic field is produced is located at $\sigma \approx 1.2$ in the homogeneous media while in the numerical simulations appears at $\sigma = 0.7$. Same scaling is observed for the rate of harmonic generation, where in the homogeneous media (near the source) second harmonic grows at a rate $p_0\sigma/2$ Pa/σ, and in the numerical simulations the rate of growing was $0.86p_0/\sigma$ Pa/σ. The whole effect is that the effective nonlinearity of the system in these conditions is increased. For the present case, a factor of increased nonlinearity can be obtained by fitting the analytical solution to the numerical results, letting as the free variable an effective parameter o nonlinearity, namely $\bar{\beta}$. Thus, for the presented results, a factor of $\bar{\beta} = 1.72$ is estimated. A new solution using this effective parameter is shown in Fig. 2.17 (bottom) in thick lines. It can be observed how the fitted solution agrees the slow-group speed for distances up to the effective shock distance (0.58σ in the figure). The observed effect of retaining coherence and reduce group velocity is to increased the effective nonlinearity of the media together with the apparition of high-amplitude nonlinear Bloch waves.

In the following subsections, we propose and analyze different interest layered

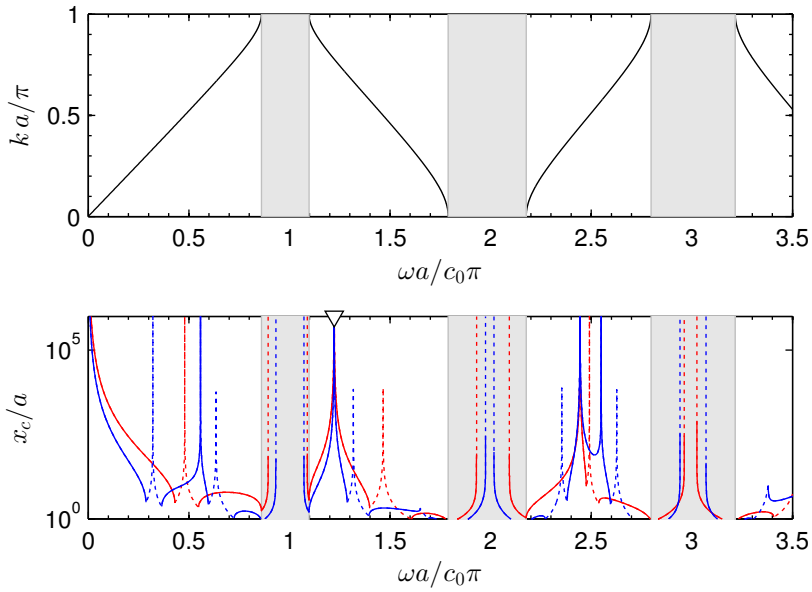


Figure 2.17: (Top) dispersion relation for a layered media of $c_1/c_2 = 2$ and $\alpha = 0.1$. (Bottom) coherence length for second (red) and third (blue) harmonic in function of the fundamental frequency. Frequencies at which the fundamental frequency is in band-gap are is marked in gray regions, while band-gap regions for second and third harmonic are marked in dashed lines.

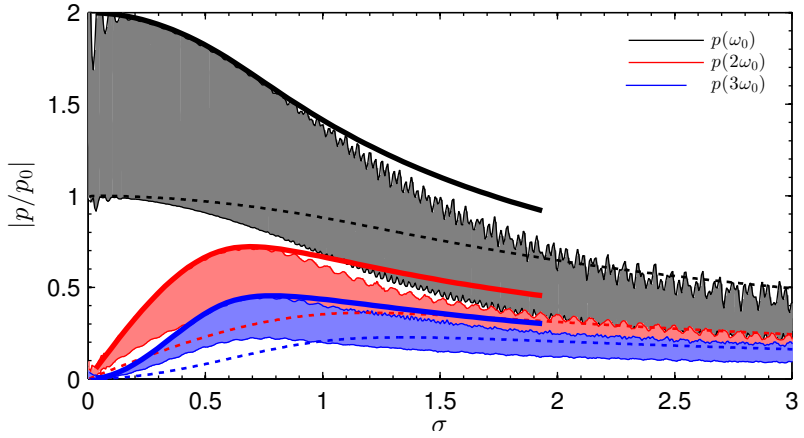


Figure 2.18: Harmonic distribution for the frequency $\omega_0 = 1.22/\Omega$. Blackstock solution (dotted lines).

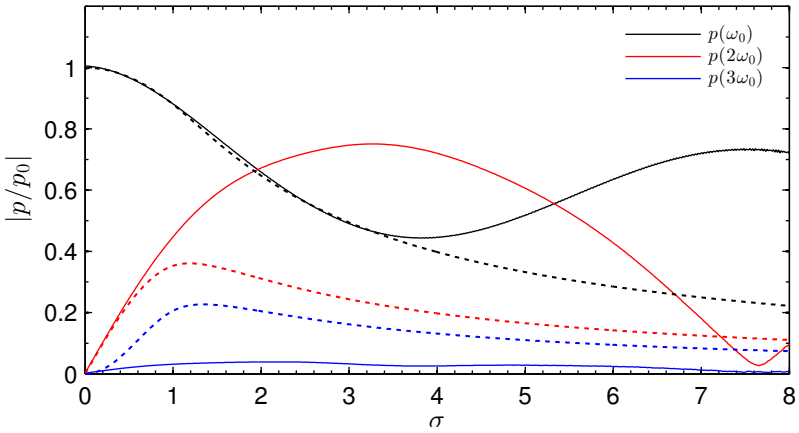


Figure 2.19: Harmonic distribution for $\omega_0 = 1.668/\Omega$ where a coherence is achieved for second harmonic while the frequency of the third harmonic falls into the bad-gap.

media designs with specific balance between between detuning, evanescent propagation and synchronous generation.

2.5.2 Increasing second harmonic generation

One can expect that second harmonic generation is maximized in homogeneous nondispersive media. However, in nondispersive media coherence is achieved not only at second harmonic frequency, but also in the higher spectral components. As a result, energy is transferred from second harmonic field to higher spectral components and therefore second harmonic field does not grow indefinitely. Moreover, shock waves are formed and nonlinear absorption reduces wave intensity for $\sigma > \pi/2$ even in lossless media (Hamilton et al., 1998a).

The controlled dispersion of the layered system can modify this situation by including dispersion that alters the higher harmonic cascade processes while maintaining coherence for second harmonic. Figure 2.14 shows an example of a dispersion relation where for $\omega_0 = 1.668/\Omega$ it can be observed that there exist a reasonable coherence for the second harmonic ($x_c/a \approx 1000$ lattice units), while the third harmonic falls in a band-gap. Figure 2.19 shows the harmonic distribution in this situation. Here, energy is transferred to second harmonic field that grows almost linearly for $\sigma < 2$. On the other hand, the energy transferred from second to third harmonic is not cumulative and its amplitude does not grow with distance. Third harmonic experiment evanescent propagation due to the imaginary part of the complex wave-vector at this frequency. A constant field, as studied in Sec. 2.4.4, is obtained for the third harmonic.

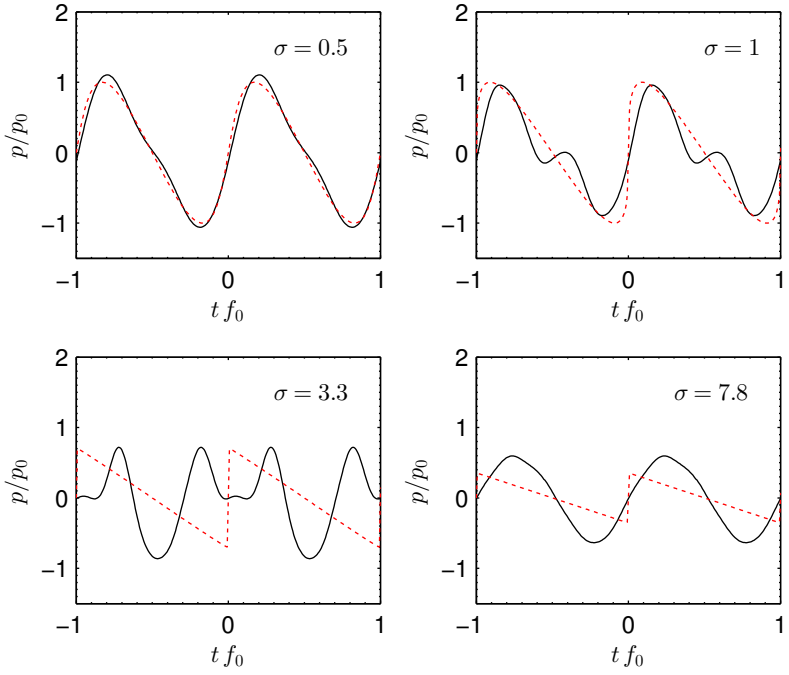


Figure 2.20: (continuous lines) Waveforms at different distances for $\omega_0 = 1.668/\Omega$. At $\sigma = 3.3$ second harmonic generation field is maximize and can be seen the period doubling in the waveform. Then, at $\sigma = 7.8$ due to second harmonic detuning nearly sinusoidal wave is recovered. Blackstock analytic solution (red dotted lines).

The total amount of the second harmonic amplitude in nondispersive media is $p_2|_{\max} \approx 0.36 p_0$, while in the example of Fig. 2.19 a maximum second harmonic amplitude of $p_2|_{\max} \approx 0.75 p_0$ is predicted. As can be shown the decreasing of the first harmonic follows the analytic nondispersive Blackstock solution for $\sigma \lessapprox 3$. Thus, in this regime all the energy of the first harmonic is being transferred to the second harmonic field. However, due to finite detuning of the second harmonic a long spatial beating is produced, with period 8σ, and energy is returned back to the first harmonic component.

It is worth noting here that at distance $\sigma \approx 3$ sawtooth profile is observed in nondispersive media. In contrast, only second and first harmonic have remarkable amplitude into the layered media. Waveforms are shown in Fig. 2.20. Near the source, where the amplitude of higher harmonics in not relevant the nondispersive waveform (in red dotted) is well approximated by the fundamental and its second harmonic of the layered medium. However, due to the evanescent propagation of the third harmonic for longer distances the nonlinear solution of the layered medium is mainly composed by the fundamental and its second harmonic. The

maximum second harmonic in this configuration is observed at $\sigma = 3.3$, where it can be appreciated in the waveforms of Fig. 2.20 the period doubling. Moreover, due to finite detuning of the second harmonic the process is not cumulative for all distances and at $\sigma = 7.8$ the energy is restored in the first harmonic again and a sinusoidal wave is obtained[4]. An analogous effect has been also studied (Naugolnykh et al., 1998) where instead of dispersion, selective absorption at specific frequencies is used to modify and enhance harmonic generation.

2.5.3 Increasing third harmonic generation

In the first band ($\omega < \Omega_0$), coherence is always lower for the third harmonic than for the second. However, in the superior bands the layered medium parameters can be tuned to obtain higher coherence for the third than for the second harmonic. Essentially we follow same ideas on the preceding section but for the third harmonic. In this case, the lattice is designed forcing the second harmonic to fall in bandgap. A the same time, perfect coherence can be found for the third harmonic at $\omega = 0.529\Omega_0$. This situation is illustrated on Fig. 2.21. In this case, the dispersion relation was obtained for a layered medium with parameters $\alpha = 0.3$ and $c_2/c_1 = 1/3$.

In this situation, as Fig.2.22 shows, second harmonic field present a constant value of about $0.04p_0$. As discussed in Sec.2.4.4, this constant field does not grow with distance and is related to the evanescent solution of the *free* wave and the local nonlinear "pumping". On the other hand, due to the coherence of the third harmonic, all the energy transferred form second to third is accumulated with distance. Therefore, near the source the rate of energy transfer from second to third harmonic is constant. Thus, third harmonic start to grow almost linearly with distance, opposite to quadratically in homogeneous media.

Also it can be seen in the simulations how fourth and fifth harmonics grow (red dotted and blue dotted lines in Fig. 2.22). In this case only fifth harmonic have remarkable amplitude, growing near the source almost quadratically with distance. Therefore, the entire system behaves as an artificially cubic-like nonlinear medium formed by quadratic nonlinear layers.

The corresponding waveforms measured at $\sigma = (0.5, 2, 8, 12)$ are shown in Fig. 2.23. For $\sigma = 0.5$ and 2, it can be observed how the wave steepens with the characteristic shape of cubic nonlinearity. No shock waves are formed as long strong dispersion is present for high frequency harmonics. However, it is worth noting here a remarkable fact: it steepens in the positive time axis direction (to

[4]Note all the energy is not restored to first harmonic in Fig. 2.19 at $\sigma = 7.8$, leading to a sinusoidal wave of different amplitude as can be observed in Fig. 2.20. The energy loss is mainly due to the artificial (numerical) viscosity necessary to nonlinear convergence(Hamilton et al., 1998a). For these simulations the total distance is 1200 lattice sites and therefore the effects of attenuation are not negligible. However, the main nonlinear effects related to strong lattice dispersion still appreciated.

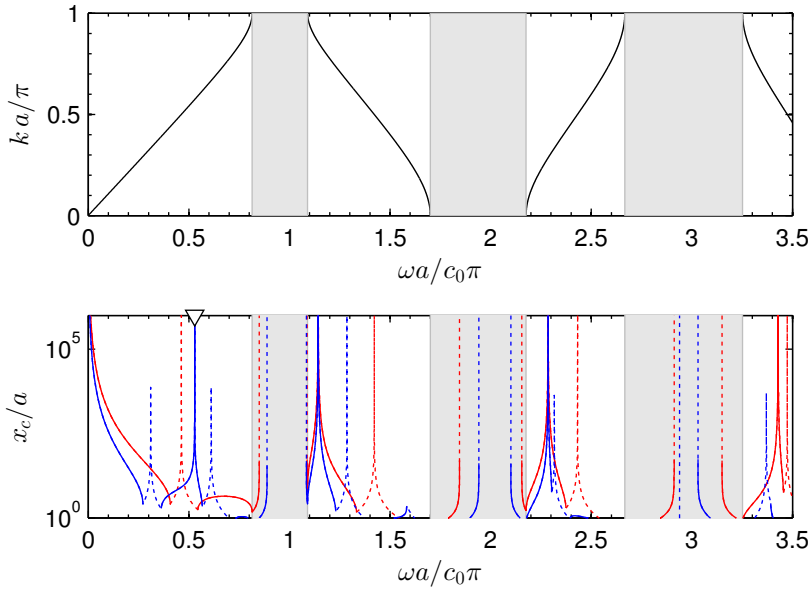


Figure 2.21: Harmonic distribution for $\omega_0 = 1.668/\Omega$ where a coherence is achieved for second harmonic while the frequency of the third harmonic falls into the bad-gap.

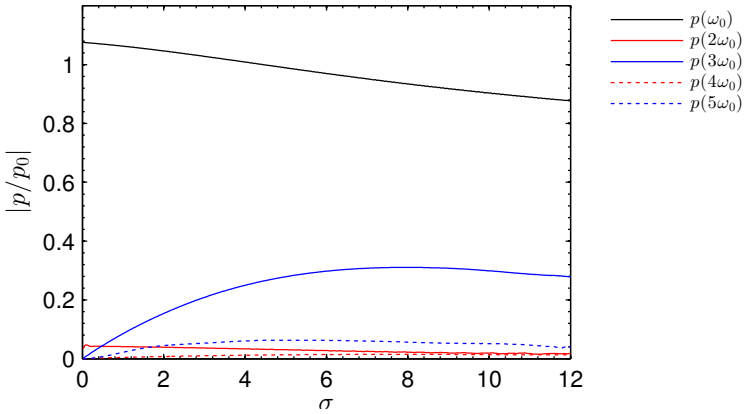


Figure 2.22: Harmonic distribution for $\omega_0 = 1.668/\Omega$ where a coherence is achieved for second harmonic while the frequency of the third harmonic falls into the bad-gap.

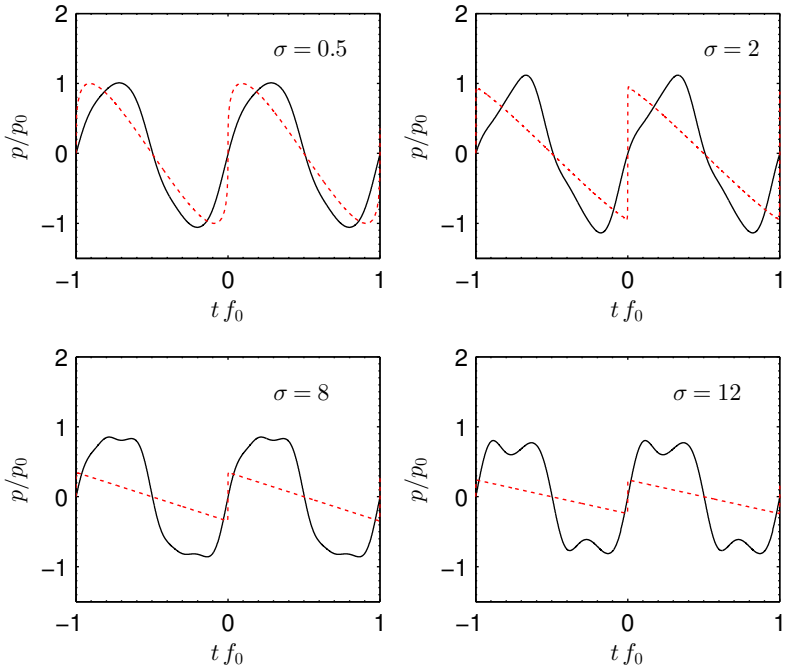


Figure 2.23: (continuous lines) Waveforms at different distances for $\omega_0 = 1.668/\Omega$. At $\sigma = 3.3$ second harmonic generation field is maximize and can be seen the period doubling in the waveform. Then, at $\sigma = 7.8$ due to second harmonic detuning nearly sinusoidal wave is recovered. Blackstock analytic solution (red dotted lines).

the right in the figure), opposite than the quadratic nonlinearity plotted in red dotted as a reference. This effect, i.e. the steepening on the opposite side of the propagation direction, is characteristic of materials with negative parameter of nonlinearity. Therefore, the effective nonlinear behavior observed by the simulations in this conditions can be described as negative-cubic-like nonlinearity.

2.5.4 Acoustic *Fluorescence* in chirped layered media

Another interesting configurations can be achieved by adiabatically changing the lattice period, $a = a(\mathbf{x})$, of the layered medium, namely chirped layered media. Analogues to these configurations, chirped periodic media has been studied in linear regime in optics (Cheng et al., 2014) or in acoustics using arrays of distributed cylindrical scatterers (Romero-García et al., 2013). Using these chirped configurations band-gap can be placed at different locations for different frequencies. Here, we design a system with increasing lattice period, where the band-gap for

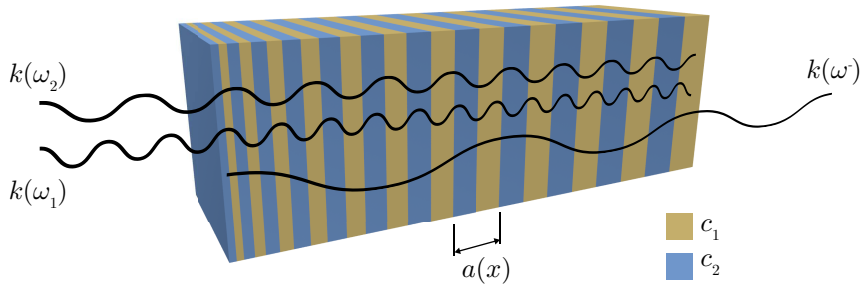


Figure 2.24: Scheme of the acoustic "fluorescence" effect. The chirped system is radiated with two waves of slightly different fundamental frequencies ω_1 and ω_2. Harmonics are generated at combination frequencies inside the medium and at the end of the system the period is tuned to achieve a band-gap at fundamental frequency. Thus, only the low-frequency difference-component is transmitted.

the fundamental component of two nearly similar frequency waves is located at the end of the chirped layered medium. Thus, as sketched in Fig. 2.24, two harmonic waves with close frequencies are injected at the beginning of the lattice. In this region, the lattice period is designed small enough to achieve good coherence so harmonics at combination frequencies can be generated progressively through the layered system. Then, at the end of the lattice the period is decreased in such a way that it correspond to a forbidden band for the fundamental component.

In this case, the frequency of the waves was selected to be $f_1 = f_0$ and $f_2 = f_0 + f_0/3$. Figure 2.25 (top) shows the bandgap location in the lattice, that is located at $x = 0$ until $x = 200a$. Then, the rest of the domain is homogeneous. Although it is calculated for infinitely period media, we assume that the band gap exist for the adiabatic chirped lattice. Figure 2.25 (bottom) shows the harmonic evolution for this configuration where it can be seen how harmonics at combination frequencies are generated at the beginning of the lattice. The bandgaps of layered medium act as spatial filtering for the fundamental components that are reflected back around $x/a = 100$, leading to an enhancement of the field discussed in (Romero-García et al., 2013). This enhancement is clearly visible in Fig.2.25 (bottom). Furthermore, not only fundamental frequency is filtered. As long the bandgap central frequency change with distance, the superior bandgaps cover the entire frequency range, reflecting back higher harmonics.

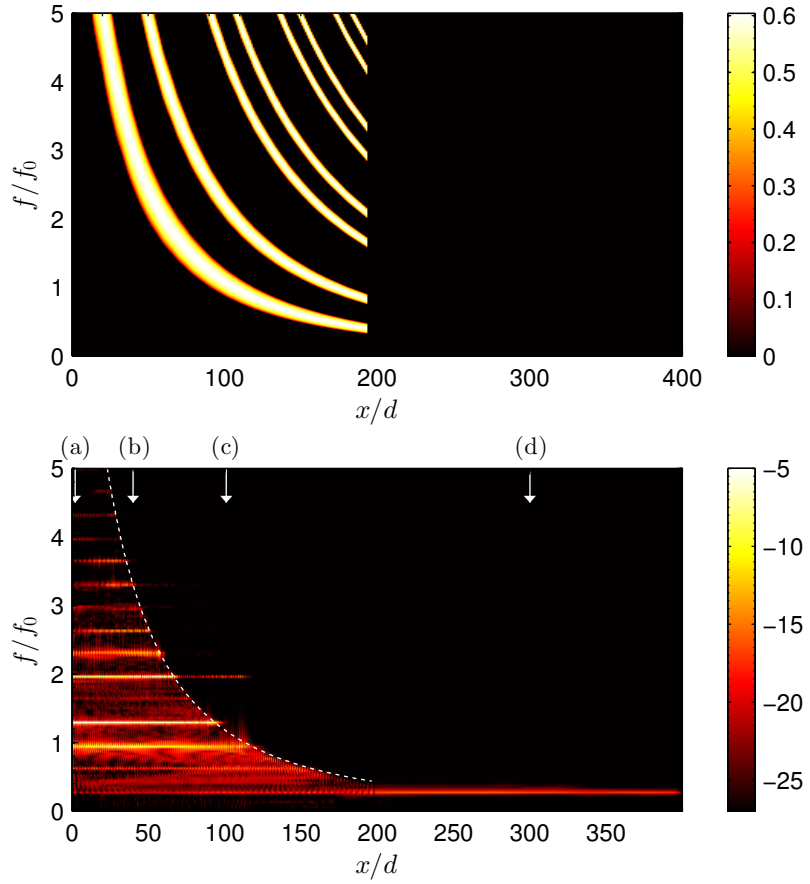


Figure 2.25: (top) Bandgap distribution in function of space. The chirped lattice ranges from $x = 0$ to $x/a = 200$, (middle) Spectrum-spatial distribution, (bottom) harmonic distribution for fundamental waves, its second harmonics and the difference component.

Therefore, only the difference frequency wave can be transmitted trough the medium. The final effect is that in transmission an effective demodulation is achieved: an amplitude modulated wave is injected, see Fig. 2.26 (a), the difference frequency is nonlinearly generated among other combination frequencies Fig. 2.26 (b-c), and the system output is only the low frequency component.

The whole effect presents some analogy with fluorescence, where electrons re-emit a photon when relaxing to a lower quantum state after being exited with some electromagnetic wave. The emitted light has, in most cases, a longer wavelength and lower energy, than the absorbed radiation. Obviously, this analogy is not formal and only conceptual.

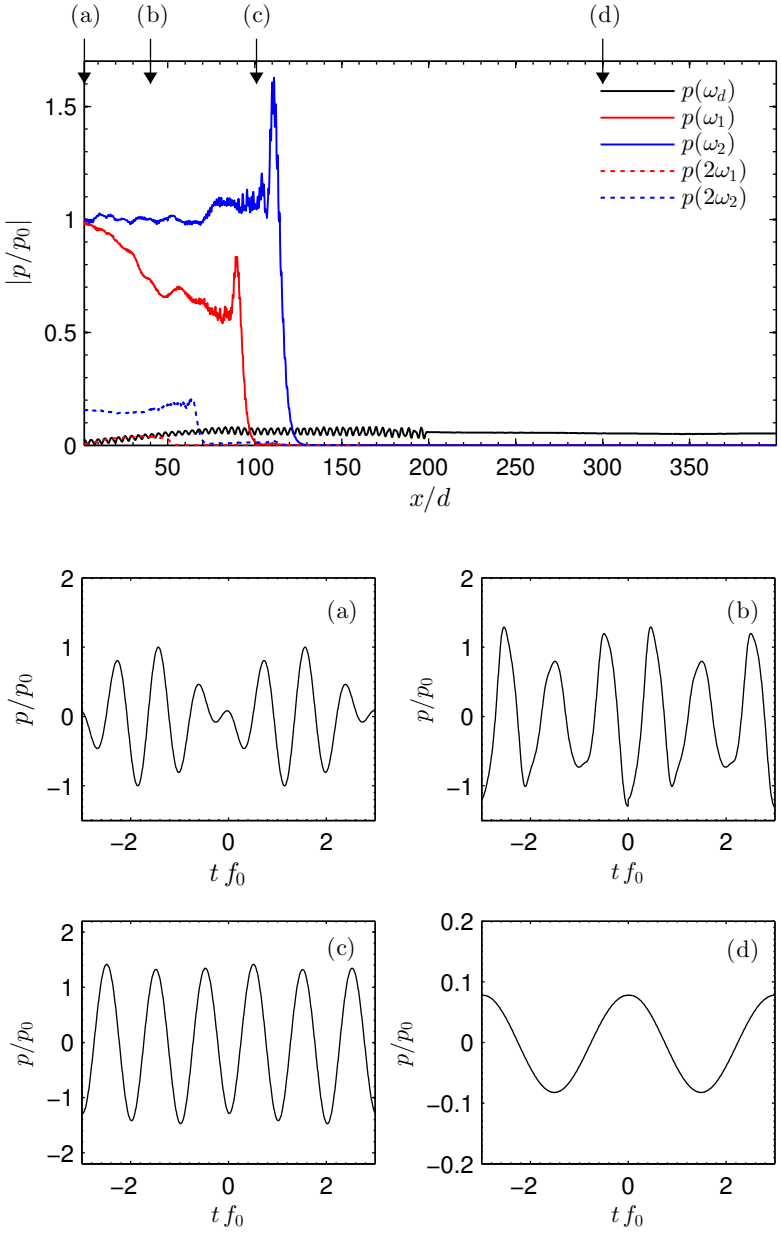


Figure 2.26: (Top) Harmonic distribution in the chirped layered media where the acoustic "fluorescence" is observed. The self-demodulation of the two collinear modes is achieved inside the nonlinear media, while the band-gap at the end of the chirped layered media limits the transmission of the high frequency components. Therefore, only the self-demodulated component is transmitted. (Bottom) Corresponding waveforms observed at locations (a-d).

2.5.5 Frequency Conversion Mirror in chirped layered media

We propose a setup of the chirped layered media in which the bandgap is located for the frequency of the second harmonic at the end of the structure. Actually, the structure is equivalent to the preceding subsection, but a monochromatic fundamental wave is selected here at frequency ω^{-}. The fundamental wave is therefore a propagating mode over all the structure. On the other hand, its second harmonic only can propagate trough the beginning part of the structure. At the end of the layered media, its corresponding wavevector presents an imaginary part and the propagation is evanescent. Therefore, it is reflected back to the source. From the point of view of the source, the whole process can be treated as a nonlinear mirror: the incident wave is reflected with doubled frequency.

In order to visually illustrate the process, simulations were carried out using a k-space method over a 2D domain. The incident wave was generated by a Gaussian beam at frequency ω, steered 10^{o} from the axis of the structure, see Fig. 2.27. It is worth noting here that the theoretical dispersion relation is one-dimensional and for non-normal incidence angles it will change. However, for illustrate the processes and for the selected incident angles is enough.

Figure 2.28 shows the first and second harmonic field, with the structure in the middle and the source below. It can be seen that when the intense wave impact on the layered, its first harmonic is slightly refracted due to different phase speed in the outside media and in the layered structure. Then, it shows very high transmission out of the structure. Only spurious reflection of the first harmonic is observed due to the impedance mismatching at the boundaries of the structure: in both limits of the crystal (top and bottom) reflection can be observed. On the other hand, the second harmonic is generated at the beginning of the propagation and inside the structure. The transmission of second harmonic is negligible. It can be seen how its amplitude becomes negligible in the bandgap area marked by

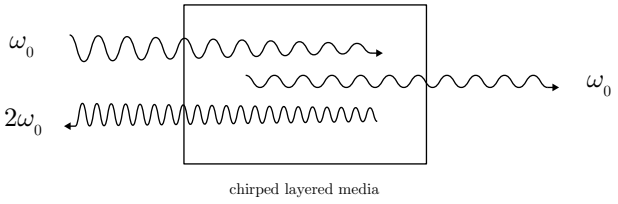


Figure 2.27: Scheme of the *frequency conversion mirror* effect. A wave with fundamental frequency ω_0 enters in the chirped system. Second harmonic is generated inside the medium and at the end of the system the period is tuned to achieve a band-gap at second harmonic frequency. Thus, second harmonic is reflected while fundamental field is transmitted.

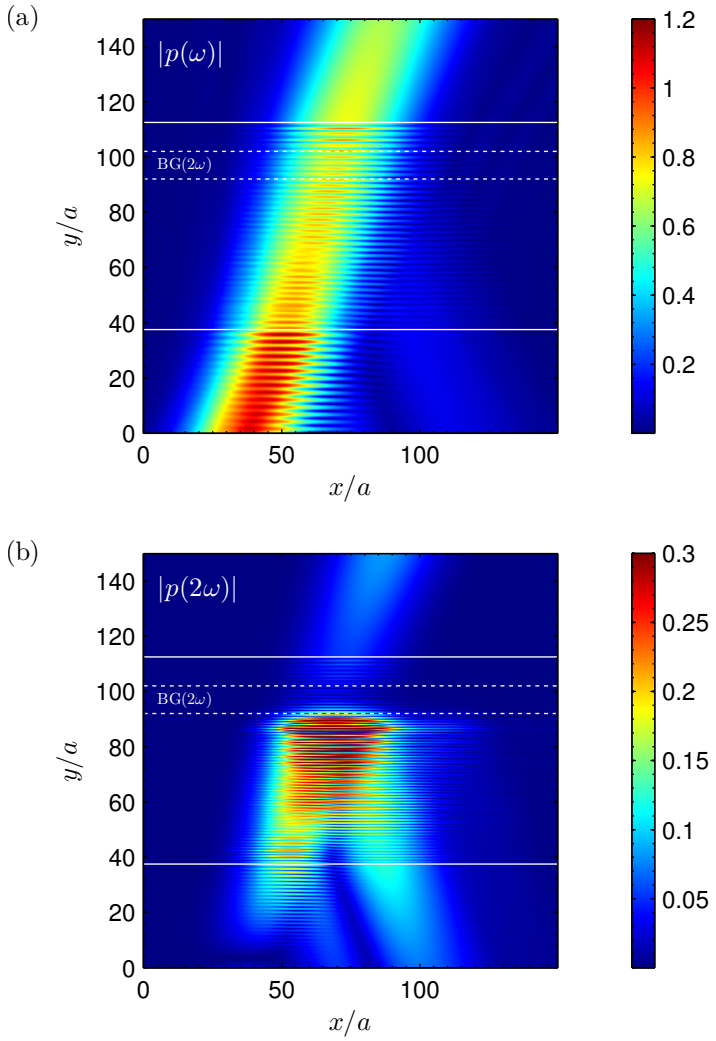


Figure 2.28: Field distribution for (a) first harmonic and (b) second harmonic field in the frequency conversion mirror configuration. The chirped layered media extends between white lines. White dotted lines marks the extension of the bandgap for the second harmonic.

the dotted lines. After the end of the gap, first harmonic start again generate harmonics by cascade processes, and second harmonic field increases, but the second harmonic generated at the beginning is not transmitted. The energy that is not transmitted is reflected back, as can be seen in Fig. 2.28 (b). In addition, reflection at the bottom boundary can be also observed due to impedance mismatching.

The effects of the present configuration can be enhanced by using very high

nonlinear material in the construction of the layered media than in the surrounding fluid. Thus, for instance using layers of bubbly fluids and solid plates with micro cracks the nonlinear generation of second harmonic can be located only inside the layered structure and if the bandgap is properly designed at the end of the lattice the transmission of second harmonic will be negligible. On the other hand, controlling the length of the crystal and the steering of the beam the reflection of the second harmonic can be uncoupled totally from the reflections of the first harmonic field. Another improvements include focalization of the reflected harmonics as achieved in optics for linear waves (Cheng et al., 2014).

2.5.6 β-Modulated media

Finally, instead of modulate the sound speed and density of the layers, the nonlinear parameter of the media can be also modulated. Thus, it is interesting to take into account that there exist some materials, most of them solid, that exhibit negative nonlinearity. These materials are well-known and also common, e.g. some glasses as Pyrex or fused silica (Hamilton et al., 1998a). The nonlinear processes in negative nonlinear parameter media are not completely different from the positive ones. The nonlinear parameter shows the dependence of sound speed on pressure. Thus, the difference between positive and negative nonlinear media is that in negative media the rarefaction cycles of the wave travels faster than the compression cycles. Thus, wave profile distortion, as Fig. 2.29 sketches, is simply inverted.

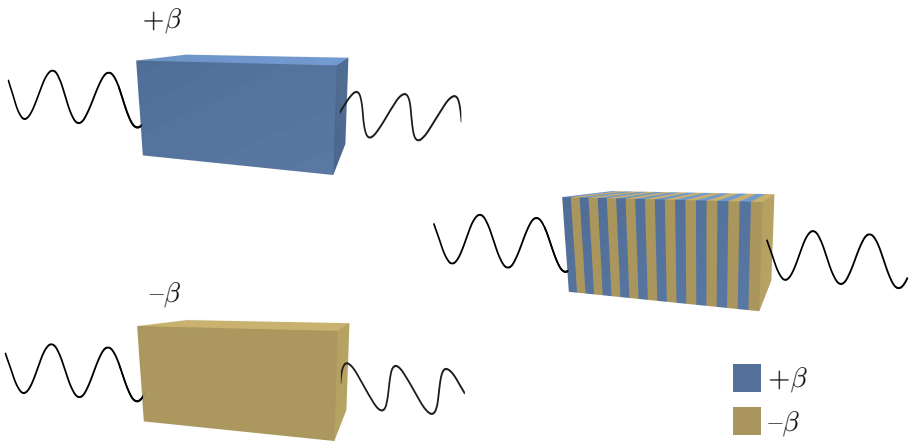


Figure 2.29: Scheme of the β-modulated acoustic layered media. (top-left) The nonlinear distortion in an homogeneous layer with $+\beta$ leads to steepening in the $+z$ direction, while for $-\beta$ the steepening is produced in the opposite direction. Therefore, alternating thin layers of positive and negative nonlinearity the steepening distortion can be mitigated.

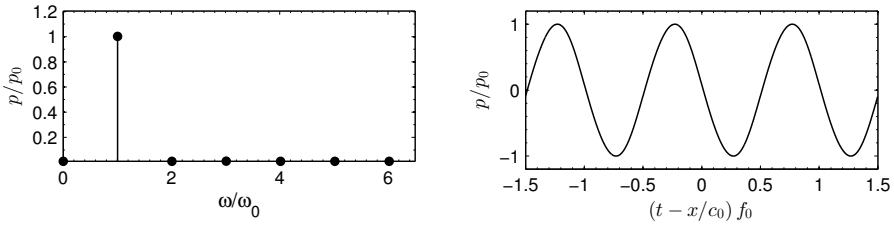


Figure 2.30: (Left) Spectrum obtained at $\sigma = 1$ for a wave traveling a the β-modulated material. (Right) Corresponding waveform.

Then, we propose a configuration where thin layers of two materials with inverted nonlinear parameter are alternated. The idea is that the distortion during propagation in one layer is compensated by the distortion in the following and thus, a extremely linear material can be generated for supporting very intense waves at distance much longer than the shock formation distance. For the sake of simplify, the density and sound speed will be maintained equal in both media. The layer thickness was set to $a = 0.1\lambda$ and the nonlinear parameters as $\beta_1 = -\beta_2 = 5$, of the order of the common materials.

Extremely linear media

Figure 2.30 shows the waveform and its spectrum recorded at the shock distance. It can be observed the absence of nonlinear distortion. due to the negligible energy transference to higher harmonics the fundamental component retains its initial amplitude. The evolution of the spectral components versus distance is shown in Fig. 2.31. It can be observed that the monochromatic wave can travel at the shock distance without experiment distortion.

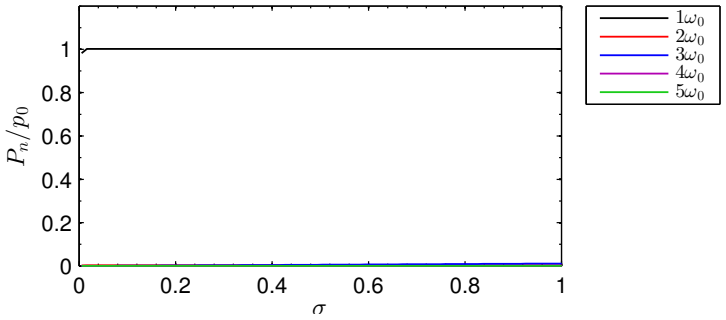


Figure 2.31: Harmonic evolution in the β-modulated material. Up to the shock wave distance almost all the energy remains in the fundamental harmonic and the harmonic amplitude for the higher spectral components is negligible.

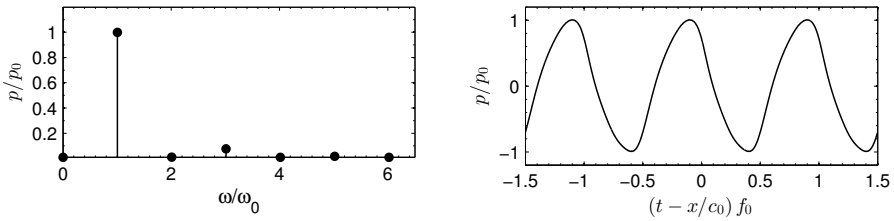


Figure 2.32: (Left) Spectrum obtained at $\sigma = 10$ for a wave traveling a the β-modulated material. (Right) Corresponding waveform.

Cubic nonlinear composite media

However, an interesting effect is also observed. If the propagation is long enough, some harmonics of the fundamental frequency appears, but only the odd harmonics are generated. Thus, response of the media appears to be effectively equivalent to a cubic media. An explanation of this phenomena can be obtained for nondispersive propagation. The asymptotic expressions for the amplitude of the harmonics near the source can be obtained by expanding the Bessel-Fubini Eq (2.37). The expansion leads to the expressions for the second and third harmonics:

$$p_2(x,\tau) = \frac{\beta p_0^2 \omega}{2\rho_0 c_0^3} x \sin 2\omega\tau, \tag{2.53}$$

$$p_3(x,\tau) = \frac{3\beta^2 p_0^3 \omega^2}{8\rho_0^2 c_0^5} x^2 \sin 3\omega\tau. \tag{2.54}$$

It can be seen that the second harmonic grows linearly with the distance and it is proportional to the nonlinear parameter β. On the other hand, the third harmonic depends quadratically on both variables. Then, if a wave travels trough a layer of the proposed structure with $\beta_1 = +\beta$, its second harmonic will increase

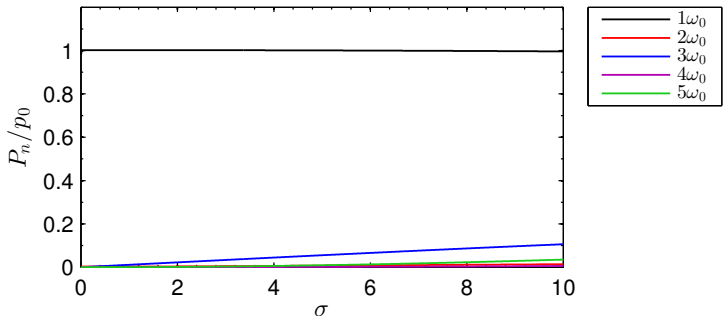


Figure 2.33: Harmonic evolution in the β-modulated material, where it can be seen the generation of odd harmonics.

linearly and the third, almost absent, will do quadratically. When the wave crosses the next layer with inverted nonlinearity $\beta_2 = -\beta$, Eq. 2.53 contributes creating the same amount of second harmonic than in the preceding layer but inverted due to the $-\beta$ coefficient, i.e. with opposite phase. Therefore, second harmonic at the end of the second layer vanishes. This process holds for thin layers were the asymptotic expressions can be applied. However, the generation of third harmonic depends on β^2, so there does not exist cancellation between layers and the generation is cumulative with distance. Third harmonic is generated by cascade processes and needs second harmonic field. Due to second harmonic is generated and compensated periodically, the evolution of the third does not grows quadratically with distance and its rate of the generation is very slow.

Figure 2.33 presents the evolution of the spectral components for distances up to $x = 10x_s$. It can be observed that the odd harmonics are generated and the even ones vanishes. On the other hand, the generated third harmonic shows an almost linear dependence with propagation distance, where the fifth harmonics grows at a quadratic rate. Figure 2.32 shows a waveform recorded at $\sigma = 10$, where the characteristic shape of cubic nonlinearity can be observed, see e.g. (Jacob et al., 2007). On the right plot, its spectrum revels an almost negligible contribution of the even harmonics.

The configuration proposed, opens a way to obtain cubic nonlinearity for the longitudinal waves from a layered distribution of quadratic nonlinear materials. Therefore, such structure can be designed also using solid composites in the micro scale to obtain new ways of management of acoustic waves as low distortion waveguides for intense perturbations where the acoustical saturation distance can be extended. In the more general case including dispersion, the system offers the possibility of designing new tunable nonlinear materials where phase velocity and effective nonlinearity can be modified to achieve exotic configurations, while the structure is made from common material composites.

2.6 Dispersion managed acoustic solitons

One of the most widely studied phenomena in most nonlinear and strongly dispersive media is the existence of solitons. Solitons are nonlinear localized perturbations that propagate without changing its shape, emerging from the interaction of nonlinearity and dispersion. The first observation of the solitary waves was in 1834 by John Scott Russell at the Union Canal in Scotland, who called them *Waves of Translation*. In its experiments Russel described the main properties of these shallow-water waves (Russell, 1844). Starting from the theoretical works of Boussinesq and Rayleigh (Boussinesq, 1871; Boussinesq, 1877; Rayleigh, 1876), these waves could not been completely explained by the existent theory of water waves until 1895 when the Diederik Korteweg and Gustav de Vries derived a simple partial differential equation for shallow-water waves (Kordeweg et al., 1895).

Their model, now known as the KdV equation, is completely integrable and provides exact solutions as solitons and cnoidal waves. However, it was not widely studied until 1965 with the advent of the computational physics when Zabusky and Kruskal found that the KdV model arises as the continuum limit of the FPU nonlinear lattice (Zabusky et al., 1965).

From these seminal works, solitary-wave solutions have been observed and deeply studied in most physical systems that can support nonlinear and dispersive waves: electromagnetism and nonlinear optics; hydrodynamics; acoustics, elastodynamics and granular media; phononics and nonlinear molecular dynamics, DNA dynamics, Bose-Einstein condensates, plasmas and so on. The solutions presented Chapter 1, in the limit of weak dispersion and weak nonlinearity, can also be described by the KdV equation. The acoustic layered media is not an exception.

Solitons have been studied by Yong et al. (2003) in layered acoustic media and in also in media with alternated solid and fluid layers (Fainstein et al., 2013; Huynh et al., 2015). Here, we extend the analysis using numerical techniques in the limits of strong nonlinearity and strong dispersion, i.e. from the long and slow solitons to sharp and intense acoustic solitary-waves.

2.6.1 KdV solitons

The Korteweg-de-Vries (KdV) equation arises as the continuum limit of the FPU quadratic nonlinear lattice (Zabusky et al., 1965). Thus, in the low frequency limit both models can be described by the same dispersion relation. Consider the dispersion relation of a mono-atomic lattice as

$$\omega^2 = \omega_M^2 \sin\left(\frac{ka}{2}\right)^2, \tag{2.55}$$

where c_0 is the small amplitude sound speed and a the oscillator separation, and the upper cut frequency is $\omega_M = 2c_0/a$. We can expand in Taylor series this lattice dispersion relation around $k = 0$, retaining up to cubic terms leads to the KdV dispersion relation:

$$\omega(k) = c_0 k - bk^3, \tag{2.56}$$

with

$$b = \frac{1}{24} c_0 a^2 \tag{2.57}$$

as the dispersion parameter of the low frequency limit for longitudinal vibrations in any mono-atomic lattice. Figure 2.34 shows the normalized dispersion relation for the lattice and its KdV low frequency approximation, where it can be appreciated

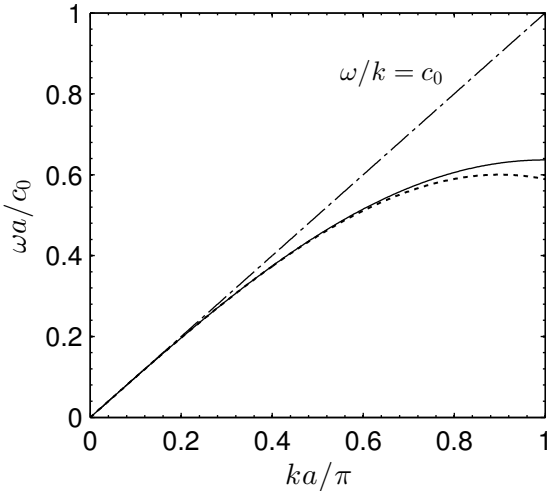


Figure 2.34: Dispersion relation for the mono-atomic lattice (continuous) and its KdV low frequency regime (dotted). Nondispersive slope is plotted in dashed-dotted line for comparison.

that both models fit very well for long wavelengths, but also for remarkable high wavenumbers. Relative difference is below 1% for wavenumbers below $kd/\pi < 0.64$. However, the group velocity in this equivalent KdV is lower then in the full lattice, and it decreases faster with frequency.

Seen that similarity between band structures, and given the fact of the same quadratic nonlinearity is present in the KdV model and the FPU lattice, it is not surprising that similar solutions can be obtained in both systems, at least in the low frequency regime. The solutions explored in the Coulomb chain presented in Chapter 1 can be obtained also by the KdV equation provided that the kinks are far of the ultra–discrete regime, e.g. for energies below 0.5 eV.

Furthermore, homogenization techniques can applied to the layered media (Santosa et al., 1991), where, despite the complexity of the superior bands, the dispersion relation in the first band present the same shape under some assumptions than the FPU lattice. Therefore, a Taylor series expansion of Eq. (2.1) in powers of ω around $\omega = 0$, collecting terms up to second order, leads to

$$\omega^2 \approx (1 - \cos(ka)) \frac{2c_1^2 c_2^2}{a\,(a_2 c_1^2 + a_1 c_2^2)}\,. \tag{2.58}$$

Then, we expand again in Taylor series in powers of k around $k = 0$, and collecting terms up to third order we get

$$\omega \approx \sqrt{\frac{ac_1^2c_2^2}{a_2c_1^2+a_1c_2^2}}\,k - \frac{a^2}{24}\sqrt{\frac{ac_1^2c_2^2}{a_2c_1^2+a_1c_2^2}}k^3\,, \tag{2.59}$$

that can be expressed in the compact KdV form

$$\omega(k) = c_0k - bk^3\,, \tag{2.60}$$

with the parameters

$$c_0 = \sqrt{\frac{ac_1^2c_2^2}{a_2c_1^2+a_1c_2^2}} \tag{2.61}$$

$$b = \frac{a^2}{24}c_0\,. \tag{2.62}$$

Note the dispersion parameter is exactly the same that obtained for the FPU mono-atomic lattice.

However, this result only states that both models are similar around $k = 0$, but there can exist remarkable differences between the layered system and its equivalent KdV model for short waves when $ka \to 1$. Figure 2.35 shows the full dispersion relation for three different α ratios and its asymptotic solution for the low frequency regime by Eq. (2.60). It is clearly seen that good agreement between the mono-atomic lattice and its KdV expansion is only achieved in the case of $\alpha = 0.9$ and $c_2/c_1 = 0.1$. For the other cases ($\alpha = 0.1$ and $\alpha = 0.5$), the first propagation band becomes flatten, the frequency at which the band-gap start becomes higher and therefore the band-gap stretches. In the limit of Eq.(2.1) for $\alpha \to 1$ and $c_2/c_1 \to 0$, the first band of the layered matches exactly the mono-atomic chain dispersion relation Eq. (2.55), while the second band does not start in a finite frequency, i.e. there does not exist superior bands. This limit shows that the first band most dispersive shape for the layered medium is the dispersion relation Eq. (2.55). This situation corresponds to the case of a homogeneous media with infinitesimal-sized soft inclusions. Note that the inclusions impedance contrast must be large and also that the sound speed of the inclusions must be is low than the host media. A good analogy of this situation, for small amplitude waves[5], is a one dimensional version of a liquid with period inclusions of gas bubbles. Also note in one dimensional system a rigid inclusion ($c_2/c_1 = 0$) implies zero transmission and therefore no wave inside the structure, increasing c_2/c_1 to low but physical values mean strong dispersion.

On the other hand, the effect of the layered medium dispersion is to *flatten* the slope of the first propagation band for high spatial frequencies, from the critical

[5]Soft inclusion typically shows large compressibility values and for finite amplitude waves the inclusions, in this case bubbles, are large compressed. Therefore, large strains are produced and the material response is described not only by its compressibility, but a large fraction of its local nonlinearity.

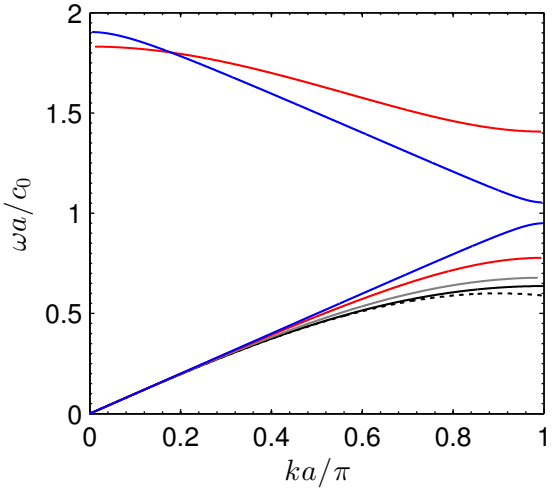


Figure 2.35: Dispersion relation for the layered media using $c_2/c_1 = 0.1$ and $\alpha = 0.1$ (blue), $\alpha = 0.5$ (red) and $\alpha = 0.9$ (gray), mono-atomic lattice (black) and the KdV homogeneous limit (dotted line). It can be observed that the layered linear dispersion relation converges to the lattice dispersion for small inclusion of low sound speed.

case of the mono-atomic chain dispersion (gray line in Fig. 2.35), to situations in which infinitesimal bandgap are created and the group speed is c_0 for all the frequencies (blue line in Fig. 2.35).

As can be seen, the layered media dispersion can modify its shape in a large amount of different configurations. Soliton shape, width and amplitude will depend in those parameters.

Let us recall here the second order lossless-Westervelt Eq. (2.31), assuming ρ_0 does not change with space and for plane waves travelling in the x direction

$$\frac{\partial^2 p}{\partial t^2} - c_0^2 \frac{\partial^2 p}{\partial x^2} - \frac{\beta}{\rho_0 c_0^2} \frac{\partial^2 p^2}{\partial t^2} = 0. \tag{2.63}$$

Here, as usual in the literature[6], we introduce the "travelling" coordinate system $z = x - c_0 t$ in which the reference frame z moves "with the wave" at speed c_0. Also, we define the new slow changing $\tau = t$ that corresponding to the travelling coordinates. The changes in the new coordinates can be related to the standard ones as

$$\frac{\partial}{\partial x} = \frac{\partial}{\partial z} \quad , \quad \frac{\partial}{\partial t} = \frac{\partial}{\partial \tau} - c_0 \frac{\partial}{\partial z} \tag{2.64}$$

[6] Although for boundary problems is more convenient to transform the reference frame to a "retarded time" coordinate, we introduce the spatial "travelling" coordinates for convenience. The transformation here would be more appropriate for initial value problems.

After some algebra, substitution of Eqs. (2.64) in Eq. (2.63) yields the lossless version of the Burgers equation

$$\frac{\partial p}{\partial \tau} + \frac{\beta}{\rho_0 c_0} p \frac{\partial p}{\partial z} = 0, \tag{2.65}$$

where the term $\partial^2 p/\partial \tau^2$ has been neglected due to the slowness change in the time τ. This equation can be rewritten in terms of particle velocity using the first order relation $v \approx p/\rho_0 c_0$ as

$$\frac{\partial v}{\partial \tau} + \beta v \frac{\partial v}{\partial z} = 0. \tag{2.66}$$

That is actually more close to its original form derived by Burgers. For convenience, let us return again to the static reference coordinate system, where Eq. (2.66), can be expressed as

$$\frac{\partial v}{\partial t} - (c_0 + \beta v) \frac{\partial v}{\partial x} = 0. \tag{2.67}$$

In this evolution equation is clearly evident amplitude dependence of the wave speed $c = c_0 + \beta v$, causing the well known steepening of the waveforms. As in previous sections, we know that the layered dispersion arises from the solution of the linearized wave equation with the layered media boundary conditions, where the eigenvalue problem leads to the Rytov's dispersion relation Eq. (2.1). In order to model KdV type dispersion, $\omega = c_0 k - b k^3$, an additional term can be introduced into the Eq. (2.67):

$$\frac{\partial v}{\partial t} - (c_0 + \beta v) \frac{\partial v}{\partial x} + b \frac{\partial^3 v}{\partial x^3} = 0\,. \tag{2.68}$$

With this term, the leading equation (in traveling coordinates) is the KdV equation, the most widely model for nonlinear waves in dispersive media. One of the exacts solution of the KdV equation is the solitary wave

$$v\,(x,t) = A \mathrm{sech}^2\left(\gamma\,(x - Vt)\right), \tag{2.69}$$

where the soliton width, γ, the amplitude, A, ant its speed, V, are related as

$$\gamma = \sqrt{\frac{\beta A}{12 b}}\,, \tag{2.70}$$

$$V = c_0 + \frac{\beta A}{3} \tag{2.71}$$

Here and beyond, we will demonstrate numerically the existence of this solution in the layered media, showing its limits of validity. Furthermore, we will investigate the behavior of solitary waves in the regime in which the layered media dispersion cannot be described by a KdV model with accuracy.

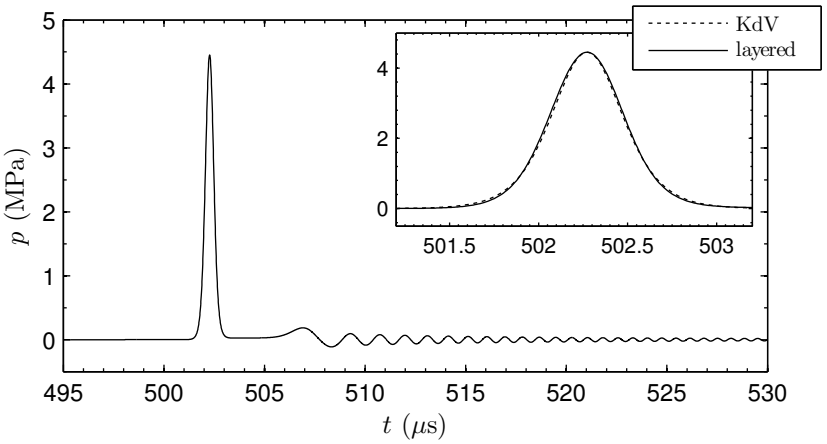


Figure 2.36: Solitary wave for the layered parameters $c_2/c_1 = 0.1$ and $\alpha = 0.1$, (continuous line) numerical solution of the layered media (dotted line) KdV solution.

Figure 2.36 shows the evolution of solitary waves for the layered parameters $c_2/c_1 = 0.1$ and $\alpha = 0.1$. As shown previously in Fig. 2.35, in this regime of parameters the layered dispersion can be described precisely by the KdV dispersive model. Due to both models are not exactly the same (even for the mono-atomic chain this is not fulfilled), we cannot claim the solitary wave solution observed in the layered system is strictly described by the solitary solution Eq. (2.69). However, as can be seen from the numerical tests, both solution closely agrees.

2.6.2 Non-cubic dispersion solitons

The presented KdV-like soliton exist only for a particular set of condition. In general, the dispersion near the band gap cannot be accurately described by the KdV dispersion. Furthermore, in case of high-amplitude/low-width solitary waves, the soliton spectrum can reach superior bands, that are in-existent in the KdV model. Here, we briefly present the existence of solitons with its width comparable to the lattice separation. Figure 2.37 shows four examples of propagating localized waves with different amplitudes. As can observed, as the soliton amplitude increases its speed increases and its width reduces, as commonly observed is any solitary wave. However, it can be seen that for high amplitude solitons, in which the width of the localized wave is of the order of the lattice, there exist remarkable differences with the continuum KdV approximation. In this simulations, the initial excitation is the KdV solution. Thus, for the low amplitude regime (Fig. 2.37 (a)) the soliton solution matches the excitation and propagates without changing its shape, amplitude and velocity. However, for higher amplitudes (Fig. 2.37 (b, c)) , it can be observed that the KdV is not the exact solution: the solitary wave breaks into

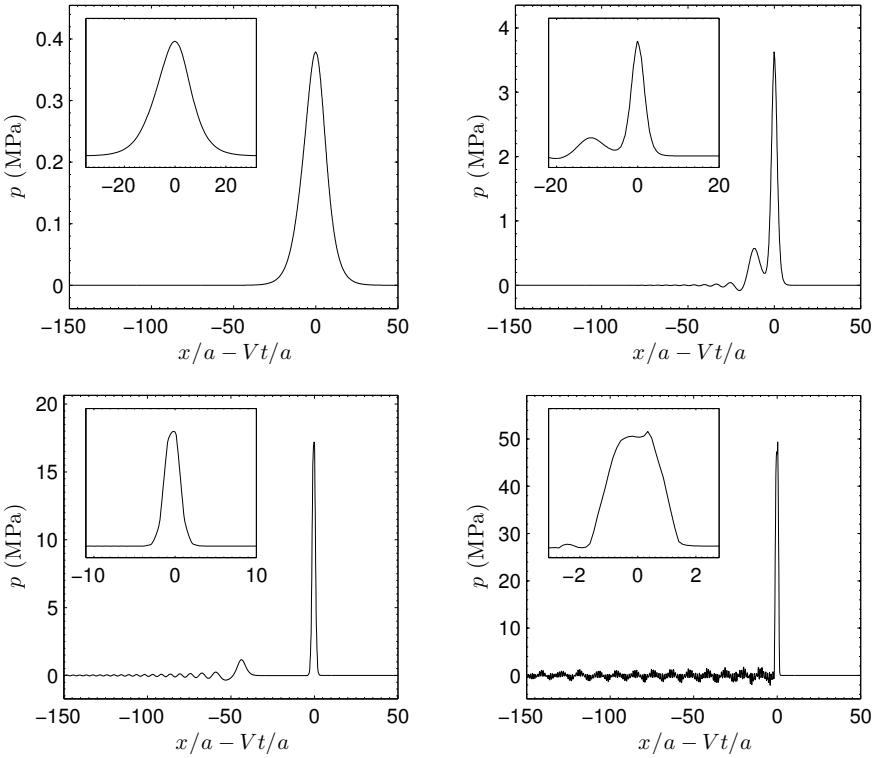


Figure 2.37: Examples of 4 solitons with increasing amplitudes.

other wave-packets plus an oscillatory tail that its left behind. Finally, in the regime width the soliton spectrum extend over the band-gap and up to second band, i.e. for very localized waves waves (Fig. 2.37 (d)) , the solitary wave suffers from a process of radiation. Note this radiation is totally different from the oscillatory tail shown in Figs. 2.37 (b, c): this radiation is not left behind and the localized wave continuously radiate low linear waves or phonons on its tail.

On the other hand, Fig. 2.38 shows the space time diagram of these waves. It can be seen clearly how the speed increases from c_0 to V, being V the speed of the localized wave. Here, the radiation is not visible due to the scaling of the color map but another particular feature of this system can be observed. For high amplitude solitons, the amplitude oscillates periodically in time and space, showing variations that in space matches the lattice period a and in time Vt/a. Therefore, the main features of the solitons in the discrete limit, where the width of the wave is comparable to the layer thickness is the existence of tail radiation and periodic oscillatory amplitude of the strongly localized waves.

A more detailed study is presented in Fig. 2.39, where we show the amplitude

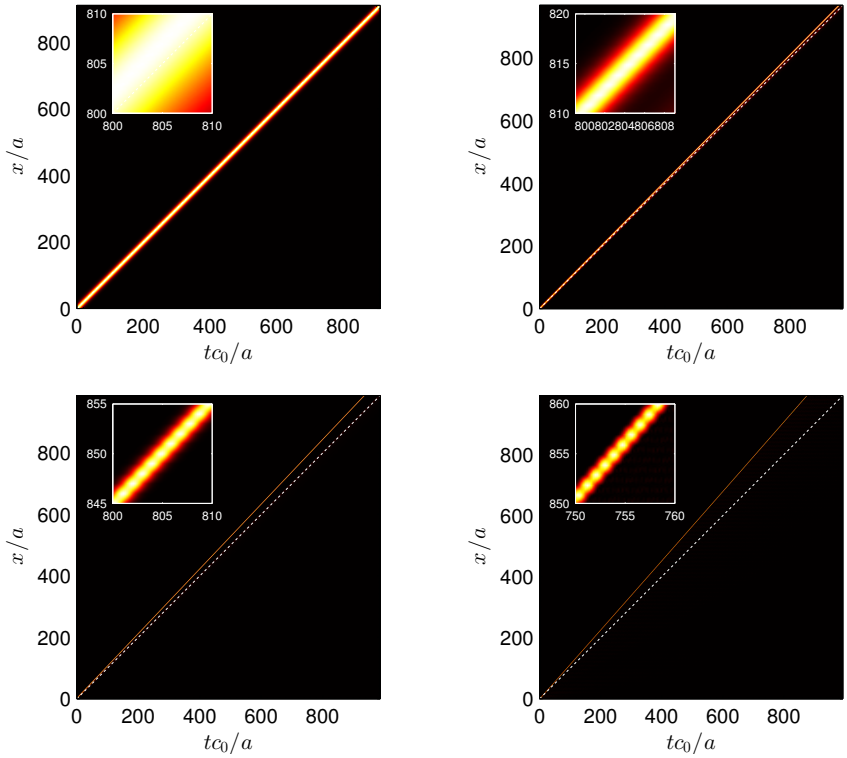


Figure 2.38: Space-time diagram representation of the solitons in Fig. 2.37, with increasing amplitude and velocity.

dependence of the soliton amplitude in function of its velocity. It can be seen that the KdV regime is only valid for weakly nonlinear excitations, of in other words, for wide solitons. For amplitudes of several MPa[7] the soliton velocity observed in simulations is considerably higher than in the KdV model.

2.6.3 1D Layered chirped: progressive amplification of solitons

The layered media offers the possibility of artificially modify the dispersion relation. As seen in previous sections, the modification of the lattice parameters can be made adiabatically, increasing or decreasing the lattice period progressively with distance forming chirped layered structure. Along the solitary wave amplitude, speed an thickness depends on the dispersion, the chirped la provides an usefully way to progressively amplify solitons. Thus, we present a test of this idea where

[7]The lattice parameters were $a = 0.85$, $c_2 = 1500$ m/s, $c_1 = 450$ m/s and $d = 0.225$ mm

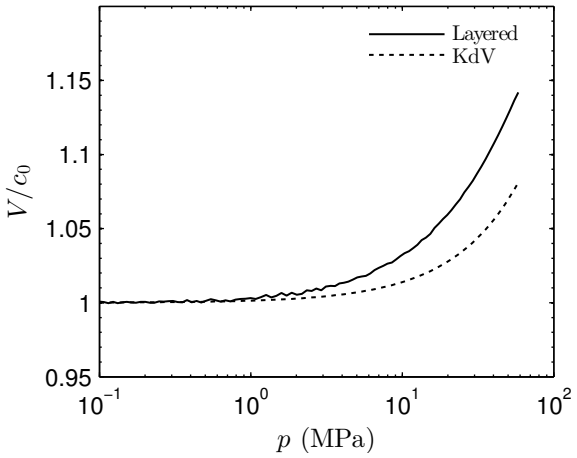


Figure 2.39: Soliton speed as a function of its amplitude for (continuous line) numerical results and (dotted line) KdV solution.

a chirped lattice period decreases with distance.

The initial excitation at the beginning of the lattice is a wide, KdV-type excitation. Thus, as Fig. 2.40 shows, soliton start to propagate at a supersonic, but low speed. As long the period is decreased, the dispersion seen by the wave adiabatically changes. Thus, the solitary wave solution slowly adapts it amplitude and thick according to the local dispersion. The result is that the wave can be stretched, amplified and accelerated to higher supersonic speeds. This proof of concept provides a method to manage the parameters of localized waves that can be applied to any other lattice. Configurations of special interest are probably the dispersion management of strain solitons in micro-structured composites, high intensity ultrasonic cutting devices for medical applications triggered by trains of amplified and pulsed excitations (instead of continuous mode) to reduce the heating and material fatigue (Harvey et al., 2014), or even period-varying granular beads composed of metallic spheres for drilling devices that can be usefully planetary exploration (Harkness et al., 2012).

2.7 Conclusions

In this Chapter we have analyzed the nonlinear propagation of acoustic waves in a layered media. The harmonic generation processes are presented and discussed mainly with numerical solutions considering a fluid-fluid structure. The strong characteristic dispersion of a layered media, in addition to the fluid nonlinearity, provides a wide range of possibilities for harmonic generation and control. In this

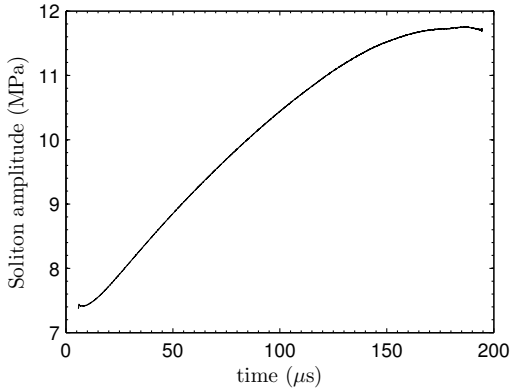


Figure 2.40: Progressive amplification of a soliton traveling in a chirped lattice.

sense, the effective nonlinearity of the composite media can be tuned for obtaining the desired harmonic balance. We provide the methods for selective harmonic generation, where the material layers can be adjusted for generate only second harmonic, only third harmonic, discard the even harmonics creating a cubic-nonlinear medium composed of quadratically-nonlinear layer. We provided also conditions for fabrication of waveguides for intense acoustic waves with extraordinary nonlinear distortion. Finally, the layered media provides conditions for dispersion management solitons, that are briefly presented, extending the work existent in the literature to the discrete limit of the soliton in which the width is of the order of the media periodicity.

On the other hand, much work on modeling the presented results remains. In this sense, we are currently working on Coupled Mode Theory. This analytical method widely used in optics (Malomed, 2000) can provide simple explanation of the dynamics of the system in terms of forward and backward coupled fields for fundamental and higher harmonics.

References

Albin, Nathan and Oscar P. Bruno (2011). "A spectral FC solver for the compressible Navier Stokes equations in general domains I: Explicit time-stepping". In: *J. Comput. Phys.* 230.16, pp. 6248–6270.

Botteldooren, D. (1996). "Numerical model for moderately nonlinear sound propagation in three-dimensional structures". In: *J. Acoust. Soc. Am.* 100.3, pp. 1357–1367.

Boussinesq, Joseph (1877). *Essai sur la théorie des eaux courantes*. Vol. 2. Imprimerie nationale.

Boussinesq, Joseph Valentin (1871). "Théorie générale des mouvements qui sont propagés dans un canal rectangulaire horizontal". In: *CR Acad. Sci. Paris* 73, pp. 256–260.

Brillouin, L. (2003). *Wave Propagation in Periodic Structures: Electric Filters and Crystal Lattices*. Dover phoenix editions. Dover Publications.

Cheng, YC, S Kicas, J Trull, M Peckus, C Cojocaru, R Vilaseca, R Drazdys, and K Staliunas (2014). "Flat Focusing Mirror". In: *Scientific reports* 4, pp. –.

Fainstein, Alejandro, N Daniel Lanzillotti-Kimura, Bernard Jusserand, and B Perrin (2013). "Strong optical-mechanical coupling in a vertical GaAs/AlAs microcavity for subterahertz phonons and near-infrared light". In: *Physical review letters* 110.3, p. 037403.

Ginter, Siegfried, Marko Liebler, Eckard Steiger, Thomas Dreyer, and Rainer E. Riedlinger (2002). "Full-wave modeling of therapeutic ultrasound: nonlinear ultrasound propagation in ideal fluids." In: *J. Acoust. Soc. Am.* 111.5, pp. 2049–2059.

Gurbatov, S.N., O.V. Rudenko, and A.I. Saichev (2011). "Waves and Structures in Nonlinear Nondispersive Media. General Theory and Applications to Nonlinear Acoustics". In: ed. by S.N. Gurbatov, O.V. Rudenko, and A.I. Saichev. Springer. Chap. Chapter 8. Types of Acoustic Nonlinearities and Methods of Nonlinear Acoustic Diagnostics, pp. 271–304.

Hamilton, Mark F, David T Blackstock, et al. (1998a). *Nonlinear acoustics*. Vol. 237. Academic press San Diego.

Harkness, Patrick and Margaret Lucas (2012). "A brief overview of space applications for ultrasonics". In: *Ultrasonics* 52.8, pp. 975–979.

Harvey, Gerald, Anthony Gachagan, and Tapiwa Mutasa (2014). "Review of high-power ultrasound-industrial applications and measurement methods". In: *Ultrasonics, Ferroelectrics and Frequency Control, IEEE Transactions on* 61.3, pp. 481–495.

Huynh, A, ND Lanzillotti-Kimura, B Jusserand, B Perrin, A Fainstein, MF Pascual-Winter, E Peronne, and A Lemaître (2006). "Subterahertz phonon dynamics in acoustic nanocavities". In: *Physical review letters* 97.11, p. 115502.

Huynh, Agnes, B Perrin, and A Lemaître (2015). "Semiconductor superlattices: A tool for terahertz acoustics". In: *Ultrasonics* 56, pp. 66–79.

Jacob, Xavier, Stefan Catheline, Jean-Luc Gennisson, Christophe Barrière, Daniel Royer, and Mathias Fink (2007). "Nonlinear shear wave interaction in soft solids". In: *The Journal of the Acoustical Society of America* 122.4, pp. 1917–1926.

Kordeweg, DJ and G de Vries (1895). "On the change of form of long waves advancing in a rectangular channel, and a new type of long stationary wave". In: *Phil. Mag* 39, pp. 422–443.

Kosevich, Arnold M. (2005). "The Crystal Lattice: Phonons, Solitons, Dislocations, Superlattices, Second Edition". In: *The Crystal Lattice*. Ed. by Arnold M. Kosevich. Wiley-VCH Verlag GmbH & Co. KGaA. Chap. Chapter 5. Acoustics of Elastic Superlattices: Phonon Crystals, pp. 153–162.

Liang, Bin, Bo Yuan, and Jian-chun Cheng (2009). "Acoustic diode: Rectification of acoustic energy flux in one-dimensional systems". In: *Physical review letters* 103.10, p. 104301.

Malomed, Boris A (2000). "Solitons in optical media with quadratic nonlinearity". In: *Nonlinear Science at the Dawn of the 21st Century*. Springer, pp. 247–262.

Maryam, W, AV Akimov, RP Campion, and AJ Kent (2013). "Dynamics of a vertical cavity quantum cascade phonon laser structure". In: *Nature communications* 4.

Naugolnykh, K. and L. Ostrovsky (1998). *Nonlinear Wave Processes in Acoustics*. Cambridge Texts in Applied Mathematics. Cambridge University Press.

Rayleigh, Lord (1876). "On waves". In: *Phil. Mag* 1.5, pp. 257–279.

Romero-García, Vicente, R Picó, A Cebrecos, Víctor José Sánchez-Morcillo, and K Staliunas (2013). "Enhancement of sound in chirped sonic crystals". In: *Applied Physics Letters* 102.9, p. 091906.

Rudenko, O.V. and S.I. Soluian (1977). *Theoretical foundations of nonlinear acoustics*. Studies in Soviet science. New York, NY 10011, USA: Consultants Bureau, p. 274.

Russell, J Scott (1844). "Report on waves". In: *14th meeting of the British Association for the Advancement of Science*. Vol. 311, p. 390.

Sánchez-Morcillo, V., I. Pérez-Arjona, V. Romero-García, V. Tournat, and V. Gusev (2013). "Second-harmonic generation for dispersive elastic waves in a discrete granular chain". In: *Physical Review E* 88.4, p. 043203.

Santosa, Fadil and William W Symes (1991). "A dispersive effective medium for wave propagation in periodic composites". In: *SIAM Journal on Applied Mathematics* 51.4, pp. 984–1005.

Tournat, V, VE Gusev, V Yu Zaitsev, and B Castagnede (2004). "Acoustic second-harmonic generation with shear to longitudinal mode conversion in granular media". In: *Europhysics Letters* 66.6, p. 798.

Vanhille, Christian and CleofCampos-Pozuelo (2004). "Numerical simulation of two-dimensional nonlinear standing acoustic waves". In: *J. Acoust. Soc. Am.* 116.1, p. 194.

Yong, Darryl H and Randall J LeVeque (2003). "Solitary waves in layered nonlinear media". In: *SIAM Journal on Applied Mathematics* 63.5, pp. 1539–1560.

Yun, Y, GQ Miao, P Zhang, K Huang, and RJ Wei (2005). "Nonlinear acoustic wave propagating in one-dimensional layered system". In: *Physics Letters A* 343.5, pp. 351–358.

Zabusky, Norman J and Martin D Kruskal (1965). "Interaction of solitons in a collisionless plasma and the recurrence of initial states". In: *Phys. Rev. Lett* 15.6, pp. 240–243.

Publications

The contents of this chapter has been presented in the following publications:

Journal papers

- **Jiménez, N.**, Mehrem, A., Picó, R., García-Raffi, L. M., Sánchez-Morcillo, V. J. "Nonlinear propagation and control of acoustic waves in phononic superlattices" *Comtes Rendus Physique : Special issue on phononic crystals*, Elsevier. *Submitted* 19 May (2015).

Conference proceedings

- V.J. Sánchez-Morcillo, **N. Jiménez**, A. Mehrem, R. Picó, Ll. García-Raffi, V. Romero-García, V. Tournat. "Nonlinear waves in periodic media: from lattices to superlattices and phononic crystals". *PHONONICS 2015: 3nd International Conference on Phononic Crystals/Metamaterials, Phonon Transport and Phonon Coupling.* Paris, France. May 31–June 5 (2015)
- V. J. Sánchez-Morcillo, **N. Jimenez**, A. Mehrem, E.M. HamHam, L. García-Raffi and R. Picó. "Propagation of Intense Acoustic Waves in Sonic Crystals", *ICU 2015: International Congress on Ultrasonics.* Metz, France. May 11-14 (2015)
- Mehrem, A., Hamham, E. M., **Jiménez, N.**, Cebrecos, A., Pico, R.; Sanchez-Morcillo, V. and García-Raffi, L. M. "Nonlinear Acoustic Waves Periodic Media" *7th Forum Acusticum 2014.* Krakow, Poland. September 7 (2014)